INTERNATIONAL JOURNAL OF AVIATION SCIENCE AND TECHNOLOGY
IJAST
www.ijast.org

International Journal of Aviation Science and Technology

Volume 3, Issue 1, June 2022

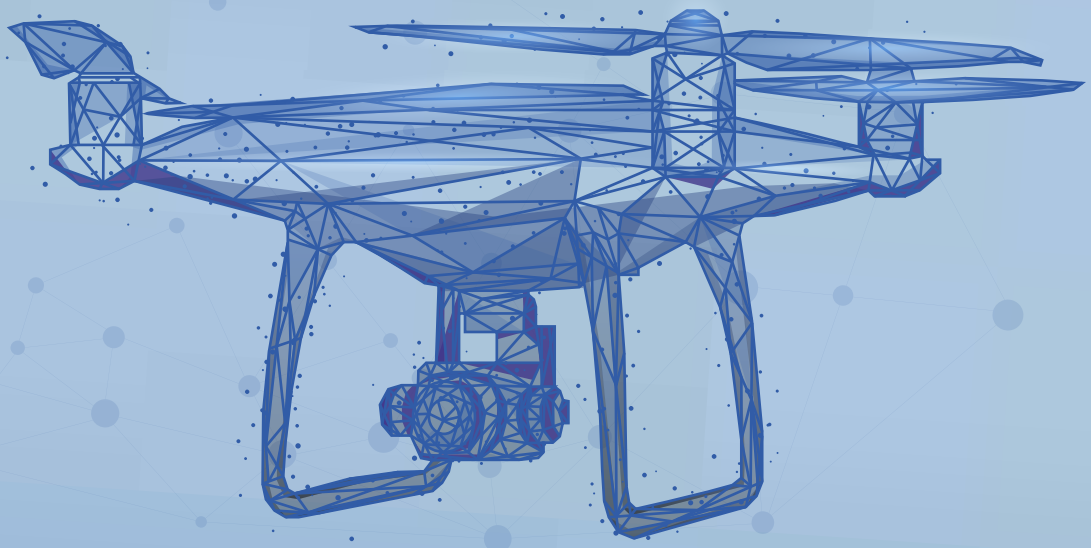

e-ISSN: 2687-525X
INTERNATIONAL SUSTAINABLE AVIATION AND ENERGY RESEARCH SOCIETY
SARES
www.sares.org

International Journal of Aviation Science and Technology

Publisher : SARES
International Sustainable Aviation and Energy Research Society
Licence holder : Prof. Dr. T. Hikmet Karakoç (President, SARES)
Address : Anadolu University TGBD TechnoPark Region No:210
26470 Eskisehir, Turkiye

e-ISSN : 2687-525X
DOI : 10.23890/IJAST
Submission : www.ijast.org
e-mail : ijast@sares.org
Copyright : SARES Society

IJAST is published with the contribution of "Research and Application Center of Civil Aviation, Eskisehir Technical University"

Index

International Journal of Aviation Science and Technology

Research Article

Effect of Coordination on Transient Response of a Hybrid Electric Propulsion System

Teresa Donateo[1], Ludovica Spada Chiodo[2]*, Antonio Ficarella[3]

[1] *University of Salento, Department of Engineering for Innovation, Lecce, Italy*
teresa.donateo@unisalento.it - 0000-0001-5189-679X

[2] *University of Salento, Department of Engineering for Innovation, Lecce, Italy*
ludovica.spadachiodo@unisalento.it - 0000-0002-0320-6958

[3] *University of Salento, Department of Engineering for Innovation, Lecce, Italy*
antonio.ficarella@unisalento.it - 0000-0003-3206-4212

Abstract

Thanks to its typical limited speeds and altitudes, Urban Air Mobility represents an interesting application for electric and hybrid-electric power systems. In addition, short-range requirements are compatible with the limited performance of today's batteries, conversely to their current inapplicability for commercial aviation purposes. For the present study, a parallel Hybrid Electric Propulsion System for a coaxial-rotor Air Taxi has been implemented in Simulink and tested on four different sets of operating conditions, with a transient signal as input for the Power Lever Angle command. The goal of this investigation is to analyze the transient behavior of the hybrid-electric propulsion system in question, to underline the role of electric motors in assisting thermal engine during transients, and, in particular, focuses on the benefits deriving from the adoption of a coordination block which adapts torque split between the two power sources on the basis of actual engine response.

Keywords

Urban Air Mobility
Hybrid electric vehicles
Transient response

Time Scale of Article

Received 11 January 2022
Revised until 4 March 2022
Accepted 30 April 2022
Online date 28 June 2022

1. Introduction

During the last decade, many aerospace companies have developed solutions for Urban Air-Mobility (UAM). UAM refers to safe, efficient, and clean urban transportation systems by air, which, according to the EASA (European Aviation Safety Agency), is expected to spread in Europe within 3-5 years (EASA, 2022) and to overcome the ever-increasing ground traffic congestion (Airbus, 2022; FEV, 2022).

Generally designed in the form of VTOL, UAM vehicles can be propelled by several propulsive systems, ranging from hybrid to electric: in fact, their typical short-range requirements, limited speed (in comparison with longer distance commuters) and altitudes up to 1000ft (Uber Elevate, 2016), make UAM compatible with such propulsive systems even though to date batteries state of the art isn't satisfactory in terms of power and energy density to be employed in larger applications (Airbus, Micro-hybridisation: the next frontier to electrify flight?, 2021).

In HEPS for Urban Air Mobility vehicles, the presence of a dual-energy storage system results in an increment in endurance and range. It offers an additional advantage, the availability of electric backup in engine failure, allowing for a few minutes of extra endurance after failure occurrence.

Moreover, the electric power source represents a useful assist for the thermal engine during high power request flight phases: in parallel architecture, the engine could be operated at its nominal power, and additional power could be supplied from electric motors during take-off

*: Corresponding Author Ludovica Spada Chiodo , ludovica.spadachiodo@unisalento.it
DOI: 10.23890/IJAST.vm03is01.0101

or climb, while excess engine power could be spent in charging the batteries during the cruise (Rendón, Sánchez R., Gallo M., & Anzai, 2021).

However, hybrid UAM vehicles introduce necessarily disadvantages in terms of increased weight and higher complexity of the power and control systems.

The hybrid propulsive system employed in the present study will be described in the following, and the energy management strategy will be briefly summarized.

The goal of this investigation is to underline the role of the electric machines in improving the dynamic response of the system during transient operating conditions, namely when a power request variation is encountered. Besides a conventional parallel HEPS, a modified version is tested, where a coordination block is provided to boost system response during engine delays.

To the authors' knowledge, no similar study is presented in literature either numerically or experimentally, except for (Roumeliotis, et al., 2019), where a much more simplified approach is considered for the transient behavior of the system, and (Wortmann, Schmitz, & Hornung, 2014) where investigation of the transient behavior of a turbofan engine with different percentages of electric assist with a different control logic is carried out.

1.1. The Air-Taxi

In this investigation, a rotorcraft for UAM, namely a coaxial-rotor Air Taxi, with a parallel HEPS is considered (Guzzella & Sciarretta, 2007): the thermal engine and the Li-ion battery-fed electric motors are mechanically connected to the rotor shaft through a gear-box (Fig 1).

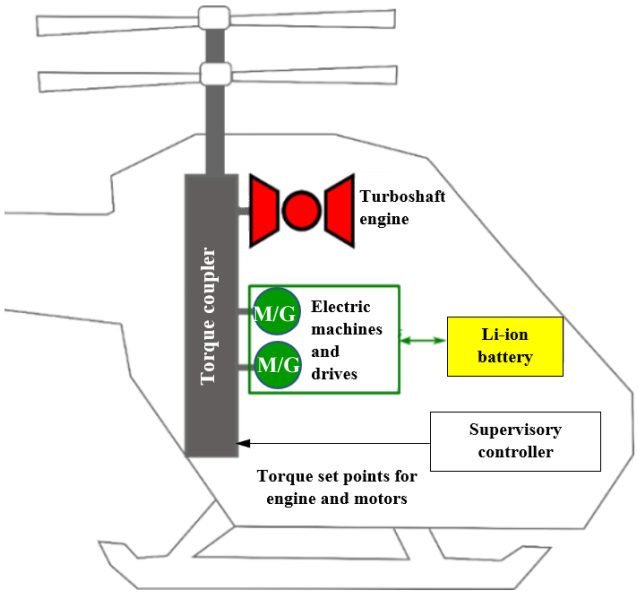

Fig. 1. Parallel HEPS for coaxial-rotor Air Taxi

Since the power management of the multi-source operation is a critical feature in HEPS, this aspect has been previously investigated by some of the authors (Donateo, Terragno, & Ficarella, 2021). In particular, the optimal curve for the discharge of the battery along the mission, denoted here as Reference State of Charge (RSOC), was found with the application of the Dynamic Programming Method.

The energy management strategy used for this investigation is based upon the application of a fuzzy logic system where the input variables are the required power at the rotor shaft and the deviation of the actual battery state of charge from the RSOC, while the output is the splitting of required power between the thermal engine and the electric machines. The constraint of keeping the battery in sufficient charge during the whole mission (to make electric backup available at any time in case of engine failure, even in the case of an aged battery) is implemented in the strategy, as explained later.

2. Methods

The behavior of the proposed power system, whose detailed description will be given in the following subsections, has been tested when a transient PLA command is given in input to the model, representing an arbitrary discontinuity in power request.

In particular, four different sets of operating conditions have been simulated, each characterized by a steady-state value of reference PLA, altitude, airspeed, and hybridization degree k. Such values are reported in Table 1. The choice of these operating conditions was made by considering two different missions, as shown in Fig. 2 (Donateo, De Pascalis, Strafella, & Ficarella, 2021). The value of k and the state of charge of the battery in the four operating points were set according to the results of a previous investigation (Donateo, Terragno, & Ficarella, 2021).

Then, a transient signal of the form depicted in Fig. 3 was applied to modify the reference PLA command to model an increase from 80% to full value in a time interval of 0.1 s. Such discontinuity was chosen arbitrarily to investigate the system response to a quasi-step input, which would represent the most demanding situation for the engine.

In addition, a sample case has been simulated to compare the performance of the hybrid system with a 0.5 hybridization degree to that of the same thermal engine

as standalone power source (k = 0).

The implemented Simulink model can be summarized by the flow chart in Fig. 4.

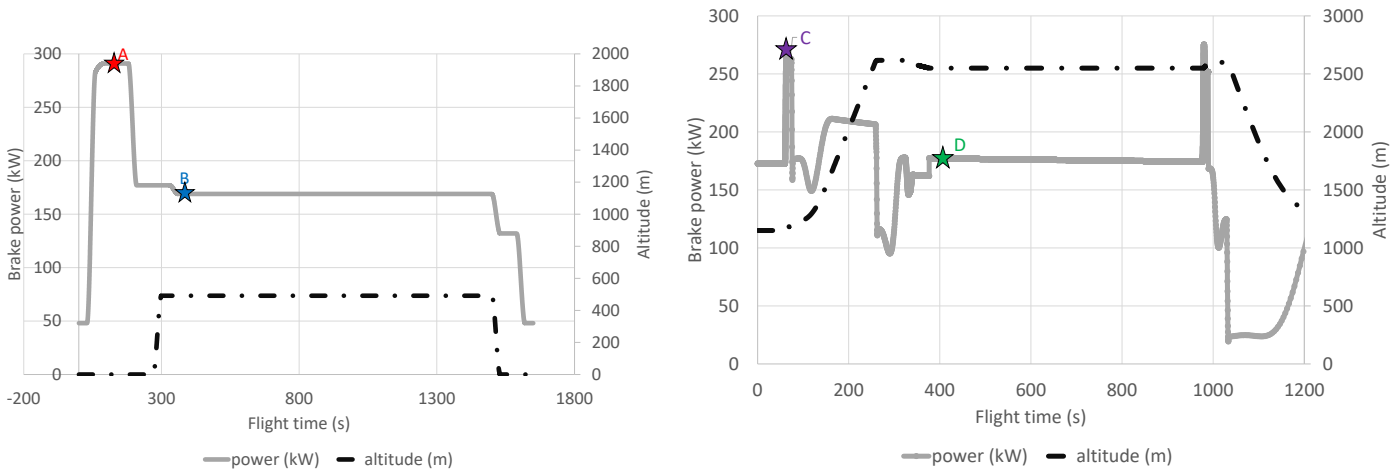

Fig. 2. Choice of the operating points.

Table 1 Operating conditions for the simulations

	Op. point A	Op. point B	Op. point C	Op. point D
PLAref (%)	65.3	50.3	68	61.5
Altitude (m)	0	492	1154	2550
True Air Speed (m/s)	30.6	30.6	4	0
Electric contribution *k*	0.4	0.7	0.47	0.6
Battery state of charge	99%	85%	99%	78%

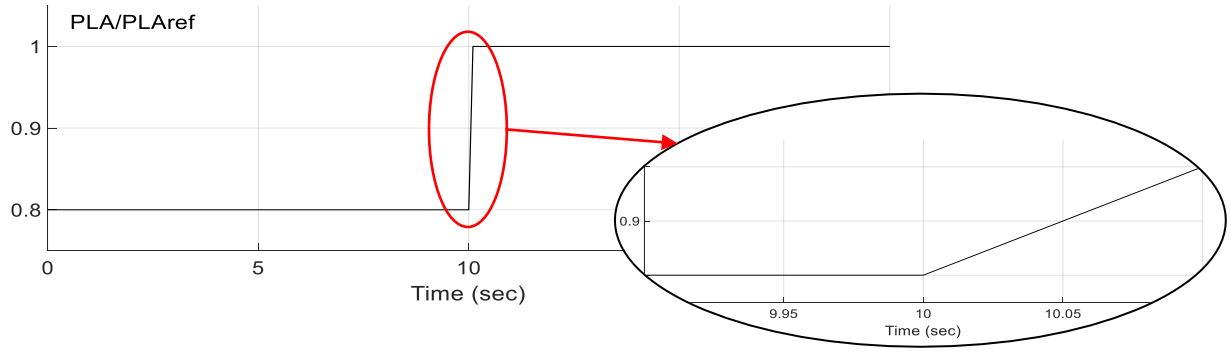

Fig. 3. Input PLA transient signal modifier.

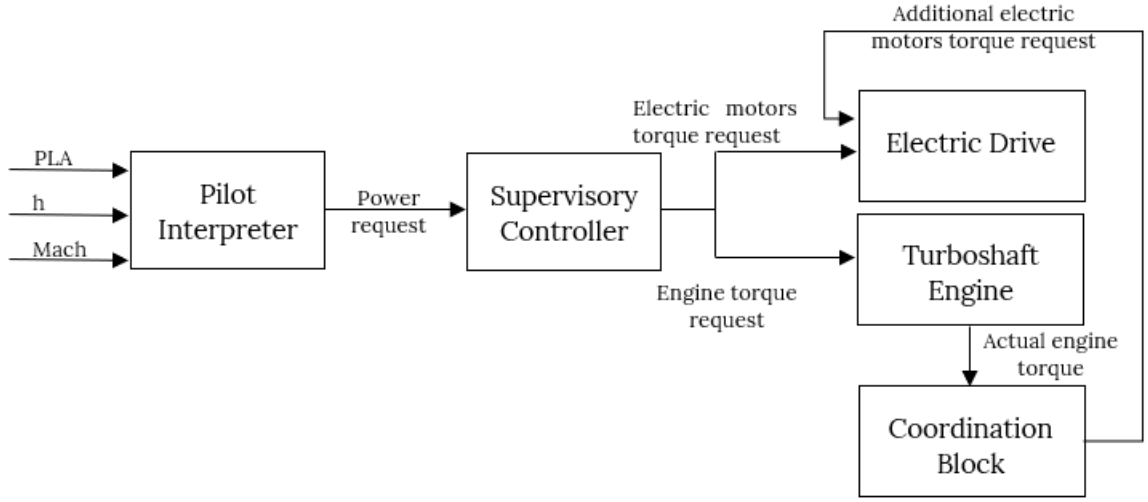

Fig. 4. HEPS model flow chart.

2.1. The Turboshaft Engine

The engine is a twin-spool turboshaft engine where the high-pressure spool connects the High-Pressure Turbine (HPT) to the compressor and rotates at the speed N_c. The Low-Pressure Turbine (LPT) is connected to the load shaft via the low-pressure spool, whose speed is assumed to equal the nominal value (N_p).

The inlet is modeled to convert the dynamic pressure of the incoming flow into static pressure with a constant efficiency of 0.9. Compressibility effects are not considered because of the typical low speeds.

Operating points are obtained from component maps available to the authors and provided in the form of lookup tables inside rotating components blocks.

A PID controller is provided to regulate fuel flow rate based on actual net LP shaft power output (since a small amount of power extraction from LP spool is considered for auxiliaries, too) and shaft power request. The controller acts to drive the power error to zero, and the automatic tuning encompassed in Matlab has been used to set its parameters, but its setting goes beyond the scope of this work. The authors intend to perform a more accurate setting of the PID controller parameters as further development of the present investigation.

The volume dynamics is taken into account by applying the inter-component volume (ICV) method as proposed in (Wang, Li, & Yang, 2017): the transient effects on fluid pressure p in the ICV volumes A and B preceding and following the HPT module (Fig. 5) are described by the following equation:

$$\frac{dp}{dt} = \frac{RT}{V}\frac{dm}{dt} = \frac{RT}{V}(\dot{m}_{in}-\dot{m}_{out}) \quad (1)$$

where the variation of mass is due to the unbalance between the volume incoming ($\dot{m}_{in}$) and outgoing ($\dot{m}_{out}$) the flow rates in transient conditions while it is zero in stationary conditions.

As for shaft dynamics, the balance of the work between the components on the same shaft is implemented to calculate the mechanical dynamic response, accordingly to Eq. (2):

$$\dot{N_c} = \left[\frac{30}{\pi}\right]^2 \frac{1}{IN_c}[P_{HPT}-P_C] \quad (2)$$

which calculates angular acceleration as a function of net power on the HP shaft, current rotational speed, and spool inertia I.

At this stage of our investigation, only HP spool dynamics has been modeled since the rotor shaft speed N_p is assumed constant at 6000rpm. However, if an LP shaft balance has to be carried out, the shaft acceleration $\dot{N}_p$ will depend on the difference between power supplied from both electric motors and engine and the load applied to the shaft.

The entire thermal engine model and its performance as a standalone power source have been previously validated through comparison with an analogous model built in the commercial tool Gas Turbine Simulation Program (GSP). This allowed to obtain a reference mapping of engine power output as a function of PLA, Mach, and altitude (thus translating a PLA input into a power request) as well as to map the power turbine discharge pressure as a function of fuel flow rate.

GSP model has also provided reference values that have been used to set inter-component volumes and shaft inertias in the Simulink model.

2.2. The Electric Drive

The employed Li-ion battery is made of 73 cells in series and has a nominal capacity of 130 Ah. A Peukert coefficient n of 1.05 is assumed, in agreement with Dubarry's results (2009), to calculate battery effective current and thus update SOC according to Eq. 3 and Eq. 4.

The Open Circuit Voltage is tabulated as a function of the battery state of charge.

$$I_{eff} = I\cdot\left[\frac{I}{I_{nom}}\right]^{n-1} \quad (3)$$

$$SOC(t) = SOC(t_0) - 100\cdot\int_{t_0}^{t}\frac{I_{eff}(t)}{C}dt \quad (4)$$

The electric motors are modeled using Simulink *mapped motor* block through the maps of maximum continuous torque and efficiency lines. The inputs to the maps are the torque command, the required shaft speed, and the battery voltage. The block outputs are the actual torque output and battery current.

The maximum power output of the employed motors is 120 kW, and their dynamic behavior is modeled by assigning an intrinsic time constant of 0.02 s, which is given as the default value in Simulink mapped motor, to account for both the motor and drive response.

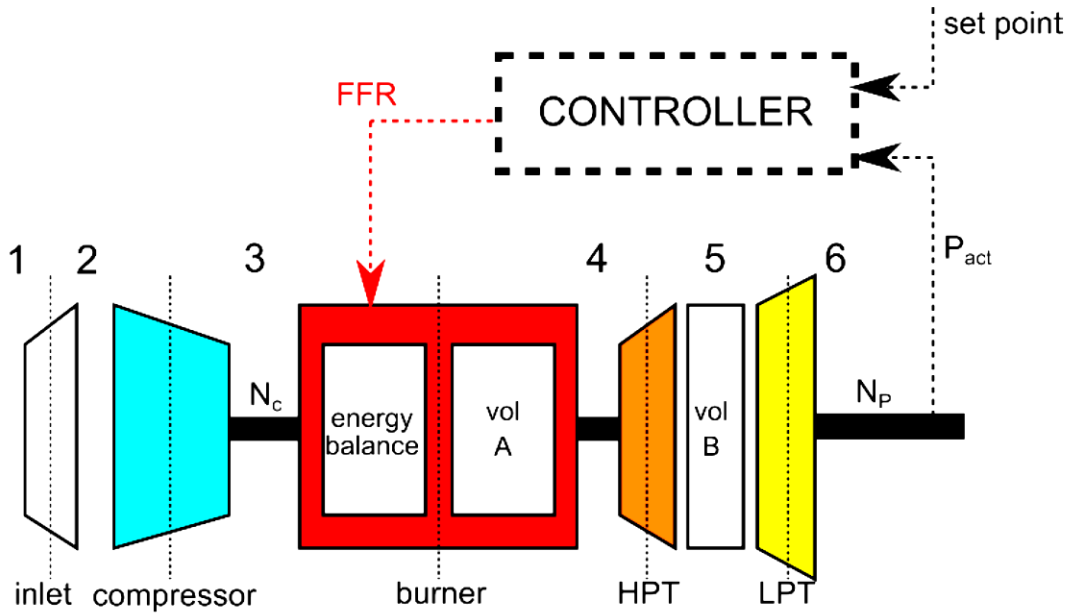

Fig. 5. Scheme of turboshaft engine with inter-component volumes.

2.3. Energy Management Strategy

The current model encompasses the capability to define an energy management strategy that is established at every time instant of the mission on the basis of current shaft power requests and battery parameters (SOC and SOH). In particular, a set of fuzzy rules is built into the supervisory controller to define the torque split between electric and thermal sources on the basis of instantaneous power demand, battery SOH and the deviation of actual SOC from the previously defined reference SOC (RSOC). Though for the present investigation, a user-defined hybridization degree is given at the beginning of its mission, and its value is held constant throughout the simulation. The selected values are those listed in Table 1.

In fact, other works from the same authors are aimed at developing and optimizing energy management strategies (Donateo, De Pascalis, Strafella, & Ficarella, 2021; Donateo, Terragno, & Ficarella, 2021) to meet the goals of fuel consumption minimization and electric backup preservation, here the focus is set on the dynamic performance improvement that can be achieved, for a fixed power split, through the activation of a coordination block: this can be defined as a device designed to account for instantaneous power difference between engine required power and engine actual power output and adjust management strategy as a consequence. Thus, when this difference is not zero, such quantity is fed as an additional load into the electric power source. In this manner, electric motors are supposed to balance power output and demand, mainly due to thermal engine response lag (suggested in (Roumeliotis, et al., 2019). That can be expressed as follows:

$$\text{If } T_{ICE} < T_{ICE,req} \quad (5)$$

$$\text{then } T_{EM} = T_{EM,req} + (T_{ICE,req} - T_{ICE}) \quad (6)$$

where T_{ICE} and T_{EM} represent actual engine and electric motors torque, and the subscript *req* refers to their respective required values.

Two cases are compared: in the first one, the energy management is simply obtained as output from the supervisory controller module (user-defined in this case), and the resulting torque split *k* is given in input to both the thermal engine and electric machine; in the second one, the coordination block is added, following the supervisory controller, to take advantage of the faster dynamics of the electric machines, so that *k* will be slightly altered from the predefined value if condition **(6)** is true.

3. Results

If a steep variation in power demand was encountered, the turboshaft engine would not be able to rapidly fulfill the new requirement because of its typical high inertia.

This is supposed to be quite evident, particularly in part-load applications, as suggested by (Wortmann, Schmitz, & Hornung, 2014).

To alleviate the impact of such behavior on global system performance, at every time instant, the difference between engine torque command and actual engine torque is loaded onto the electric module in the manner described in the previous section as a result of the coordination block activation, which is intended to leverage fast electric motor response in favor of a more respondent propulsive system as a whole.

For each of the four test cases, the parameters of Table 1 combined with the PLA modifier of Fig. 3 have been given in input to the HEPS Simulink dynamic model.

In the following pictures (Fig. 6), the power request and power output of the turboshaft engine, the electric motors, and the hybrid system is plotted for the system with both the coordination block on and off.

As it can be seen, after a fast power request increase from 80% to full value in 0.1 seconds, the overall system output achieves its target after 0.15 s on average when the coordination block is active, which means 0.05 s after the stabilization of the input signal, while it requires an additional time interval of about 0.15 s for the system without coordination to attain its nominal request, with a delay of 0.2 s for the response stabilization. So, the uncoordinated system response lags behind that of the coordinated system in all four cases, requiring four times the time needed from the latter to get the new steady condition.

More in general, the performance improvement made possible by hybridization of the system combined with the beneficial effect deriving from the activation of the coordination block can be evinced from Fig. : here, the higher slope of hybrid system response during transient is visible, in contrast with looser thermal engine response, which is characterized by a larger interval of instability, too.

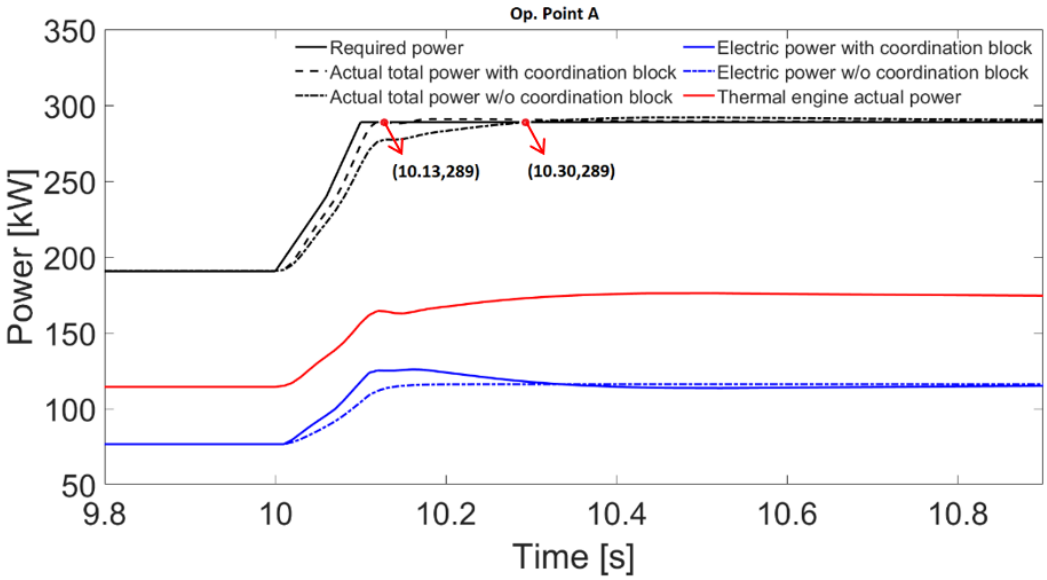

Fig. 6a. Effect of coordination on transient response, Op. Point A.

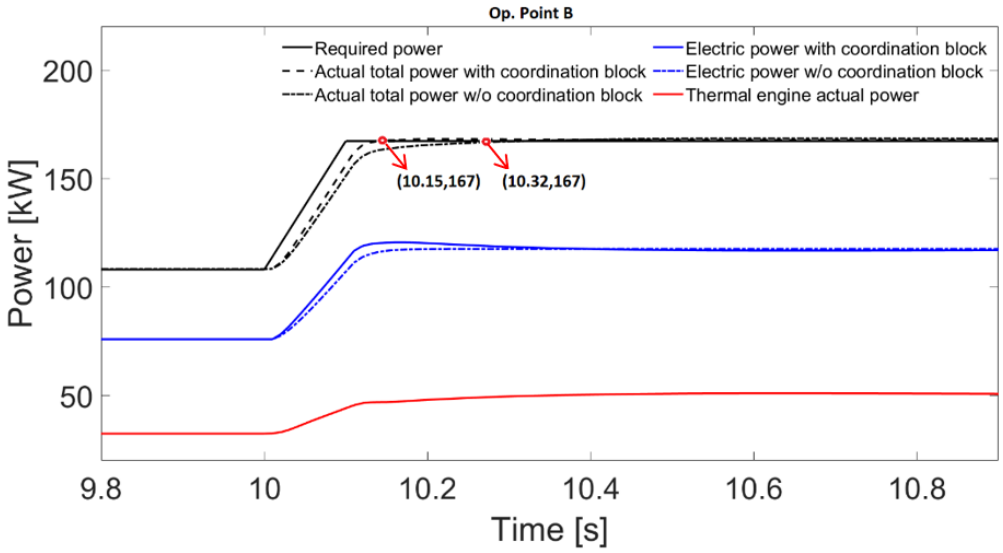

Fig. 6b. Effect of coordination on transient response, Op. Point B.

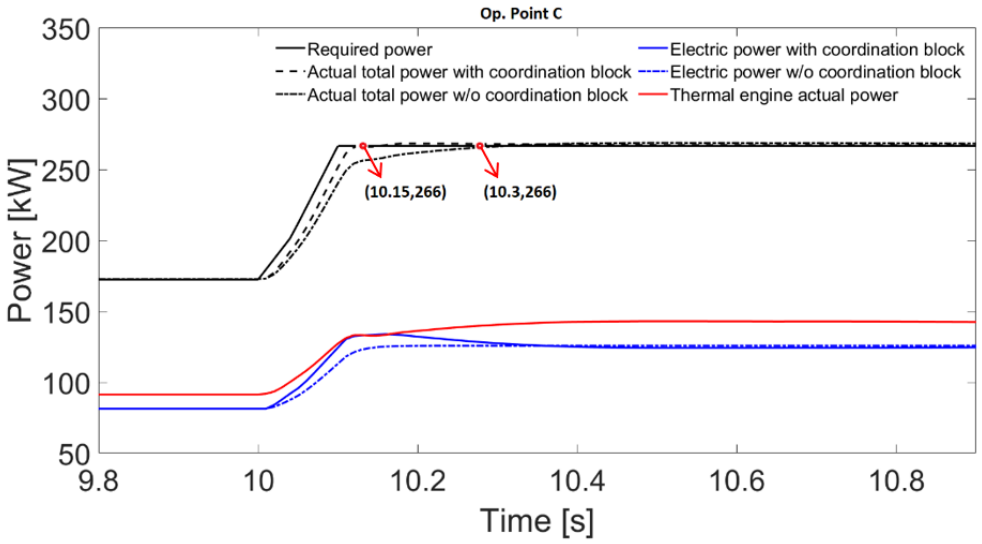

Fig. 6c. Effect of coordination on transient response, Op. Point C.

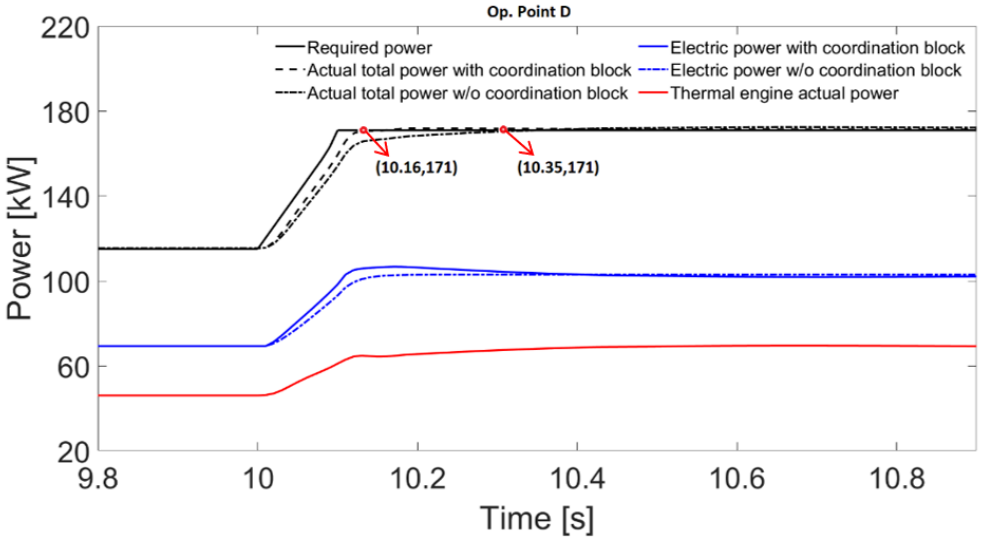

Fig. 6d. Effect of coordination on transient response, Op. Point D.

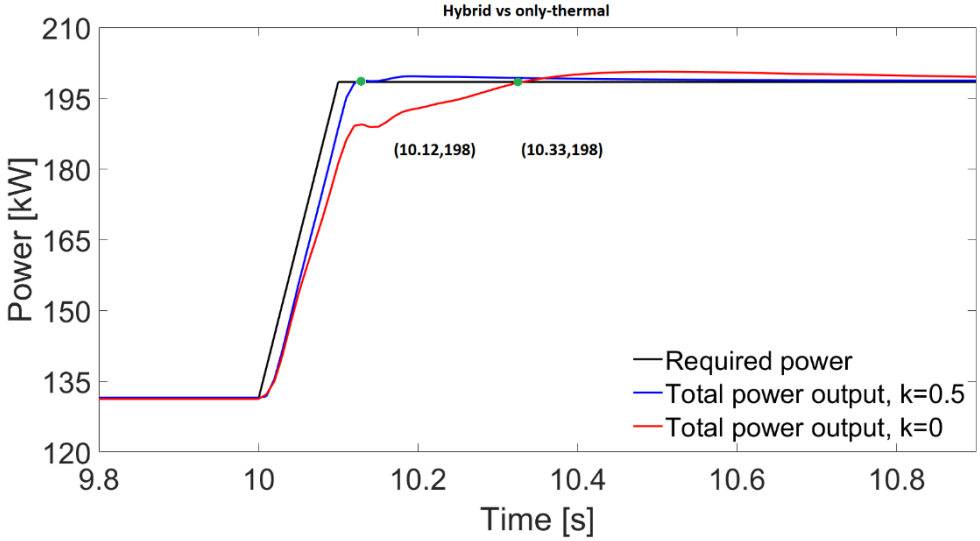

Fig. 7. Performance improvement attained with system hybridization.

4. Conclusions

This paper investigated the capability of a Hybrid Electric Propulsion System designed for Urban Air Mobility applications to rapidly match power demand variations in the form of a transient PLA command given in input to the tested Simulink model.

In particular, the paper focuses on the difference in transient response determined by the activation of a coordination block following the supervisory controller, which previously defined energy management strategy in terms of load split between thermal and electric modules. The role of the coordination block is that of adjusting electric power demand during transient phases to compensate for thermal engine response delay and thus allow the whole system to adapt faster to the new power request. This is made possible by the different typical inertias of the two power sources since it is known that electric machine's response times are generally lower than that of turbine engines, whose performance is even worse at part load use.

The coordination block has been revealed to be effective over all four typical mission profiles analyzed in the paper.

As a further development, a dynamic model of the rotor will be included to characterize LP spool dynamics more in-depth and thus investigate system behavior in a more realistic fashion.

Abbreviations

HEPS	:	Hybrid Electric Propulsion System
HPT	:	High Pressure Turbine
ICV	:	Inter Component Volume
LPT	:	Low Pressure Turbine
N_c	:	Core speed
N_p	:	Low pressure spool speed
PLA	:	Power Lever Angle
RSOC	:	Reference State of Charge
SOC	:	State of Charge
SOH	:	State of Health
UAM	:	Urban Air Mobility
VTOL	:	Vertical Take-Off and Landing

CRediT Author Statement

Ludovica Spada Chiodo: Investigation, Software, Writing-Original Draft. **Teresa Donateo:** Conceptualization, Methodology, Writing-Review & Editing Supervision. **Antonio Ficarella:** Conceptualization, Writing-Review & Editing Supervision, Funds acquisition.

Acknowledgements

This study has been funded by the Italian Ministry for Education, University and Research and developed in collaboration with Aerospace Technological District (DTA) and AvioAero within project SMEA - *Diagnostic and Prognostic Methods and Sensors Development for the Health Monitoring in Aeronautic and Transport Applications*.

References

Airbus. (2021). *Micro-hybridisation: the next frontier to electrify flight?* (Retrieved on January 2022) https://www.airbus.com/en/newsroom/news/2021-09-micro-hybridisation-the-next-frontier-to-electrify-flight

Airbus. (2022). *Urban Air Mobility*. (Retrieved on February 2022) https://www.airbus.com/en/innovation/zero-emission/urban-air-mobility

Donateo, T., De Pascalis, C., Strafella, L., & Ficarella, A. (2021). Off-line and On-line Optimization of the Energy Management Strategy in a Hybrid Electric Helicopter for Urban Air-Mobility. *Aerospace Science and Technology*, 113.

Donateo, T., Terragno, A., & Ficarella, A. (2021). An optimized fuzzy logic for the energy management of a hybrid electric air-taxi. *76th ATI National Congress*. Rome, Italy.

Dubarry, M., & Liaw, B. (2009). Identify capacity fading mechanism in a commercial LiFePO4 cell. *Journal of Power Sources*, 194, 541–549.

EASA. (2022). *Urban Air Mobility* (UAM). (Retrieved on February 2022) https://www.easa.europa.eu/domains/urban-air-mobility-uam

FEV. (2022). *Urban Air Mobility - A game changer for smart cities*. (Retrieved on February 2022) https://uam.fev.com/

Guzzella, L., & Sciarretta, A. (2007). *Vehicle Propulsion Systems: Introduction to Modeling and Optimization*. Berlin, Germany: Springer.

Rendón, M. A., Sánchez R., C. D., Gallo M., J., & Anzai, A. H. (2021). Aircraft Hybrid-Electric Propulsion: Development Trends, Challenges and Opportunities. *Journal of Control, Automation and Electrical Systems*, 32(5), 1244-1268. https://doi.org/10.1007/s40313-021-00740-x

Roumeliotis, I., Mourouzidis, C., Zaffaretti, M., Pachidis, V., Broca, O., & Unlu, D. (2019). Assessmnet of Thermo-electric Power Plants for Rotorcraft Application. *Proceedings of ASME Turbo-Expo 2019: Turbomachinery Technical Conference and Exposition*. Phoenix, Arizona, USA.

Uber Elevate. (2016). *Fast-Forwarding to a Future of On-Demand Urban Air Transporation*. (Retrieved on September 2021) https://uberpubpolicy.medium.com/fast-forwarding-to-a-future-of-on-demand-urban-air-transportation-f6ad36950ffa

Wang, C., Li, Y., & Yang, B. (2017). Transient performance simulation of aircraft engine integrated with fuel and control systems. *Applied Thermal Engineering*, 114, 1029-1037.

Wortmann, G., Schmitz, O., & Hornung, M. (2014). Comparative assessment of transient characteristics of conventional and hybrid gas turbine engine. *CEAS Aeronautical Journal*, 5, 209-223.

International Journal of Aviation Science and Technology

Research Article

A Leader-Follower Trajectory Tracking Controller for Multi-Quadrotor Formation Flight

Diogo Ferreira[1], Paulo Oliveira[2], Afzal Suleman[3]

[1] *Instituto Superior Técnico, Lisbon, Portugal*
diogo.s.ferreira@tecnico.ulisboa.pt - 0000-0002-2904-8580

[2] *Instituto Superior Técnico, Department of Mechanical Engineering, Lisbon, Portugal*
paulo.j.oliveira@tecnico.ulisboa.pt - 0000-0002-5799-390X

[3] *University of Victoria, Department of Mechanical Engineering, Victoria, BC, Canada*
suleman@uvic.ca - 0000-0001-6498-2996

Abstract

The aim of this work is to design a control system based on modern control methods to control flight formations of quadrotor unmanned aerial vehicles. A leader-follower methodology is implemented where the leader vehicle has some predefined trajectory, and the follower vehicles are controlled in order to track the leader while keeping a constant displacement. The formation control system, responsible for the vehicle formation, considers, at first, only the motion at a constant height, and secondly, the three-dimensional motion. In both cases, the nonlinear control laws are derived based on Lyapunov stability theory and the Backstepping method. The control laws are validated in simulation, resorting to a realistic environment and vehicle models.

Keywords

Unmanned Aerial Vehicle
Leader-follower
Lyapunov stability
Backstepping

Time Scale of Article

Received 16 January 2022
Revised until 20 March 2022
Accepted 9 April 2022
Online date 28 June 2022

1. Introduction

Unmanned Air Vehicles (UAVs), which were originally developed for military purposes, have now been devoted to a myriad of other uses, ranging from aerial photography, goods delivery, agriculture, mapping and surveillance, pollution monitoring, or infrastructure inspections. When appropriately synchronized, a swarm of UAVs can perform much more complex tasks with gains in efficiency and robustness. As an example, (Bacelar, Cardeira, & Oliveira, 2019) describes how it is possible to deploy two UAVs to carry heavy loads cooperatively. (Rosalie, et al., 2017) presents a strategy for area exploration and mapping carried out by a swarm of autonomous UAVs. For policing and surveillance missions in areas where the communication range is limited, (Scherer & Rinner, 2020) discusses how efficient a network of UAVs can be in covering the area. For agriculture applications, (Ju & Son, 2018) delve deeply into the advantages of using multiple UAVs with distributed control for better performance.

Most of the examples shown apply different concepts of formation and resort to different techniques of how to control it. The control structure can be either centralized or decentralized. The centralized solutions rely on only one agent performing all computations and assigning the other agents their respective tasks. The centralized algorithms are generally easier to design but more difficult to implement due to the heavy computational burden. Also, communication is critical as

*: Corresponding Author Diogo Ferreira, diogo.s.ferreira@tecnico.ulisboa.pt
DOI: 10.23890/IJAST.vm03is01.0102

(Das, et al., 2002) consider that if the communication link between the central agent and any other agent fails, the entire formation is broken. The decentralized solutions break down the computational burden into smaller problems to be solved by each of the agents. In this case, the control laws are derived for each agent or subgroup of agents. The decentralized algorithms are expectedly more intricate to design, but their implementation is more reliable, efficient, and robust.

In terms of the approaches to formation control, the most relevant concepts are the leader-follower, the virtual leader, and the behavior-based. In the leader-follower case, as defined by (Shao, Xie, & Wang, 2007), a formation is achieved when each follower drives into the desired position with respect to the leader, which has some known trajectory. In the second case, the virtual leader describes a reference trajectory, and the formation is achieved when all the vehicles in the swarm follow the leader in a rigid structure, maintaining a rigid geometric shape with respect to one another and to a reference frame, according to (Leonard & Fiorelli, 2001). The behavior-based formation control approach defines different control behaviors for different situations of interest, and the control action for each vehicle is a weighted average of the control for each behavior, as explained by (Balch & Arkin, 1998).

Contrary to many strategies found in the literature, which define the displacement in the inertial frame, this paper implements this method for the 2D motion and expresses the displacement in the follower's body frame through decentralized onboard sensors. Moreover, given that the follower vehicles track a real-time reference provided by their controllers, they do not need any clue about the leader's path, which can be unparameterized. For the 3D case, a centralized approach has been chosen for computational efficiency.

2. Quadrotor Model

Let $\{I\}$ be an orthonormal reference frame according to the North-East-Down (NED) coordinate system, fixed at some point constant along the time. Let $\{B\}$ be another orthonormal reference frame centered at point $\boldsymbol{p}$. The orientation of $\{B\}$ with respect to $\{I\}$ is given by the roll, pitch, and yaw angles $\boldsymbol{\lambda} \coloneqq (\phi, \theta, \psi)$ that represent the rotation about their respective axes. The rotation matrix from $\{B\}$ to $\{I\}$ is given by an orthogonal matrix

$$\boldsymbol{R} \coloneqq \boldsymbol{R}(\boldsymbol{\lambda}) \in SO(3) = \{\boldsymbol{X} \in \mathbb{R}^{3\times3} : \boldsymbol{X}\boldsymbol{X}^T = \boldsymbol{X}^T\boldsymbol{X} = \boldsymbol{I}_3, |\boldsymbol{X}| = 1\}. \quad (1)$$

From the definition of $\boldsymbol{R}$, its derivative is $\dot{\boldsymbol{R}} = \boldsymbol{R}\boldsymbol{S}(\boldsymbol{\omega})$, with $\boldsymbol{\omega}$ the angular velocity of $\{B\}$ expressed in $\{B\}$. Let $\boldsymbol{p}$ be the quadrotor's position and $\boldsymbol{v}$ its velocity in $\{I\}$. The kinematics of the rigid body, for any $\theta \neq (2k+1)\frac{\pi}{2}, \forall k \in \mathbb{Z}$, can be written as

$$\begin{cases} \dot{\boldsymbol{p}} = \boldsymbol{v} \\ \dot{\boldsymbol{\lambda}} = \boldsymbol{Q}(\boldsymbol{\lambda})\boldsymbol{\omega} \end{cases} \quad (2)$$

with

$$\boldsymbol{Q}(\boldsymbol{\lambda}) = \begin{pmatrix} 1 & \sin\phi\tan\theta & \cos\phi\tan\theta \\ 0 & \cos\phi & -\sin\phi \\ 0 & \frac{\sin\phi}{\cos\theta} & \frac{\cos\phi}{\cos\theta} \end{pmatrix}. \quad (3)$$

Let m be the mass of the quadrotor and $J \in \mathbb{R}^{3\times3}$ its inertia tensor. From the conservation of linear and angular momentum in inertial frames, the complete dynamics of the rigid body in $\{I\}$ is given by

$$\begin{cases} m\dot{\boldsymbol{v}} = \boldsymbol{f} \\ \boldsymbol{J}\dot{\boldsymbol{\omega}} = -\boldsymbol{S}(\boldsymbol{\omega})\boldsymbol{J}\boldsymbol{\omega} + \boldsymbol{n} \end{cases} \quad (4)$$

where $\boldsymbol{f}$ is the sum of external forces applied on the quadrotor expressed in $\{I\}$ and $\boldsymbol{n}$ the sum of external moments expressed in $\{B\}$ and $\boldsymbol{S}(\boldsymbol{\omega})$ is a skew-symmetric matrix such that $\boldsymbol{S}(\boldsymbol{x})\boldsymbol{y} = \boldsymbol{x} \times \boldsymbol{y}$ for any $\boldsymbol{x}, \boldsymbol{y} \in \mathbb{R}^3$.

A quadrotor is made of two pairs of counter-rotating rotors, assumed equal and equally spaced, as represented in figure 1. The forces applied on the quadrotor include its weight, aligned with the inertial frame z axis pointing downwards, and the total thrust force $T = \sum_{i=1}^{4} T_i$ along the body z axis, pointing upwards. Relative to $\{I\}$, it is given by

$$\boldsymbol{f} = mg\boldsymbol{e_3} - T\boldsymbol{R}\boldsymbol{e}_3 \quad (5)$$

The moments applied on the quadrotor originated from the different thrust forces produced by each rotor and the reaction torque generated by the rotors rotating. For the purpose of this work, which by no means intends to be a fastidious description of the quadrotor dynamics, the thrust force and reaction torque of each rotor are assumed proportional to its angular speed squared, such that the sum of external moments relative to $\{B\}$ is

$$\boldsymbol{n} = \begin{pmatrix} 0 & l & 0 & -l \\ l & 0 & -l & 0 \\ \frac{c_Q}{c_T} & -\frac{c_Q}{c_T} & \frac{c_Q}{c_T} & -\frac{c_Q}{c_T} \end{pmatrix} \begin{pmatrix} T_1 \\ T_2 \\ T_3 \\ T_4 \end{pmatrix} \quad (6)$$

where l is the quadrotor radius, i.e. the distance between the center of mass and the center of each rotor.

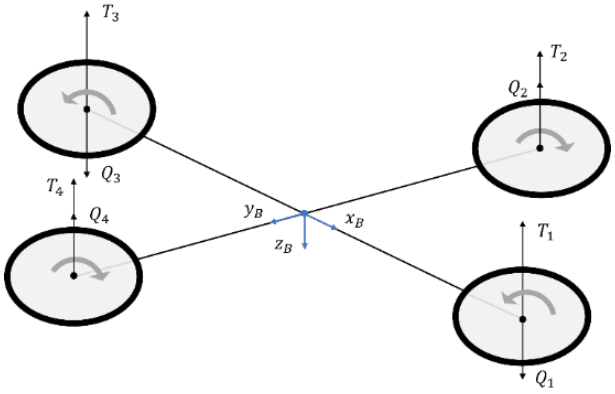

Fig. 1. Simplified representation of a quadrotor with forces and moments on each rotor.

3.Horizontal Formation Control

A trajectory tracking controller is implemented to make the follower track the leader while keeping a constant offset in its reference frame. Assuming the motion at constant height, Eqs. (2) and (4) can be simplified for a purely kinematic model given by

$$\begin{cases} \dot{x} = u\cos\psi - v\sin\psi \\ \dot{y} = u\sin\psi + v\cos\psi \\ \dot{\psi} = r \end{cases} \quad (7)$$

with only two independent equations. Given that we ultimately wish to control the force and the torque, it is wise to select the input vector $(\dot{u}, \dot{r})^T$ (or alternatively $(\dot{v}, \dot{r})^T$). So, the kinematics can also be written as

$$\begin{cases} \dot{\boldsymbol{p}} = \boldsymbol{R}\boldsymbol{v} \\ \dot{\psi} = r \end{cases} \quad (8)$$

with $\boldsymbol{v} \coloneqq v\boldsymbol{e}_1$ the horizontal velocity and $\boldsymbol{R} \coloneqq \boldsymbol{R}(\psi)$ the horizontal rotation matrix from the body-fixed reference frame to the inertial frame. If $\boldsymbol{\Delta} = (\Delta_x, \Delta_y)^T$ is the desired displacement and $\boldsymbol{p}, \boldsymbol{c} \in \mathbb{R}^2$ the follower's and leader's positions, respectively, the position error $\boldsymbol{z}_1 \in \mathbb{R}^2$, expressed in the follower's reference frame, can be written as

$$\boldsymbol{z}_1 = \boldsymbol{R}^T(\boldsymbol{c} - \boldsymbol{p}) - \boldsymbol{\Delta} \quad (9)$$

and its derivative as

$$\dot{\boldsymbol{z}}_1 = \boldsymbol{R}^T\dot{\boldsymbol{c}} - \boldsymbol{v} - \boldsymbol{S}(r)(\boldsymbol{z}_1 + \boldsymbol{\Delta}). \quad (10)$$

An equilibrium point different from zero $\boldsymbol{z}_e \in \mathbb{R}^2$ for the error system above makes $\dot{\boldsymbol{z}}_1 = 0$. By making the appropriate change of coordinates, one can obtain the error system with an equilibrium point at the origin. We now want to derive a control law to stabilize the system around this equilibrium point. Let $V_1: \mathbb{R}^2 \to \mathbb{R}$ be a continuously differentiable Lyapunov function such that $V_1(0) = 0, V_1(\boldsymbol{z}_1) > 0 \forall \boldsymbol{z}_1 \neq 0$ and $\|\boldsymbol{z}_1\| \to \infty \Rightarrow V_1(\boldsymbol{z}_1) \to \infty$ given by $V_1 = 1/2\,\|z_1\|^2$. Its derivative is

$$\dot{V}_1 = \boldsymbol{z}_1^T(\boldsymbol{R}^T\dot{\boldsymbol{c}} - \boldsymbol{v} - \boldsymbol{S}(r)\boldsymbol{\Delta}) \quad (11)$$

Adding and subtracting a term $k_1\|\boldsymbol{z}_1\|^2$ yields

$$\dot{V}_1 = k_1\|\boldsymbol{z}_1\|^2 + \boldsymbol{z}_1^T\boldsymbol{z}_2 \quad (12)$$

where a new error $\boldsymbol{z}_2 = k_1\boldsymbol{z}_1 + \boldsymbol{R}^T\dot{\boldsymbol{c}} - \boldsymbol{v} - \boldsymbol{S}(r)\boldsymbol{\Delta}$ was introduced. To apply backstepping with one step, we define the continuously differentiable Lyapunov function $V_2: \mathbb{R}^4 \to \mathbb{R}$ such that $V_2(0) = 0, V_2(\boldsymbol{z}_1, \boldsymbol{z}_2) > 0 \forall (\boldsymbol{z}_1, \boldsymbol{z}_2) \neq 0$ and $\|(\boldsymbol{z}_1, \boldsymbol{z}_2)\| \to \infty \Rightarrow V_2(\boldsymbol{z}_1, \boldsymbol{z}_2) \to \infty$ given by $V_2(\boldsymbol{z}_1, \boldsymbol{z}_2) = V_1(\boldsymbol{z}_1) + 1/2\,\|\boldsymbol{z}_2\|^2$. Its derivative is

$$\dot{V}_2 = \dot{V}_1 + \boldsymbol{z}_2^T\left[k_1\dot{\boldsymbol{z}}_1 + \boldsymbol{R}^T\ddot{\boldsymbol{c}} - \boldsymbol{S}(r)\boldsymbol{R}^T\dot{\boldsymbol{c}} - \begin{pmatrix} 1 & -\Delta_y \\ 0 & \Delta_x \end{pmatrix}\begin{pmatrix} \dot{v} \\ \dot{r} \end{pmatrix}\right] \quad (13)$$

If the accelerations $\dot{v}, \dot{r}$ are considered inputs of the system, the control law should be

$$\begin{pmatrix} \dot{v} \\ \dot{r} \end{pmatrix} = \begin{pmatrix} 1 & -\Delta_y \\ 0 & \Delta_x \end{pmatrix}^{-1}(k_1\dot{\boldsymbol{z}}_1 + \boldsymbol{R}^T\ddot{\boldsymbol{c}} - \boldsymbol{S}(r)\boldsymbol{R}^T\dot{\boldsymbol{c}} + \boldsymbol{z}_1 + k_2\boldsymbol{z}_2) \quad (14)$$

which is well-defined for $\Delta_x \neq 0$. Under this control law, the error system can be written in the strict-feedback form (Khalil, 2014) as

$$\begin{cases} \dot{\boldsymbol{z}}_1 = -(\boldsymbol{S}(r) + k_1\boldsymbol{I}_2)\boldsymbol{z}_1 + \boldsymbol{z}_2 \\ \dot{\boldsymbol{z}}_2 = -\boldsymbol{z}_1 - k_2\boldsymbol{z}_2 \end{cases} \quad (15)$$

and the derivative of V_2 becomes

$$\dot{V}_2 = -k_1\|\boldsymbol{z}_1\|^2 - k_2\|\boldsymbol{z}_2\|^2 \quad (16)$$

which is negative for $(\boldsymbol{z}_1, \boldsymbol{z}_2) \neq 0$ if $k_1, k_2 > 0$. Thus, according to the Barbashin-Krasovskii theorem (Khalil, 2014), the error system is globally asymptotically stable around the origin.

Consider the existence of an unknown external acceleration disturbance $\boldsymbol{d} \in \mathbb{R}^2$ expressed in {B} such that

$$\dot{\boldsymbol{z}}_2 = k_1\dot{\boldsymbol{z}}_1 + \boldsymbol{R}^T\ddot{\boldsymbol{c}} - \boldsymbol{S}(r)\boldsymbol{R}^T\dot{\boldsymbol{c}} - \dot{\boldsymbol{v}} - \boldsymbol{S}(\dot{r})\boldsymbol{\Delta} + \boldsymbol{R}\boldsymbol{d} \quad (17)$$

Additionally, assume the controller has an estimator $\hat{\boldsymbol{d}} \in \mathbb{R}^2$ such that

$$\begin{pmatrix} \dot{v} \\ \dot{r} \end{pmatrix} = \begin{pmatrix} 1 & -\Delta_y \\ 0 & \Delta_x \end{pmatrix}^{-1}(k_1\dot{\boldsymbol{z}}_1 + \boldsymbol{R}^T\ddot{\boldsymbol{c}} - \boldsymbol{S}(r)\boldsymbol{R}^T\dot{\boldsymbol{c}} + \boldsymbol{z}_1 + k_2\boldsymbol{z}_2 + \boldsymbol{R}\hat{\boldsymbol{d}}) \quad (18)$$

Expressing the estimation error by $\tilde{\boldsymbol{d}} = \boldsymbol{d} - \hat{\boldsymbol{d}}$ and the error state $\boldsymbol{z} = (\boldsymbol{z}_1, \boldsymbol{z}_2)^T$, the error dynamics can be written in state-space as $\dot{\boldsymbol{z}} = \boldsymbol{A}\boldsymbol{z} + \boldsymbol{B}\tilde{\boldsymbol{d}}$ with

$$\boldsymbol{A} = \begin{pmatrix} -(\boldsymbol{S}(r) + k_1\boldsymbol{I}_2) & \boldsymbol{I}_2 \\ -\boldsymbol{I}_2 & -k_2\boldsymbol{I}_2 \end{pmatrix}$$

and

$$\boldsymbol{B} = \begin{pmatrix} 0_{2\times 2} \\ \boldsymbol{R} \end{pmatrix}$$

Let $V_3: \mathbb{R}^6 \to \mathbb{R}$ be a continuously differentiable Lyapunov function such that $V_3(0) = 0, V_3(\boldsymbol{z}, \tilde{\boldsymbol{d}}) > 0 \forall (\boldsymbol{z}, \tilde{\boldsymbol{d}}) \neq 0$ and $\|(\boldsymbol{z}, \tilde{\boldsymbol{d}})\| \to \infty \Rightarrow V_3(\boldsymbol{z}, \tilde{\boldsymbol{d}}) \to \infty$ given by $V_3(\boldsymbol{z}, \tilde{\boldsymbol{d}}) = V_2(\boldsymbol{z}) + \frac{1}{2k_d}\|\tilde{\boldsymbol{d}}\|^2$. Its derivative is

$$\dot{V}_3(\boldsymbol{z}, \tilde{\boldsymbol{d}}) = \boldsymbol{z}^T\boldsymbol{A}\boldsymbol{z} + \boldsymbol{z}^T\boldsymbol{B}\tilde{\boldsymbol{d}} + \frac{1}{k_d}\tilde{\boldsymbol{d}}^T\dot{\tilde{\boldsymbol{d}}} \quad (19$$

The first term of $\dot{V}_3$ is negative for all $\boldsymbol{z} \neq 0$ as it has already been proved the error system converges under the control law from Eq. (14). As of the remaining two terms, $\dot{V}_3$ gets negative for all $(\boldsymbol{z}, \tilde{\boldsymbol{d}}) \neq 0$ if they sum to zero. If the disturbance is assumed constant, then $\dot{\tilde{\boldsymbol{d}}} = -\dot{\hat{\boldsymbol{d}}}$ and the adaptation law for the estimator is

$$\dot{\hat{\boldsymbol{d}}} = k_d\boldsymbol{B}^T\boldsymbol{z} \quad (20)$$

Now that we have the tracking control and the disturbance estimation, we must study the stability of the system comprised of both the position error and the disturbance estimation error simultaneously. This system is given by

$$\begin{pmatrix} \dot{\boldsymbol{z}} \\ \dot{\tilde{\boldsymbol{d}}} \end{pmatrix} = \begin{pmatrix} \boldsymbol{A} & \boldsymbol{B} \\ -k_d \boldsymbol{B}^T & 0_{2\times 2} \end{pmatrix} \begin{pmatrix} \boldsymbol{z} \\ \tilde{\boldsymbol{d}} \end{pmatrix} \tag{21}$$

Let $\Omega = \{(\boldsymbol{z}, \tilde{\boldsymbol{d}}) \in \mathbb{R}^6 : V_3(\boldsymbol{z}, \tilde{\boldsymbol{d}}) \leq c\}$ for any $c \in \mathbb{R}^+$. The set Ω is bounded since V_3 is radially unbounded and, from Lyapunov's direct method (Khalil, 2014), it is positively invariant with respect to the dynamics (21). Let E be the set of all points in Ω where $\dot{V}_3(\boldsymbol{z}, \tilde{\boldsymbol{d}}) = 0$. This set is given by $E = \{(\boldsymbol{z}, \tilde{\boldsymbol{d}}) \in \mathbb{R}^6 : \boldsymbol{z} = 0\}$. Let M be the largest invariant set contained in E. By LaSalle's theorem (Khalil, 2014), every solution with the initial condition in Ω approaches M as $t \to \infty$. Since for any $(\boldsymbol{z}, \tilde{\boldsymbol{d}}) \in \mathbb{R}^6$ there exists a $c > 0$ such that $(\boldsymbol{z}, \tilde{\boldsymbol{d}}) \in \Omega$, we have that any solution converges to M. From its invariance, we have that $\dot{\boldsymbol{z}} = 0 \Leftrightarrow \tilde{\boldsymbol{d}} = \boldsymbol{0_{2\times 1}}$ for all $(\boldsymbol{z}, \tilde{\boldsymbol{d}}) \in M$. Therefore, $(\boldsymbol{z}, \tilde{\boldsymbol{d}}) = 0$ is the only element in M and the system is globally asymptotically stable around the origin.

3.1. Closed-loop system

After deriving a control law, it is of interest to study the stability of the closed-loop system, i.e., the formation of one leader and one follower. When the position error is identically zero, $\boldsymbol{z}_1 = \dot{\boldsymbol{z}}_1 = 0$, and Eq. (10) becomes

$$\boldsymbol{R}^T \dot{\boldsymbol{c}} - \boldsymbol{v} - \boldsymbol{S}(r)\boldsymbol{\Delta} = 0. \tag{22}$$

Assuming a general leader's trajectory $\dot{c} = C(cos\,\psi_c, sin\,\psi_c)^T$, the closed-loop equation (22) can be expanded to isolate the control variables as

$$\begin{pmatrix} v \\ r \end{pmatrix} = \begin{pmatrix} C\cos(\psi - \psi_c) - C\Delta_y/\Delta_x \sin(\psi - \psi_c) \\ -C/\Delta_x\, sin(\psi - \psi_c) \end{pmatrix}. \tag{23}$$

These equations describe a nonlinear periodic system with dynamics for ψ and output v. It is asymptotically stable around the points

$$\psi^* = \psi_c + 2k\pi, \quad \forall k \in \mathbb{Z} \tag{24}$$

within the region of convergence

$$\psi \in]\psi_c + (2k-1)\pi, \psi_c + (2k+1)\pi[, \quad \forall k \in \mathbb{Z} \tag{25}$$

In conclusion, the follower can have a heading difference relative to the leader of up to 180°. The bigger the difference, the slower the convergence is to the desired heading. In the limit, if a follower is set to track a leader describing a linear path, starting in the opposite heading, it will not converge.

4. Three-dimensional Formation Control

The motion of the quadrotor at constant height has been studied, and a controller for the simplified model has been derived using the backstepping method applied to the position error. This method is now used to derive a similar nonlinear controller for the complete model. The dynamics from Eqs. (2) and (4) can be written in a state-space form $\dot{\boldsymbol{X}} = f(\boldsymbol{X}, \boldsymbol{U})$ by introducing the state vector $\boldsymbol{X} = (\phi, \dot{\phi}, \theta, \dot{\theta}, \psi, \dot{\psi}, z, \dot{z}, x, \dot{x}, y, \dot{y})$ and the input vector $\boldsymbol{U} = (T, n_x, n_y, n_z)$, according to (Bouabdallah & Siegwart, 2005). Defining the constants $a_\phi = (J_y - J_z)/J_x$, $a_\theta = (J_z - J_x)/J_y$, $a_\psi = (J_x - J_y)/J_z$, $b_\phi = 1/J_x$, $b_\theta = 1/J_y$ and $b_\psi = 1/J_z$, the dynamics becomes

$$f(X,U) = \begin{cases} \dot{\phi} \\ a_\phi \dot{\theta}\dot{\psi} + b_\phi n_x \\ \dot{\theta} \\ a_\theta \dot{\phi}\dot{\psi} + b_\theta n_y \\ \dot{\psi} \\ a_\psi \dot{\phi}\dot{\theta} + b_\psi n_z \\ \dot{z} \\ g - T/m\, cos\,\phi\, cos\,\theta \\ \dot{x} \\ T/m\, u_x \\ \dot{y} \\ T/m\, u_y \end{cases} \tag{26}$$

with $u_x = cos\,\phi\, sin\,\theta\, cos\,\psi + sin\,\phi\, sin\,\psi$ and $u_y = cos\,\phi\, sin\,\theta\, sin\,\psi - sin\,\phi\, cos\,\psi$. The system as it is posed highlights an important relationship between the position and attitude of the quadrotor: the position components depend on the angles; however, the opposite is not true. In other words, the way the position evolves is a consequence of the attitude of the quadrotor. However, the attitude is oblivious to its position. The overall system can be thought of as the result of two semi-decoupled subsystems: the translation and the rotation – for which two controllers are designed separately.

4.1. Attitude Control

Let $z_\phi = \phi_{ref} - \phi \in \mathbb{R}$ be the roll angle error. Let $V_\phi : \mathbb{R} \to \mathbb{R}$ be a continuously differentiable Lyapunov function such that $V_\phi(0) = 0, V_\phi(z_\phi) > 0 \forall z_\phi \neq 0$ and $\|z_\phi\| \to \infty \Rightarrow V_\phi(z_\phi) \to \infty$ given by $V_\phi = 1/2\,\|z_\phi\|^2$. Its derivative is

$$\dot{V}_\phi = z_\phi(\dot{\phi}_{ref} - \dot{\phi}) \tag{27}$$

If $\dot{\phi}$ is controlled to be

$$\dot{\phi} = \dot{\phi}_{ref} + k_\phi z_\phi \tag{28}$$

then $\dot{V}_\phi = -k_\phi z_\phi^2$. Let now $z_{\dot{\phi}} \in \mathbb{R}$ be the roll rate error given by

$$z_{\dot{\phi}} = \dot{\phi} - \dot{\phi}_{\text{ref}} - k_\phi z_\phi \tag{29}$$

and the augmented Lyapunov function $V_{\dot{\phi}} : \mathbb{R}^2 \to \mathbb{R}$, in the same conditions as above, given by

$$z_{\dot{\phi}} = \dot{\phi} - \dot{\phi}_{\text{ref}} - k_\phi z_\phi \tag{30}$$

with its derivative given by

$$\dot{V}_{\dot{\phi}} = -k_\phi z_\phi^2 + z_{\dot{\phi}}(a_\phi \dot{\theta}\dot{\psi} + b_\phi n_x - \ddot{\phi}_{ref} - k_\phi \dot{z}_\phi). \tag{31}$$

If the control law for n_x is chosen to be

$$n_x = 1/b_\phi(\ddot{\phi}_{ref} + k_\phi \dot{z}_\phi - a_\phi \dot{\theta}\dot{\psi} - k_{\dot{\phi}} z_{\dot{\phi}}), \tag{32}$$

Then

$$\dot{V}_{\dot{\phi}} = -k_{\phi} z_{\phi}^2 - k_{\dot{\phi}} z_{\dot{\phi}}^2, \tag{33}$$

which is negative for $(z_{\phi}, z_{\dot{\phi}}) \neq 0$ if $k_{\phi}, k_{\dot{\phi}} > 0$. Thus, according to the Barbashin-Krasovskii theorem (Khalil, 2014), the roll error system is globally asymptotically stable around the origin. Following the same backstepping procedure for the remaining angular variables, an attitude controller is derived as

$$\begin{cases} n_x = 1/b_{\phi}\left(\ddot{\phi}_{ref} + k_{\phi}\dot{z}_{\phi} - a_{\phi}\dot{\theta}\dot{\psi} - k_{\dot{\phi}} z_{\dot{\phi}}\right) \\ n_y = 1/b_{\theta}\left(\ddot{\theta}_{ref} + k_{\theta}\dot{z}_{\theta} - a_{\theta}\dot{\phi}\dot{\psi} - k_{\dot{\theta}} z_{\dot{\theta}}\right) \\ n_z = 1/b_{\psi}\left(\ddot{\psi}_{ref} + k_{\psi}\dot{z}_{\psi} - a_{\psi}\dot{\phi}\dot{\theta} - k_{\dot{\psi}} z_{\dot{\psi}}\right) \end{cases} \tag{34}$$

with gains $k_{\phi}, k_{\dot{\phi}}, k_{\theta}, k_{\dot{\theta}}, k_{\psi}, k_{\dot{\psi}} > 0$.

As stated in Section 2, the quadrotor model is well defined for any $\theta \neq (2k+1)\frac{\pi}{2}, \forall k \in \mathbb{Z}$. It is important to remember that, because of the singularities of the Euler angles and the topological limitations of $SO(3)$ group, this attitude controller is almost globally stable.

4.2. Position Control

A similar backstepping approach will next be followed for controlling the quadrotor position. Let $z_z = z_{ref} - z \in \mathbb{R}$ be the altitude error. Let $V_{\phi} = 1/2 z_z^2$ be a Lyapunov function, in the same conditions as above, with derivative

$$\dot{V}_z = z_z(\dot{z}_{ref} - \dot{z}) \tag{35}$$

If $\dot{z}$ is controlled to be

$$\dot{z} = \dot{z}_{ref} + k_z z_z \tag{36}$$

then $\dot{V}_z = -k_z z_z^2$. Let now $z_{\dot{z}}$ be the vertical speed error given by

$$z_{\dot{z}} = \dot{z} - \dot{z}_{ref} - k_z z_z \tag{37}$$

and the augmented Lyapunov function $V_{\dot{z}}: \mathbb{R}^2 \to \mathbb{R}$, in the same conditions as above, given by

$$V_{\dot{z}} = V_z + 1/2 z_{\dot{z}}^2 \tag{38}$$

with its derivative given by

$$\dot{V}_{\dot{z}} = -k_z z_z^2 + z_{\dot{z}}(g - T/m \cos\phi \cos\theta - \ddot{z}_{ref} - k_z \dot{z}_z). \tag{39}$$

If the control law for T is chosen to be

$$T = m/(\cos\phi \cos\theta)(g - \ddot{z}_{ref} - k_z \dot{z}_z - k_{\dot{z}} z_{\dot{z}}), \tag{40}$$

Then

$$\dot{V}_{\dot{z}} = -k_z z_z^2 - k_{\dot{z}} z_{\dot{z}}^2 \tag{41}$$

which is negative for $(z_z, z_{\dot{z}}) \neq 0$ if $k_z, k_{\dot{z}} > 0$. Thus, according to the Barbashin-Krasovskii theorem (Khalil, 2014), the altitude error system is globally asymptotically stable around the origin. Following the same backstepping procedure for the remaining position variables, a position controller is derived as

$$\begin{cases} T = m/(\cos\phi \cos\theta)\left(g - \ddot{z}_{ref} - k_z \dot{z}_z - k_{\dot{z}} z_{\dot{z}}\right) \\ u_x = m/T(\ddot{x}_{ref} + k_x \dot{z}_x - k_{\dot{x}} z_{\dot{x}} \\ u_y = m/T(\ddot{y}_{ref} + k_y \dot{z}_y - k_{\dot{y}} z_{\dot{y}} \end{cases} \tag{42}$$

with gains $k_x, k_{\dot{x}}, k_y, k_{\dot{y}}, k_z, k_{\dot{z}} > 0$.

To feed the attitude controller with the roll and pitch reference values, it is assumed the quadrotor does not perform complex maneuvers, thereby keeping ϕ and θ small enough. From the definitions of u_x and u_y it can be written

$$\begin{pmatrix} \theta_{ref} \\ \phi_{ref} \end{pmatrix} = \begin{pmatrix} \cos\psi & \sin\psi \\ \sin\psi & -\cos\psi \end{pmatrix} \begin{pmatrix} u_x \\ u_y \end{pmatrix} \tag{43}$$

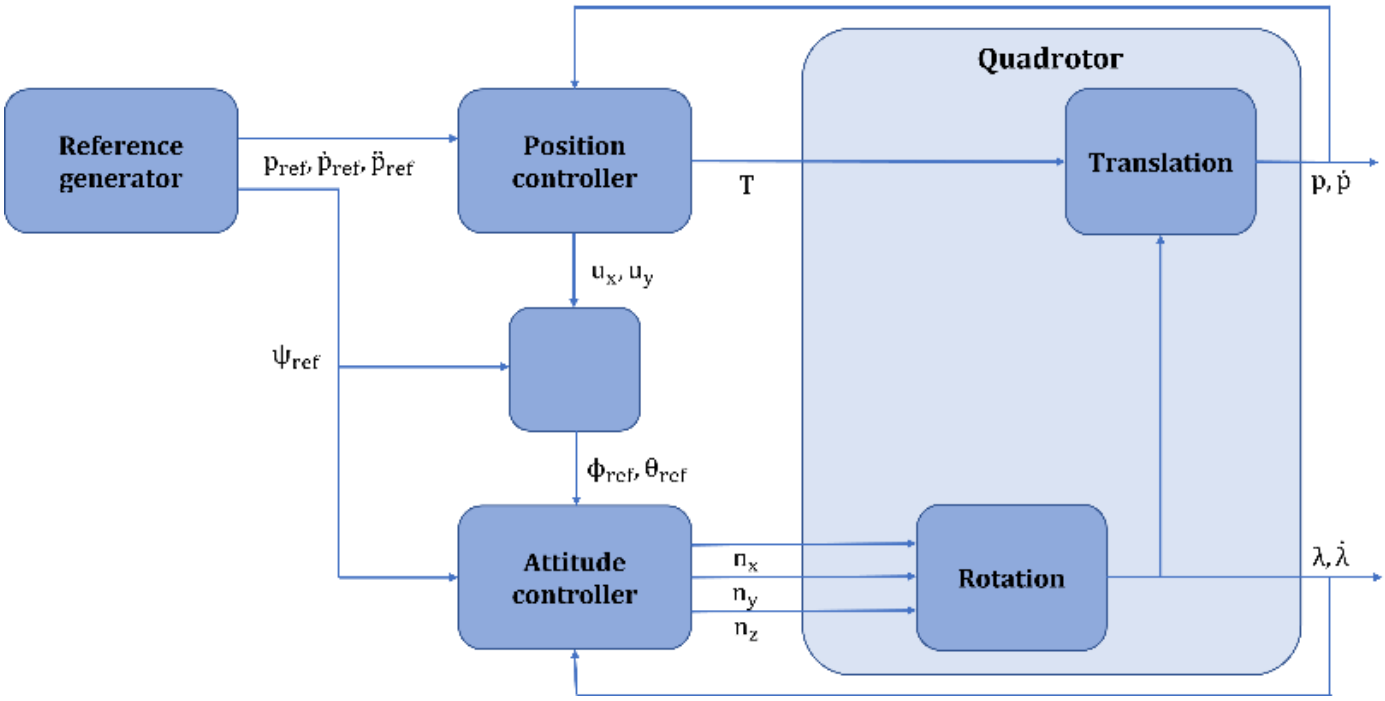

Fig. 2. 3D controller scheme.

The attitude controller also requires the derivative and second derivative of the reference Euler angles. These derivatives could be explicitly computed from the system (43); however, that would require measurements of the acceleration and its derivative, which are in all likelihood unavailable. Numerical differentiation of the reference roll and pitch is suggested by (Alcocer, Valenzuela, & Colorado, 2016) and adapted to

$$\dot{\phi}_{ref} \approx \frac{\phi_{ref}(t)-\phi_{ref}(t-\Delta t)}{\Delta t} \quad (44)$$

And

$$\dot{\theta}_{ref} \approx \frac{\theta_{ref}(t)-\theta_{ref}(t-\Delta t)}{\Delta t} \quad (45)$$

respectively, where Δt is the sampling period. The second derivative of the reference angles can be computed likewise. The controller scheme is depicted in Fig. 2.

5. Simulation Results

Several simulations have been carried out for the developed architectures. This section presents an illustrative simulation for both the 2D and 3D controllers, where the physical parameters are shown in SI units.

The first simulation consists of a formation of two vehicles – one leader and one follower – in the two-dimensional space. The follower is intended to track a leader in a circular path with a radius $2\,m$ and angular speed $1\,m/s$. The displacement is $\Delta = (1,1)$ and the gains are $k_1 = k_2 = k_d = 0.5$. The disturbance intensity is $d = (1,1)$. Figure 3 shows the simulation position as the follower starts from outside the leader's circle and converges to a trajectory where it sees the leader at the position (1,1) in its reference frame. Position and estimation error convergence is guaranteed after about 10 seconds. Figure 4 shows the speed convergence for a uniform circular motion and the heading angle bounded between $-180°$ and $180°$.

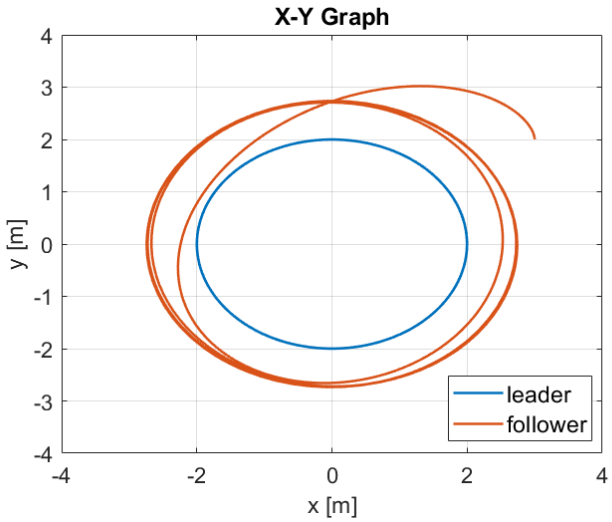

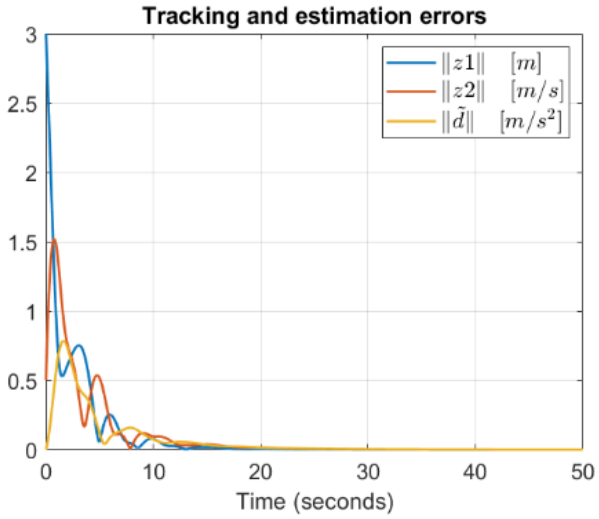

Fig.3. 2D simulation – position and tracking and estimation error.

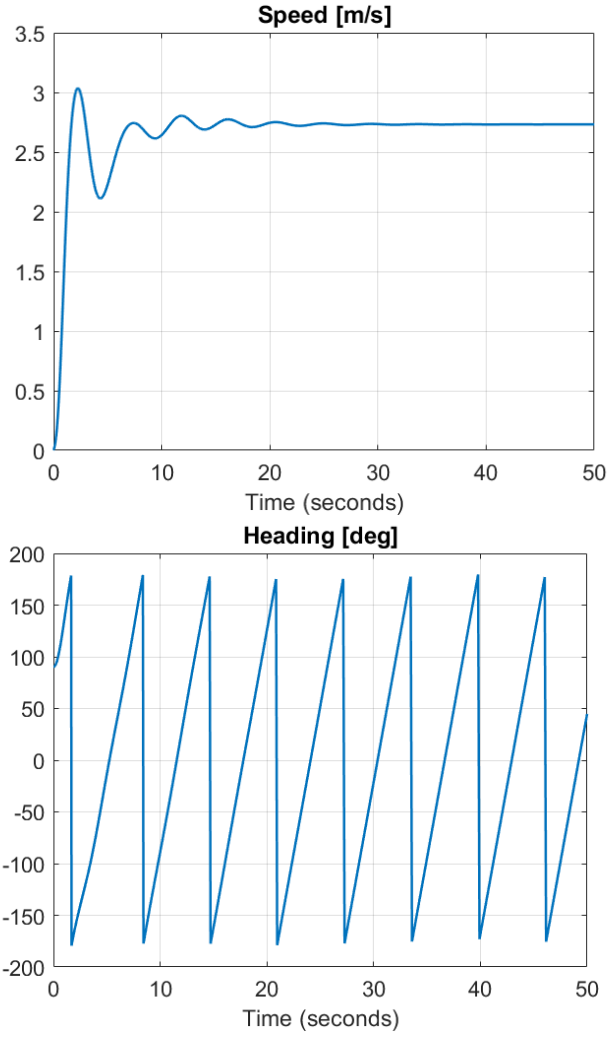

Fig.4. 2D simulation – speed and heading angle.

For the three-dimensional case, the complete model simulation considers a formation of one leader and two followers, each of them with equal controllers and departing from the same place. The heavy quadrotor model developed by (Pounds, Mahony, & Corke, 2010) was used. The attitude gains are all equal to 1, and the

position gains are $k_x = k_y = 2.2, k_{\dot{x}} = k_{\dot{y}} = 0.18, k_z = 0.5, k_{\dot{z}} = 0.2$. The first follower keeps a displacement of $\Delta_1 = (1,1,0)$ and the second follower keeps a displacement of $\Delta_2 = (2,2,0)$. White Gaussian noise is added to the sensors of the followers with a signal-to-noise ratio equal to 45 dB. Figure 5 displays the position of the vehicles and the actuation on each rotor, respectively, for a 100-second simulation. It is possible to see the thrust forces for each rotor converging to a constant value as the quadrotor tilts and banks. Figure 6 shows the horizontal speed – converging to a uniform circular motion at constant height – and the distance from the followers to the leader at each time instant. This plot converges to the desired value after 50 seconds, which bears testimony to the fact that the position error system converges to zero.

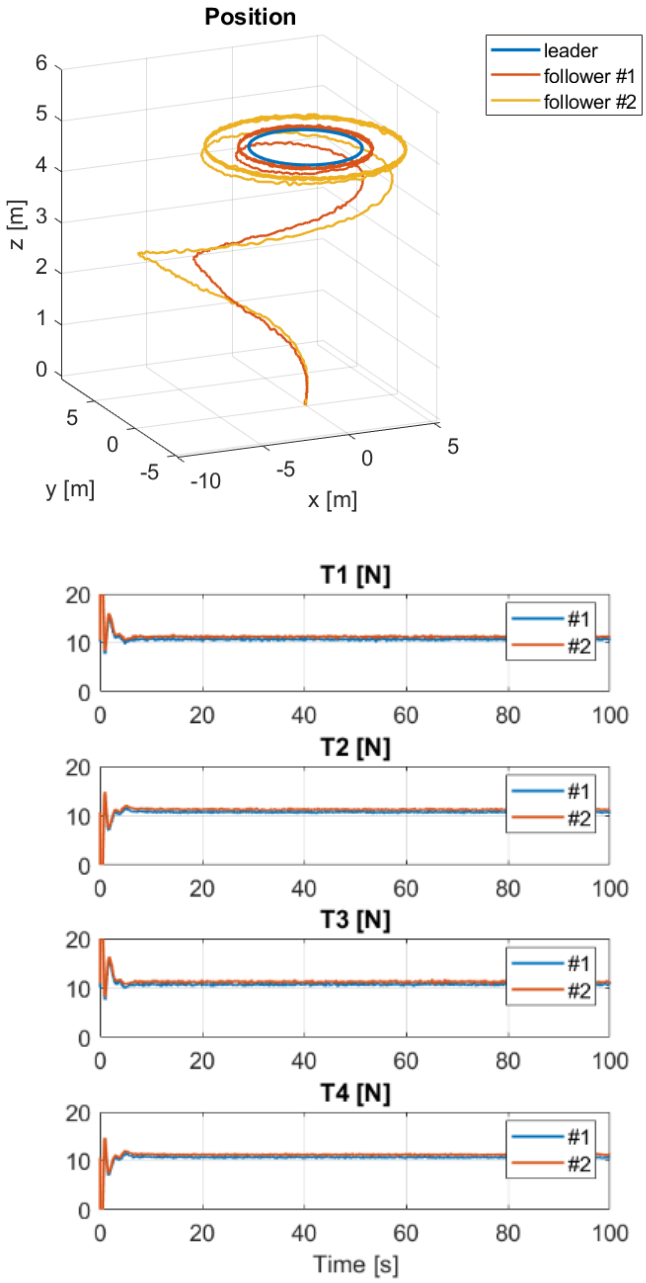

Fig.5. 3D simulation – position and actuation.

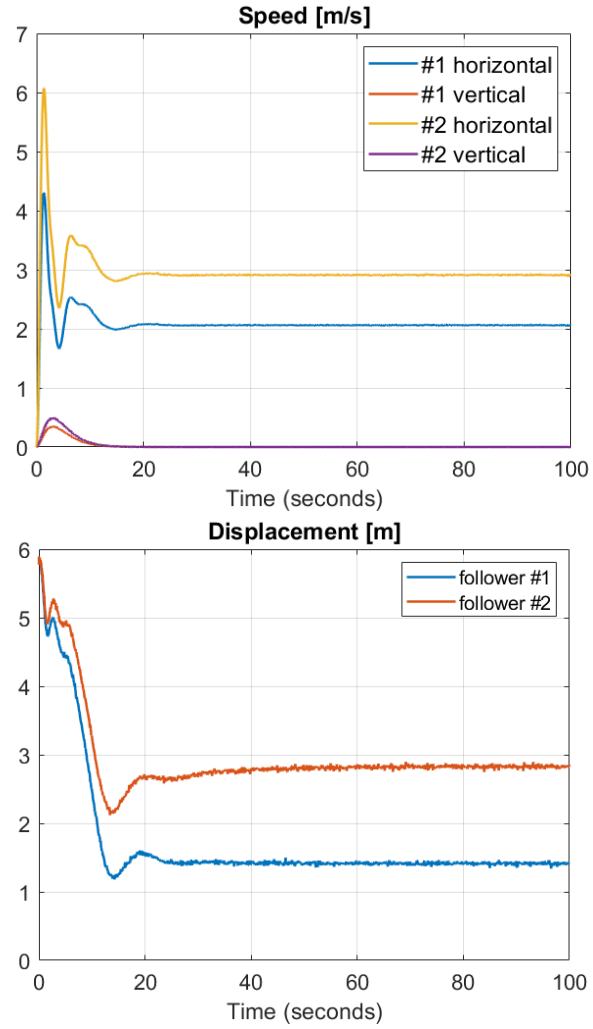

Fig.6. 3D simulation – speed and displacement.

It is important to recall the assumption that the noise is both white and Gaussian. In fact, this assumption, however suitable for the simulation under analysis, is not completely accurate in a real environment. Firstly, the real noise is never completely white because the power spectral density is not necessarily constant for all frequencies. Secondly, the real noise is never completely Gaussian, given that a Gaussian distribution allows infinite frequency values, which is certainly not verifiable in a physical environment.

6. Concluding Remarks

This work proposes an approach to the problem of flight formation by solving the trajectory tracking problem of quadrotor unmanned aerial vehicles. The formation is conceived as a leader vehicle being followed by a follower vehicle that keeps a constant displacement between them. The backstepping method has been applied to derive nonlinear control laws, and the stability concerns have been addressed through Lyapunov stability theory.

The control solution is twofold. Firstly, only the motion at constant height was considered. In this case, the

controller is purely kinematic but robust to constant acceleration disturbances, and the stability of the error system is globally asymptotic. The dynamic behavior of a closed-loop formation comprised of one leader and one follower is shown to be periodic. A formal proof of asymptotic stability within a certain region of convergence is also provided for this closed loop.

Secondly, a complete three-dimensional model was considered. This model is both kinematic and dynamic and takes into account the relevant inputs from the rotors spinning. The error system is also proved globally asymptotically stable.

A relevant simulation study has been carried out to attest to the performance of the control laws developed previously. For the motion at a constant height, the follower was intended to track a leader in a circular path. For the complete model simulation, two followers take part in the formation with noisy measurements from the sensors.

Possible avenues for future work could include validation in real quadcopters, estimating variables unavailable to the followers, incorporating collision avoidance techniques, and applying varying disturbances.

CRediT Author Statement

Diogo Ferreira: Conceptualization, Methodology, Software, Validation, Investigation, Writing – Original Draft. **Paulo Oliveira**: Conceptualization, Writing – Review & Editing, Supervision. **Afzal Suleman**: Conceptualization, Writing – Review & Editing, Supervision.

References

Alcocer, R., Valenzuela, J., & Colorado, R. (2016). A robust approach for trajectory tracking control of a quadrotor with experimental validation. *ISA Transactions*, 65, 262-274.

Bacelar, T., Cardeira, C., & Oliveira, P. (2019). Cooperative Load Transportation with Quadrotors. *IEEE International Conference on Autonomous Robot Systems and Competions*, (pp. 1-6).

Balch, T., & Arkin, R. (1998). Behavior-based formation control for multirobot teams. *IEEE Transactions on Robotics and Automation*, 14, 926-939.

Bouabdallah, S., & Siegwart, R. (2005). Backstepping and Sliding-Mode Techniques Applied to an Indoor Micro Quadrotor. *International Conference on Robotics and Automation*.

Das, A., Fierro, R., Kumar, V., Ostrowski, J., Spletzer, J., & Taylor, C. (2002). A vision-based formation control framework. *IEEE Transactions on Robotics and Automation*, 18, 813-825.

Ju, C., & Son, H. (2018). Multiple UAV Systems for Agricultural Applications: Control, Implementation and Evaluation. *Electronics*, 7.

Khalil, H. (2014). *Nonlinear Systems*. Pearson.

Leonard, N., & Fiorelli, E. (2001). Virtual leaders, artificial potentials and coordinated control of groups. *Proceedings of the 40th IEEE Conference on Decision and Control*, 3, pp. 2968-2973.

Pounds, P., Mahony, R., & Corke, P. (2010). Modelling and control of a large quadrotor robot. *Control Engineering Practice*, 18, 691-699.

Rosalie, M., Dentler, J., Danoy, G., Bouvry, P., Kannan, S., Mendez, M., & Voos, H. (2017). Area exploration with a swarm of UAVs combining deterministic chaotic ant colony mobility with position MPC. *International Conference on Unmanned Aircraft Systems*, (pp. 1392-1397).

Scherer, J., & Rinner, B. (2020). Multi-UAV Surveillance With Minimum Information Idleness and Latency Constraints. *IEEE Robotics and Automation Letters*, 4812-4819.

Shao, J., Xie, G., & Wang, L. (2007). Leader-following formation control of multiple mobile vehicles. *IET Control Theory and Applications*, 1, 545-552.

International Journal of Aviation Science and Technology

Research Article

Frequency Domain Analysis of F-16 Aircraft in a Variety of Flight Conditions

Abdurrahim Bilal Özcan[1]*, Elbrus Caferov[2]

[1] İstanbul Technical University, İstanbul, Turkiye
ozcana20@itu.edu.tr - 0000-0003-4994-7572

[2] İstanbul Technical University, İstanbul/Turkiye
cafer@itu.edu.tr - 0000-0002-7742-2514

Abstract

Examining the flight quality of an aircraft to ensure the stability of the aircraft, increase maneuverability, and make the aircraft easier to control by the pilot necessitates an examination of the natural stability of the system. Within the scope of the paper, the frequency domain response of the F-16 aircraft dynamics is analyzed using Simulink models considering two different flight regimes because the frequency-domain methods have many distinct and important advantages over time-domain methods. Aerodynamic, propulsive, and atmospheric databases are used to create the nonlinear model. The trim analysis for cruise flights is carried out to obtain trim parameters. The aircraft is numerically linearized using the small perturbation theory. The linearized dynamics for each trim condition are used to create transfer functions for each input. The linear model is subsequently examined in the frequency domain to obtain information about the dynamic behavior of the aircraft, and flight quality analysis was examined by considering the lateral and longitudinal modes of the aircraft by international standards. It has been clearly understood the stability augmentation system design has critical importance for the modes with unstable or long steady-state duration.

Keywords

Frequency Domain Analysis
F-16 Aircraft
Lateral Motion
Longitudinal Motion
System Dynamics

Time Scale of Article

Received 06 February 2022
Revised until 08 April 2022
Accepted 23 April 2022
Online date 28 June 2022

1. Introduction

Stability analysis is a critical phenomenon that needs to be addressed for achieving the targeted mission according to the aircraft type. Passenger comfort, the pilot's ability to control the aircraft, the calculation of flight performance, how accurately the sensors will work, and many other criteria (Hess, 2007) can be revealed by analyzing the natural stability of the aircraft. Especially with the developing technology, enhancing technical capacities and travel time maneuverability, and increasing time-varying data such as ammunition and fuel necessitates performance and efficiency calculations and high-accuracy tests (Dündar et al., 2020). These tests are carried out using the aerodynamic efficiency data arising from the design of the aircraft, the equations of motion calculated from the aerodynamic coefficients and the effectiveness of the control surfaces, flight performance calculations, etc.

Frequency domain analysis is useful for dynamic analysis, robust controller design (Hess, 2007) and verification, guidance and trajectory studies, air combat research, and many other missions (Garza and Morelli, 2003). It indicates how well the aircraft responds to a range of input frequencies. Changes in amplitude and phase fit into a specific pattern that depends on the aircraft's design, from which information about the system is revealed. Also, the higher bandwidth means the faster-commanded speed or position adjustment time (Wescott, 2006). The bode is an analysis plot for a linear

*: Corresponding Author Abdurrahim Bilal Özcan, ozcana20@itu.edu.tr
DOI: 10.23890/IJAST.vm03is01.0103

time-invariant system in the frequency domain that includes a magnitude and a phase plot (Atangana and Akgül, 2020).

Morelli et al. mentioned that (Morelli and Grauer, 2020; Morelli and Jared, 2015) frequency-domain studies for F-16 fighter aircraft have crucial advantages over time-domain studies due to the reasons such as noise rejection, accurate modeling, the modeling of parametric uncertainty, enabling simple and effective approach, data extraction, and validation, real-time modeling, flying qualities modeling, and computational efficiency. Along with these advantages, a disadvantage of frequency-domain estimation is associated with the practical limitation of identification techniques to linear dynamical systems only (Klein, 1978 and 1980). Fu stated (Fu, 1990) that the frequency response of the transfer function facilitates the enhancement of uncertain transfer matrices for multi-input, multi-output systems (MIMO). Meanwhile, these results are utilized to determine the H∞ norm, gain margin, and phase margin and to improve the diagonal dominance of the MIMO indeterminate system. A frequency-domain study is also used to determine the stability parameters of the aircraft (Morelli, 2000, Millidere, 2021, Shukla et al., 2017). The short-period characteristic evaluated in the longitudinal motion was obtained by driving the elevator input at different frequencies. With some estimated aerodynamic derivatives of the system, the second order transfer function and accordingly the damping ratio and natural frequency data can be obtained (Milliken, 1947, Greenberg, 1951).

In this paper, the frequency domain response of the F-16 fighter airplane dynamics is analyzed with performed Simulink models considering altitude of 3000 feet (914.4 m) and 30000 feet (9144 m) trimming conditions. To acquire comprehensive nonlinear dynamics, the plant model of the F-16 fighter airplane is established by modeling aerodynamic, gyroscopic, gravitational, and propulsive force and moments concerning atmospheric effects. The modeling part comprises various data such as the geometric configuration of fighter airplanes, aircraft wind tunnel test aerodynamic and propulsion data, given inertia-mass parameters, and engine angular momentum.

In kinematic calculations, Euler angular representation is chosen to obtain transfer functions and state-space representations to make the final results understandable. The most important advantage of quaternion is that it eliminates the singularity problem. However, it is more difficult to interpret quaternion than Euler angles. Since there is no singularity at the points where linearization is made, it does not affect the analysis made in the frequency domain, and in order to make the final results understandable, both transfer functions and state-space representations are made according to Euler angles.

The aircraft operation intervals, which also define where the trim conditions are, should be specified prior to linearization. The intervals can be defined for take-off, cruise, or another mode. The states and required control inputs can then be derived by trim analysis of these operating points. Once the trim variables are obtained, the nonlinear dynamics of the aircraft can be linearized to obtain the state-space equations. In this paper, reappraisal is carried out in this study by looking at the dynamics in the frequency domain. In the end, the aircraft dynamics are also investigated purpose whether they are appropriate for human and aircraft dynamic response interfaces, as successful maneuvering, approaching, and tracking missions are all dependent on them. As a result, for the given criteria, this analysis should also be carried out in terms of the damping ratio, time constant, and natural frequency of lateral and longitudinal modes.

This paper is organized as follows. The nonlinear equation of the system dynamics is addressed in the second chapter. Then, the trim conditions for cruise flight and linearization process of the nonlinear model are expressed to obtain transfer functions and break frequencies which constitutive they are tabulated. Also, the state-space model of the F-16 aircraft is composed. In the third chapter, Bode diagrams and pole maps are demonstrated. Finally, obtained results and their effects on stability modes are analyzed and interpreted.

2. Equation of Motion

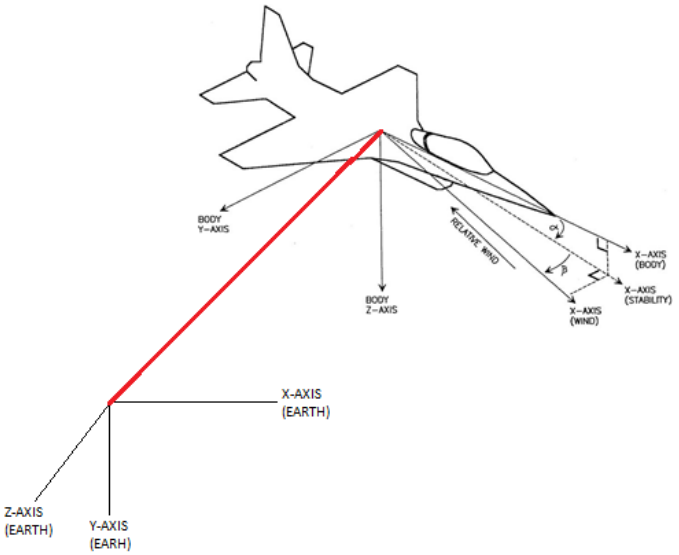

Fig. 1. Earth-fixed and body-fixed reference frames (Stevens and Lewis, 1992)

Considering the equation of motion of an aircraft, various assumptions are made in order to simplify the equations. First, the airframe is assumed to be a rigid body, so the center of gravity of the aircraft won't have a

relative velocity for the Body-fixed reference frame. Second, the mass of aircraft is assumed to be constant, and finally, mass distribution remains constant during the flight, resulting in a constant inertia tensor. The equation of motion of an aircraft is mainly obtained on Earth-fixed and Body-fixed reference frames. These reference frames are represented in Fig. 1.

Six nonlinear equations of motion were utilized to model nonlinear aircraft dynamics for translational and rotational motion (Stevens and Lewis, 1992). These equations are shown in (1-4).

$$\dot{u} = \frac{\sum F_x}{m} - qw + rv \tag{1}$$

$$\dot{v} = \frac{\sum F_y}{m} - ur + pw \tag{2}$$

$$\dot{w} = \frac{\sum F_z}{m} - pv + qu \tag{3}$$

External forces acting on the aircraft in a body-fixed reference frame, such as aerodynamic, gravitational, and propulsive forces, are represented by F_x, F_y, and F_z. Sometimes, these equations are used by transforming them into earth-fixed or wind axes reference frames. For the earth-fixed frame, transformation can be done by using the relation below.

$$\begin{pmatrix} \dot{x} \\ \dot{y} \\ \dot{z} \end{pmatrix} = \begin{pmatrix} cos\psi cos\theta & cos\psi sin\theta sin\phi - sin\psi cos\phi & cos\psi sin\theta cos\phi + sin\psi sin\phi \\ sin\psi cos\theta & sin\psi sin\theta sin\phi + cos\psi cos\phi & sin\psi sin\theta cos\phi - sin\psi sin\phi \\ -sin\theta & cos\theta sin\phi & cos\theta cos\phi \end{pmatrix} \begin{pmatrix} u \\ v \\ w \end{pmatrix} \tag{4}$$

Where ϕ, θ, and ψ are the Euler angles that correspond to orientation in the earth-fixed frame and the transformation matrix T_E^B, provides a transformation from body-fixed frame to earth-fixed frame. The other transformation to wind axes can be done using the (5).

$$\begin{pmatrix} \dot{V}_T \\ \dot{\beta} \\ \dot{\alpha} \end{pmatrix} = \begin{pmatrix} \cos\alpha\cos\beta & \sin\beta & \sin\alpha\cos\beta \\ -\frac{1}{V_T}\cos\alpha\sin\beta & \frac{1}{V_T}\cos\beta & -\frac{1}{V_T}\sin\alpha\sin\beta \\ -\frac{\sin\alpha}{V_T\cos\beta} & 0 & \frac{\cos\alpha}{V_T\cos\beta} \end{pmatrix} \begin{pmatrix} u \\ v \\ w \end{pmatrix} \tag{5}$$

On the other hand, rotational equation of motion can be found using Newton's second law,

$$\sum M_{ext} = \frac{dH}{dt} = \dot{H} + \omega \times H \tag{6}$$

Hence, angular velocity rates can be found as

$$\dot{p} = \frac{\sum L + I_{xy}(\dot{q} - pr) + I_{xz}(\dot{r} + pq) - (I_{zz} - I_{yy})qr - I_{yz}(r^2 - q^2)}{I_{xx}} \tag{7}$$

$$\dot{q} = \frac{\sum M + I_{yz}(\dot{r} - pq) + I_{xy}(\dot{p} + qr) - (I_{xx} - I_{zz})pr - I_{xz}(p^2 - r^2)}{I_{yy}} \tag{8}$$

$$\dot{r} = \frac{\sum N + I_{xz}(\dot{p} - qr) + I_{yz}(\dot{q} + pr) - (I_{yy} - I_{xx})pq - I_{xy}(q^2 - p^2)}{I_{zz}} \tag{9}$$

In general applications, regarding aircraft geometry, some product inertia terms that are I_{xy} and I_{yz} may be neglected. Another transformation can be performed for rotational kinematics, which incorporates angular body rates and Euler angle rates,

$$\begin{pmatrix} \dot{\phi} \\ \dot{\theta} \\ \dot{\psi} \end{pmatrix} = \begin{pmatrix} 1 & \tan\theta\sin\phi & \cos\phi\tan\theta \\ 0 & \cos\phi & -\sin\phi \\ 0 & \sec\theta\sin\phi & \sec\theta\cos\phi \end{pmatrix} \begin{pmatrix} p \\ q \\ r \end{pmatrix} \tag{10}$$

3. Modeling

During the flight, some external forces and moments are acting on the aircraft. There are variety of factors that cause these forces and moments. These variables and model types will be discussed in this section. Aerodynamic, propulsion, atmospheric, gyroscopic, and gravitational models are all covered in this article.

For aerodynamic modeling, Nguyen et al. (1979) provided extensive data about the fighter aircraft F-16, and the data that is used in this paper is obtained from that article by Nguyen (1979). This data consists of two main parts, which are breakpoints and data. The data part is based on the data which is obtained from wind-tunnel testing of F-16 (Nguyen, 1979). On the other hand, breakpoints store the angle of attack, slip angle, or surface deflection data in which wind-tunnel testing is conducted.

$$F_{(X,Y,Z)_{aerodynamic}} = C_{x,y,z} \times \bar{q} \times S \tag{11}$$

$$M_{(L,M,N)_{aerodynamic}} = C_{l,m,n} \times \bar{q} \times S \times b \tag{12}$$

Where the dynamic pressure is $\bar{q}$, the wing reference area is S, the span length is b, and the aerodynamic chord length is C.

For propulsion modeling, In F-16 aircraft, propulsion is provided by a turbofan jet engine. The engine data is given in reference to Nguyen (1979) for F-16 aircraft, and it is used to calculate thrust force F_T. Regarding provided data, thrust force depends on Mach number, altitude of the aircraft, and throttle settings of idle, mil, and max. Thrust value is calculated by interpolating provided data with input variables. An interpolation must be done considering power percentage to find thrust value within these points. If the throttle level is within the 50-0 percent,

$$T = T_{idle} + (T_{mil} - T_{idle})(\frac{ts}{0.77}) \tag{13}$$

where ts is the percent throttle setting within 0-1, and if the throttle level is within 50-100, thrust becomes,

$$T = T_{mil} + (T_{max} - T_{mil})(ts - 0.77)/0.77 \tag{14}$$

propulsive forces can be defined as,

$$F_P = \begin{pmatrix} F_T cos\theta_p cos\psi_p \\ F_T cos\theta_p sin\psi_p \\ -F_T sin\theta_p \end{pmatrix} \tag{15}$$

the moment can be calculated using relation below,

$$M_P = \begin{pmatrix} -(F_T \cos\theta_p \sin\psi_p) r_{P,z} - (F_T \sin\theta_p) r_{P,y} \\ (F_T \cos\theta_p \cos\psi_p) r_{P,z} + (F_T \sin\theta_p) r_{P,x} \\ -(F_T \cos\theta_p \cos\psi_p) r_{P,y} + (F_T \sin\theta_p \sin\psi_p) r_{P,x} \end{pmatrix} \quad (16)$$

ψ_p represents the angle between the z-axis of reference frames and θ_p represents the angle between the y-axis of propulsion and body reference frame. $\boldsymbol{r}_{P/cg}$ are assumed to be zero, which makes the propulsive force vector $\boldsymbol{F}_P$ has an only component in the x-axis of the body frame.

Rotating rigid bodies have angular momentum. Suppose that an external moment acts on the rigid body that generates angular velocity. In that case, gyroscopic moments are generated to conserve previous angular momentum by producing the counter moment called the gyroscopic precession effect. According to the reference Nguyen (1979), the angular momentum of the aircraft is considered as 216.9 kg.m^2/sec in the x-direction of the propulsion system reference frame. Therefore, in this system, gyroscopic moments can be found as,

$$\sum M_{Gy} = -\begin{pmatrix} 0 \\ r H_{P,x} j_B \\ -q H_{P,x} k_B \end{pmatrix} \quad (17)$$

Due to gravitation, there is always applied gravitation force on aircraft. As the attitude of the aircraft changes, the gravitational vector in the body axis changes. This can be modeled by using the earth-to-body reference frame transformation matrix T_E^B and gravity vector in the earth-fixed reference frame. Force components can be found as

$$F_G = \begin{pmatrix} -mg \sin\theta \\ mg \cos\theta \sin\phi \\ mg \cos\theta \cos\phi \end{pmatrix} \quad (18)$$

For actuator modeling, some time lag can be observed when a command was given to an actuator. As a result, these actuator dynamics are also incorporated into the simulation system to make it more realistic. The actuator models are considered first order system. Rate and position limiters are also added to the model. Additionally, the references of actuator models can be given as Nguyen, 1979 and Sonneveldt 2006.

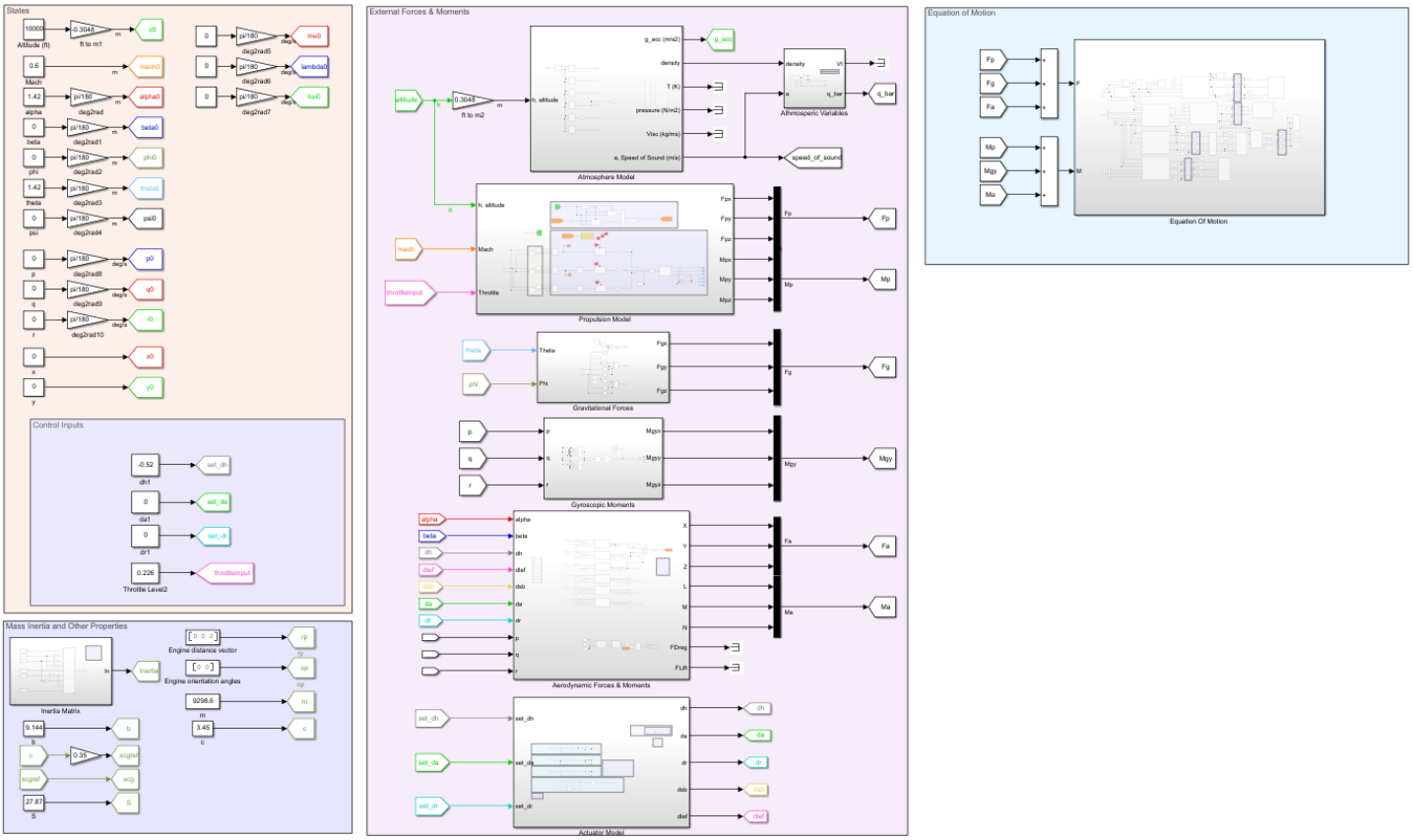

Fig. 2. General Simulink model of the F-16 aircraft before trimming phase

4. Trim Conditions and Linearization

Linearization of equations of motion and decomposition of linearized equations into two sets, longitudinal and lateral, are studied in this section. The operational points that determine the numerical outcome of the trim conditions must be determined before linearization. Trim conditions will be found by finding the point where the forces and moments acting on aircraft body are zero using the optimization algorithm. The cost function to be minimized is specified in (19). The constraint equations that will set the limits of optimization are translational dynamics, rotational dynamics,

translational kinematics, rotational kinematic, and some additional physical definitions for specific of the trim conditions. Translational dynamics are introduced in (1-3), translational kinematics are introduced in (4), rotational dynamics are introduced in (7-9), and rotational kinematics are introduced in (10).

$$J = f_{TD1}^2 + f_{TD2}^2 + f_{TD3}^2 + f_{RD1}^2 + f_{RD2}^2 + f_{RD3}^2 + f_{RK1}^2 + f_{RK2}^2 + f_{RK3}^2 + f_{TK2}^2 + f_{TK3}^2 \quad (19)$$

States are V_T, β, α, (u, v, w), p, q, r, φ, θ, ψ, h, γ and control Inputs are δ_e, δ_a, δ_r, δ_T. Four states are defined in question V_T (velocity), h (altitude), γ (gamma angle), and φ angle. The trim is mostly searched for the defined condition. $\zeta_{specified}$ = [V_T, h, γ, φ]^T, V_T = constant, h = constant, γ = constant, φ = 0, $\zeta_{unknown}$=[β, α, p, q, r, θ, ψ, δ_e, δ_a, δ_r, δ_T]^T. Thus, the cost function J($\zeta_{specified}$, $\zeta_{unknown}$) for the general straight flight can be solved with 11 unknowns for 11 equations. The constraint equations are translational dynamics, rotational dynamics, translational kinematics, rotational kinematic, and some additional physical definitions for specific trim conditions. Simulation of F-16 fighter aircraft is performed regarding these trim analyses. The states and control inputs are initialized considering findings in trim analysis, and the dynamics of the aircraft are analyzed.

Optimization algorithms make minimization according to the targeted subject. According to the selected optimization algorithm, local minimum or global minimum can be found. The cost function is primarily used to evaluate the current performance of the model by comparing the predicted results. For the J cost function to be equal to zero, all the functions that make it up must be zero. While the selected optimization algorithm solves this, it tries to bring the cost function closer to zero. Scatter-Search-Based global optimization was used in MATLAB Global Search Method to find trimmed states and inputs. A Global Search object presents a solver that attempts to locate the solution with the lowest objective function value. Global Search solver first generates trial points employing a Scatter Search method. These trial points are then filtered and fmincon is started from each of the filtered points. For case 1, the fmincon function converges to 1.535628e-11; furthermore, the Global Search algorithm converges to 5.6463e-14, corresponding to the least minimum value. For case 2, fmincon function converges to 0.00602 where corresponds to the local minimum. Since the value found with fmincon is not the global minimum, a different algorithm has been tried. The minimum cost function 3.5680e-13 was found via the Global Search algorithm. The selected algorithm cannot converge any further. While searching the global minimum, the following constraints and initial values were referred.

Table 2. Trimmed state derivatives ($\dot{x}$) of Case 1

$\dot{V}_{T1}$	$\dot{\alpha}_1$	$\dot{q}_1$	$\dot{\theta}_1$	$\dot{\beta}_1$	$\dot{p}_1$	$\dot{r}_1$	$\dot{\phi}_1$
0	0	0	0	0	0	0	0

Table 4. Trimmed Inputs (u) for Case 1

δ_{T1} [% ratio]	δ_{ht1} [deg]	δ_{a1} [deg]	δ_{r1} [deg]
0.1485	-0.5708	0	0

Table 5. Trimmed state derivatives ($\dot{x}$) of Case 2

$\dot{V}_{T2}$	$\dot{\alpha}_2$	$\dot{q}_2$	$\dot{\theta}_2$	$\dot{\beta}_2$	$\dot{p}_2$	$\dot{r}_2$	$\dot{\phi}_2$
0	0	0	0	0	0	0	0

Table 7. Trimmed Inputs (u) for Case 2

δ_{T1} [% ratio]	δ_{ht1} [deg]	δ_{a1} [deg]	δ_{r1} [deg]
0.4221	-0.5134	0	0

The six nonlinear differential equations that govern aircraft motion are nonlinear differential equations. That can be solved with a variety of numerical integration techniques. However, it is practically difficult to obtain closed solutions (equations for each variable). Closed solutions to the dynamic behavior of the aircraft can provide helpful information (linear models). Hence, alternative strategies such as obtaining partial derivatives of the equation of motion or small perturbation approaches (Jafarov and Tasaltm, 1999) are used to linearize the aircraft's equations of motion. By applying the conditions in Table 2 and Table 3, the

Table 1. Constraints and initial values of Case-1 and Case-2

	β [rad]	α [rad]	p [rad/s]	q [rad/s]	r [rad/s]	θ [rad]	ψ [rad]	δ_{ht} [°]	δ_a [°]	δ_r [°]	δ_T [%]
Case 1: M=0.45, h=3000 ft (914.4 m), γ=0°, ϕ =0°											
Initial	0.0017	0.0175	1	1	1	pi/12	pi/9	0.1	0.1	0.1	0.8
Lower	-pi/6	-pi/2	-inf	-inf	-inf	-pi/2	-pi	-25	-21.5	-30	0
Upper	pi/6	pi/2	inf	inf	inf	pi/2	pi	25	21.5	30	1
Case 2: M=0.45, h=30000 ft (9144 m), γ =0°, ϕ =0°											
Initial	0.0017	-0.0175	-0.1	-0.1	-0.1	-pi/12	-pi/9	-0.1	0.1	0.1	0.3
Lower	-pi/6	-pi/2	-1	-1	-1	-pi/2	-pi	-25	-21.5	-30	0
Upper	pi/6	pi/2	1	1	1	pi/2	pi	25	21.5	30	1

Table 3. Trimmed States (x) of Case 1

V_{T1} [m/s]	α_1[rad - deg]		q_1 [rad/s]	θ_1 [rad - deg]		β_1 [rad]	p_1 [rad/s]	r_1 [rad/s]	ϕ_1 [rad]
151.5302	0.0446	2.5581	0	0.0446	2.5581	0	0	0	0

Table 6. Trimmed States (x) of Case 2

V_{T2} [m/s]	α_2[rad - deg]		q_2 [rad/s]	θ_2 [rad - deg]		β_2 [rad]	p_2 [rad/s]	r_2 [rad/s]	ϕ_2 [rad]
136.4314	0.1728	9.8989	0	0.1728	9.8989	0	0	0	0

Linear state-space model of longitudinal dynamics for case 1 in (20)

$$\begin{bmatrix}\Delta\dot{V}_T\\ \Delta\dot{\alpha}\\ \Delta\dot{q}\\ \Delta\dot{\theta}\end{bmatrix}=\begin{bmatrix}-0.0182 & 1.1250 & -0.2336 & -9.8043\\ -0.0009 & -0.9145 & 0.9118 & 0\\ 0.0004 & 0.6531 & -0.9798 & 0\\ 0 & 0 & 1 & 0\end{bmatrix}\begin{bmatrix}\Delta V_T\\ \Delta\alpha\\ \Delta q\\ \Delta\theta\end{bmatrix}+\begin{bmatrix}7.3609 & 0.0306\\ -0.0022 & -0.0022\\ 0 & -0.1663\\ 0 & 0\end{bmatrix}\begin{bmatrix}\Delta\delta_{T1}\\ \Delta\delta_{ht1}\end{bmatrix} \quad (20)$$

Linear state-space model of lateral dynamics for case 1 in (21).

$$\begin{bmatrix}\Delta\dot{\beta}\\ \Delta\dot{p}\\ \Delta\dot{r}\\ \Delta\dot{\varphi}\end{bmatrix}=\begin{bmatrix}-0.2730 & 0.0444 & -0.9919 & 0.0646\\ -27.4910 & -3.2705 & 0.6278 & 0\\ 6.4680 & -0.0318 & -0.4349 & 0\\ 0 & 1 & 0 & 0\end{bmatrix}\begin{bmatrix}\Delta\beta\\ \Delta p\\ \Delta r\\ \Delta\varphi\end{bmatrix}+\begin{bmatrix}0.0003 & 0.0007\\ -0.6636 & 0.1148\\ -0.0279 & -0.0560\\ 0 & 0\end{bmatrix}\begin{bmatrix}\Delta\delta_{a1}\\ \Delta\delta_{r1}\end{bmatrix} \quad (21)$$

Linear state-space model of longitudinal dynamics for case 2 in (22).

$$\begin{bmatrix}\Delta\dot{V}_T\\ \Delta\dot{\alpha}\\ \Delta\dot{q}\\ \Delta\dot{\theta}\end{bmatrix}=\begin{bmatrix}-0.0189 & -2.2246 & -0.5453 & -9.7786\\ -0.0010 & -0.3908 & 0.9630 & 0\\ 0.0002 & -0.1414 & -0.4208 & 0\\ 0 & 0 & 1 & 0\end{bmatrix}\begin{bmatrix}\Delta V_T\\ \Delta\alpha\\ \Delta q\\ \Delta\theta\end{bmatrix}+\begin{bmatrix}2.2820 & -0.0105\\ -0.0029 & -0.0009\\ 0 & -0.0540\\ 0 & 0\end{bmatrix}\begin{bmatrix}\Delta\delta_{T2}\\ \Delta\delta_{ht2}\end{bmatrix} \quad (22)$$

Linear state-space model of lateral dynamics for case 2 in (23).

$$\begin{bmatrix}\Delta\dot{\beta}\\ \Delta\dot{p}\\ \Delta\dot{r}\\ \Delta\dot{\varphi}\end{bmatrix}=\begin{bmatrix}-0.0996 & 0.1727 & -0.9821 & 0.0706\\ -13.0351 & -1.0935 & 0.5716 & 0\\ 2.1056 & -0.0224 & -0.1499 & 0\\ 0 & 1 & 0 & 0\end{bmatrix}\begin{bmatrix}\Delta\beta\\ \Delta p\\ \Delta r\\ \Delta\varphi\end{bmatrix}+\begin{bmatrix}0.0001 & 0.0003\\ -0.2011 & 0.0364\\ -0.0079 & -0.0183\\ 0 & 0\end{bmatrix}\begin{bmatrix}\Delta\delta_{a2}\\ \Delta\delta_{r2}\end{bmatrix} \quad (23)$$

Table 8. Transfer functions of trimmed points

	Case 1: M=0.45, *h*=3000 ft (914.4 m), γ =0°, ϕ =0°	**Case 2**: M=0.45, *h*=30000 ft (9144 m), γ =0°, ϕ =0°
$\frac{V_T(s)}{\delta_{ht}(s)}$	$\frac{0.030595\,(s+1.047)\,(s^2+2.037s+46.98)}{(s+1.721)\,(s-0.05708)\,(s^2+0.2486s+0.02056)}$	$\frac{-0.01047\,(s-9.21)\,(s+6.689)\,(s+0.3182)}{(s^2+0.004027s+0.006845)\,(s^2+0.8265s+0.3036)}$
$\frac{\alpha(s)}{\delta_{ht}(s)}$	$\frac{-0.002168\,(s+70.94)\,(s^2+0.01839s+0.009173)}{(s+1.721)\,(s-0.05708)\,(s^2+0.2486s+0.02056)}$	$\frac{-0.00094077\,(s+55.73)\,(s^2+0.01924s+0.0104)}{(s^2+0.004027s+0.006845)\,(s^2+0.8265s+0.3036)}$
$\frac{q(s)}{\delta_{ht}(s)}$	$\frac{-0.16632\,s\,(s+0.01933)\,(s+0.9218)}{(s+1.721)\,(s-0.05708)\,(s^2+0.2486s+0.02056)}$	$\frac{-0.054045\,s\,(s+0.01289)\,(s+0.3944)}{(s^2+0.004027s+0.006845)\,(s^2+0.8265s+0.3036)}$
$\frac{\theta(s)}{\delta_{ht}(s)}$	$\frac{-0.16632\,(s+0.01933)\,(s+0.9218)}{(s+1.721)\,(s-0.05708)\,(s^2+0.2486s+0.02056)}$	$\frac{-0.054045\,(s+0.01289)\,(s+0.3944)}{(s^2+0.004027s+0.006845)\,(s^2+0.8265s+0.3036)}$
$\frac{\beta(s)}{\delta_a(s)}$	$\frac{0.00025585\,(s-1.578)\,(s^2-1.79s+49.52)}{(s+3.193)\,(s+0.01849)\,(s^2+0.767s+7.569)}$	$\frac{9.4388e-05\,(s-284.9)\,(s^2+0.6015s+0.093)}{(s+0.8485)\,(s+0.005894)\,(s^2+0.4885s+4.198)}$
$\frac{p(s)}{\delta_a(s)}$	$\frac{-0.66361\,(s-0.002859)\,(s^2+0.7477s+7.693)}{(s+3.193)\,(s+0.01849)\,(s^2+0.767s+7.569)}$	$\frac{-0.20115\,(s-0.01245)\,(s^2+0.2906s+2.594)}{(s+0.8485)\,(s+0.005894)\,(s^2+0.4885s+4.198)}$
$\frac{r(s)}{\delta_a(s)}$	$\frac{-0.02791\,(s+1.721)\,(s^2+1.007s+6.808)}{(s+3.193)\,(s+0.01849)\,(s^2+0.767s+7.569)}$	$\frac{-0.0079385\,(s+0.4108)\,(s^2+0.1908s+11.41)}{(s+0.8485)\,(s+0.005894)\,(s^2+0.4885s+4.198)}$
$\frac{\varphi(s)}{\delta_a(s)}$	$\frac{-0.66485\,(s^2+0.7486s+7.693)}{(s+3.193)\,(s+0.01849)\,(s^2+0.767s+7.569)}$	$\frac{-0.20253\,(s^2+0.2804s+2.652)}{(s+0.8485)\,(s+0.005894)\,(s^2+0.4885s+4.198)}$

$\frac{\boldsymbol{\beta(s)}}{\boldsymbol{\delta_r(s)}}$	$\frac{0.00071153\ (s+85.76)\ (s+3.181)\ (s+0.002136)}{(s+3.193)\ (s+0.01849)\ (s^2+0.767s+7.569)}$	$\frac{0.00025073\ (s+96.9)\ (s+0.9297)\ (s-0.0269)}{(s+0.8485)\ (s+0.005894)\ (s^2+0.4885s+4.198)}$
$\frac{\boldsymbol{p(s)}}{\boldsymbol{\delta_r(s)}}$	$\frac{0.11476\ (s+2.747)\ (s-2.513)\ (s-0.002903)}{(s+3.193)\ (s+0.01849)\ (s^2+0.767s+7.569)}$	$\frac{0.036392\ (s-2.149)\ (s+2.035)\ (s-0.01249)}{(s+0.8485)\ (s+0.005894)\ (s^2+0.4885s+4.198)}$
$\frac{\boldsymbol{r(s)}}{\boldsymbol{\delta_r(s)}}$	$\frac{-0.056005\ (s+3.223)\ (s^2+0.3034s+0.2855)}{(s+3.193)\ (s+0.01849)\ (s^2+0.767s+7.569)}$	$\frac{-0.018252\ (s+0.4992)\ (s^2+0.7096s+1.25)}{(s+0.8485)\ (s+0.005894)\ (s^2+0.4885s+4.198)}$
$\frac{\boldsymbol{\varphi(s)}}{\boldsymbol{\delta_r(s)}}$	$\frac{0.11226\ (s+2.742)\ (s-2.584)}{(s+3.193)\ (s+0.01849)\ (s^2+0.767s+7.569)}$	$\frac{0.033207\ (s+2.1)\ (s-2.355)}{(s+0.8485)\ (s+0.005894)\ (s^2+0.4885s+4.198)}$

Table 9. Break frequencies of transfer functions

		Break Frequencies
$\frac{\mathbf{V_T(s)}}{\mathbf{\delta_{ht}(s)}}$	Case-1	$K_{vt1}=0.030595, \frac{1}{T_{vt1}}=1.047, \omega_{n1}=6.854\ , \zeta_{n1}=0.148, \frac{1}{\tau 1_{ph1}}=0.05708, \frac{1}{\tau 1_{ph2}}=1.721, \omega_{n_{sp1}}=0.1433, \zeta_{sp1}=0.866$
	Case-2	$K_{vt2}=-0.01047, \frac{1}{T_{vt2}}=9.21, \omega_{n2}=1.458\ , \zeta_{n2}=2.4, \omega_{n_{phz}}=\ 0.0827, \zeta_{ph2}=0.0243, \omega_{n_{sp2}}=\ 0.55, \zeta_{sp2}=\ 0.75$
$\frac{\boldsymbol{\alpha(s)}}{\boldsymbol{\delta_{ht}(s)}}$	Case-1	$K_{a1}=-0.002168, \frac{1}{T_{a1}}=70.94, \omega_{n1}=0.0957\ , \zeta_{n1}=0.096, \frac{1}{\tau 1_{ph1}}=0.05708, \frac{1}{\tau 1_{ph2}}=1.721,\ \omega_{n_{sp1}}=\ 0.1433, \zeta_{sp1}=0.86$
	Case-2	$K_{a2}=-0.00094077, \frac{1}{T_{a2}}=55.73, \omega_{n2}=0.1019, \zeta_{n2}=0.094,\ \omega_{n_{phz}}=0.08273, \zeta_{ph2}=0.0243, \omega_{n_{sp2}}=0.55, \zeta_{sp2}=0.75$
$\frac{\boldsymbol{\theta(s)}}{\boldsymbol{\delta_{ht}(s)}}$	Case-1	$K_{\theta}=-0.002168,\ \ \frac{1}{T_{\theta_{i_1}}}=0.01933,\ \ \ \frac{1}{T_{\theta_{i_2}}}=0.9218, \frac{1}{\tau 1_{ph1}}=0.05708, \frac{1}{\tau 1_{ph2}}=1.721,\ \omega_{n_{sp1}}=\ 0.1433, \zeta_{sp1}=0.86$
	Case-2	$K_{\theta}=-0.054045, \frac{1}{T_{\theta_{z_1}}}=0.01289, \frac{1}{T_{\theta_{z_2}}}=0.3944, \omega_{n_{phz}}=\ 0.08273, \zeta_{\ ph2}=0.0243,\ \omega_{n_{sp2}}=\ 0.55, \zeta_{sp2}=0.75$
$\frac{\boldsymbol{\beta(s)}}{\boldsymbol{\delta_a(s)}}$	Case-1	$K_{\beta 1}=0.00025585,\ \ \frac{1}{\tau_{s1}}=3.193\ , \frac{1}{\tau_{r1}}=0.01849\ \ \ \omega_{ndr1}=\ 2.751\ \ \zeta_{ndr1}=0.139$
	Case-2	$K_{\beta 2}=9.4388e-05\ ,\ \ \frac{1}{\tau_{s2}}=0.8485\ , \frac{1}{\tau_{r2}}=0.005894\ \ \ \omega_{ndr2}=\ 2.048\ \ \zeta_{ndr2}=0.119$
$\frac{\boldsymbol{\varphi(s)}}{\boldsymbol{\delta_a(s)}}$	Case-1	$K_{\varphi 1}=-0.66485\ ,\ \omega_{n\varphi 1}=2.773,\ \zeta_{n\varphi 1}=0.1349\ \frac{1}{\tau_{r1}}=3.193\ , \frac{1}{\tau_{s1}}=0.01849,\ \omega_{ndr1}=\ 2.751\ \ \zeta_{ndr1}=0.139$
	Case-2	$K_{\varphi 2}=-0.20253\ ,\ \omega_{n\varphi 2}=1.628,\ \zeta_{n\varphi 2}=0.086\ \frac{1}{\tau_{r2}}=0.8485\ , \frac{1}{\tau_{s2}}=0.005894,\ \ \ \omega_{ndr2}=\ 2.048\ \ \zeta_{ndr2}=0.119$
$\frac{\mathbf{p(s)}}{\mathbf{\delta_r(s)}}$	Case-1	$K_{p1}=0.11476, \frac{1}{\tau 1_{\varphi 1}}=0.002903, \frac{1}{\tau 1_{\varphi 2}}=2.513, \frac{1}{\tau 1_{\varphi 3}}=2.747, \frac{1}{\tau_{r1}}=3.193, \frac{1}{\tau_{s1}}=0.01849, \omega_{ndr1}=2.751, \zeta_{ndr1}=0.139$
	Case-2	$K_{p2}=0.036392\ \frac{1}{\tau 2_{\varphi 1}}=0.01249 \frac{1}{\tau 2_{\varphi 2}}=2.035, \frac{1}{\tau 2_{\varphi 3}}=2.149, \frac{1}{\tau_{r2}}=0.8485\ , \frac{1}{\tau_{s2}}=0.005894, \omega_{ndr2}=2.048\ \zeta_{ndr2}=0.119$
$\frac{\mathbf{r(s)}}{\mathbf{\delta_r(s)}}$	Case-1	$K_{r1}=-0.056005, \frac{1}{T_{\psi 1}}=3.223, \omega_{n\psi 1}=0.534\ , \zeta_{\psi 1}=0.2839\ \frac{1}{\tau_{s1}}=3.193, \frac{1}{\tau_{r1}}=0.01849,\ \omega_{n_{dr1}}=\ 2.751, \zeta_{dr1}=\ 0.139$
	Case-2	$K_{r2}=-0.018252\ , \frac{1}{T_{\psi 2}}=0.4992, \omega_{n\psi 2}=1.118, \zeta_{\psi 2}=0.317, \frac{1}{\tau_{s2}}=0.8485, \frac{1}{\tau_{r2}}=0.005894,\ \omega_{ndr2}=2.048, \zeta_{ndr2}=0.119$

linearization process is completed, and these equations of motion are mathematically separated into two sets as longitudinal and lateral motion. After linearization, the equations of motion are divided into longitudinal motion, including variables Vt, α, q, θ, and lateral motion, including states β, ϕ, ψ, p, r. With thanks to the perturbed linearization algorithm, state-space models of Case-1 and Case-2 were generated with 2^{11} and 2^{10} precision, respectively. The relevant models can be expressed as follows.

The known flight conditions were chosen with respect to constant altitude and wings level as α= θ, β= -ψ, and angular position rates p = q = r = 0. Trimmed states and inputs are calculated in Table 2 and Table 3.

Frequency domain analysis is done using Bode diagram for single input single output systems. For this reason, longitudinal and latitudinal dynamics expressed in state-space form should be converted into transfer functions. Table 4 shows the F-16 aircraft's transfer functions. Table 5 also shows the break frequencies of transfer functions.

5. Frequency Domain and Flying Qualities Analysis

Transfer functions and root locus plots are provided for various modes. The outcomes of the open-loop study may be classified to represent various aspects of flight handling performance. Two flight conditions will be examined based on their behavior in different modes. Stability augmentation system and control augmentation system designs are required based on the data inspected from the frequency domain response.

The design is expected to meet the desired dynamics, and these dynamics are determined by both military and civil aviation standards. All these design and performance requirements are specified in MIL-F-8785C (Flying Qualities of Piloted Airplanes), which contains these military standards (MIL-F-8785C, 1980).

The criteria in the standards have varying constraints depending on the aircraft's class, flight phase, and flying quality. Therefore, it is necessary to determine the class of the F-16 fighter aircraft. F-16 aircraft can be classified as Class IV, Category A, or Level 1 according to MIL-F-8785C specifications. The limits that the aircraft dynamics are determined by looking at this classification (Atak, 2020). The damping ratio of the F-16 should be between $0.35 < \zeta_{sp} < 1.30$, and its natural frequency should be between $0.28 < \omega_{n_{sp}} < 3.6$. The damping ratio of the short-term mode should be as great as possible. If there is insufficient damping, serious problems may emerge. For the phugoid mode, the damping ratio $\zeta_{ph} \geq 0.04$ and $\log_e 2/(-\zeta\omega_{n_{ph}}) \geq 55$ requirements are specified in the MIL-F-8785C standards. The frequency domain and flight quality analyses are shown in the bode diagrams below for the two situations studied.

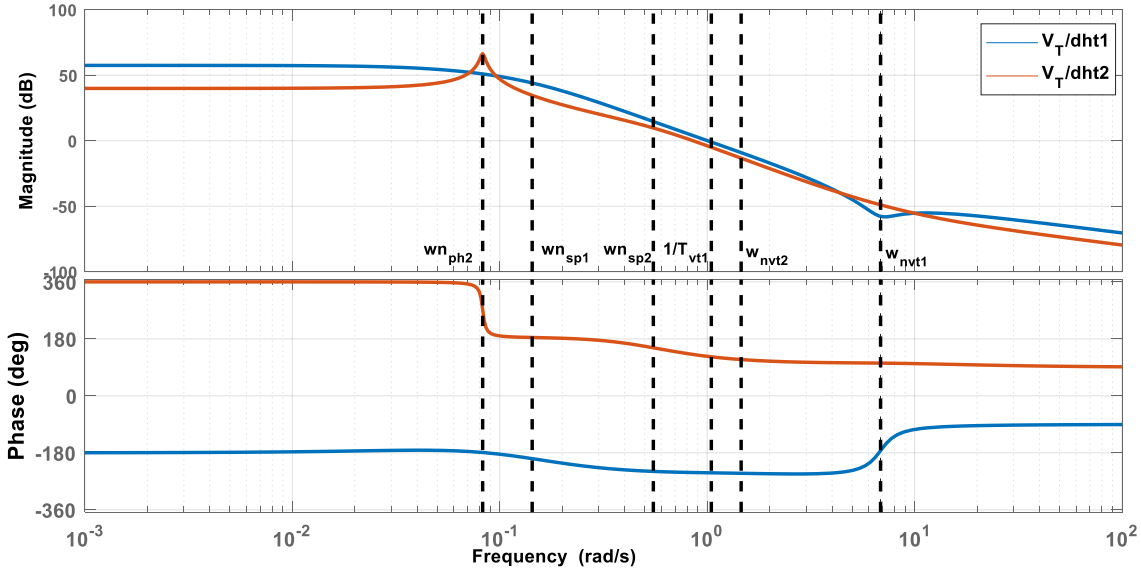

Fig.3. $\frac{V_T(s)}{\delta_{ht}(s)}$ Bode diagrams for Case-1 and Case-2.

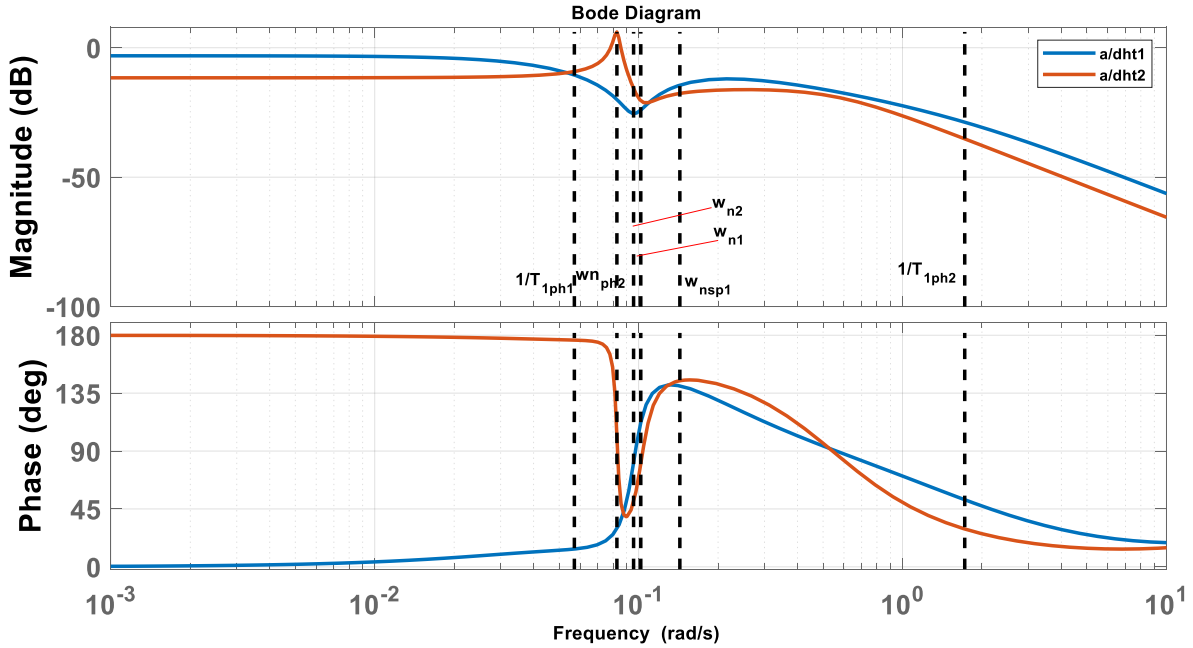

Fig. 4. $\frac{a(s)}{\delta_{ht}(s)}$ Bode diagrams for Case-1 and Case-2.

The frequency response of wind velocity V_T to horizontal tail input for case-1 and case-2 is shown. There is a pole for case-1 and zero for case-2 on the right side of the imaginary axis. Such systems are known as non-minimum phase systems. While the system in case-1 is unstable, the system in case-2 is stable. For both systems, at low frequencies, the gain margin value and phase shift remain constant. In case 2, a small peak in gain is observed when the input frequency crosses the short period break frequency, and the gain continues to decrease gradually at higher frequencies. At higher frequencies, the phase lag related to the short period mode results in a constant total phase lag of -180 degrees. The response steadily decreases as the control input frequency is raised, with an increasing phase lag. In particular, the dominant effect of Case-2 belongs to the phugoid mode, where the gain peaks because of the low damping ratio. It is explicitly located inside the observable bandwidth.

The frequency responses of the angle of attack a to horizontal tail input δ_{ht} for case-1 and case-2 are shown. The system in case-1 is unstable because of its positive pole. $\frac{1}{T_a}$ can not be seen because of the workspace of the figure. Because of the positive pole, case-1 is an unstable and nonminimum phase system, whereas case-2 is a stable and minimum phase system. The gain margin value is constant for both cases at extremely low frequencies. When the input frequency reaches the phugoid break frequency, the case-2 gain plot shows a peak that implies a small damping ratio, and the gain continues to decrease slowly at higher frequencies. There is significant phase lag induced by phugoid and phase lead caused by ω_{na} between the frequencies of 0.07 and 0.2. As the control input frequency is increased, the response diminishes steadily with increasing phase lag. In both cases, the system parameters are derived using the transfer function for pitch angle, where the input is a horizontal tail.

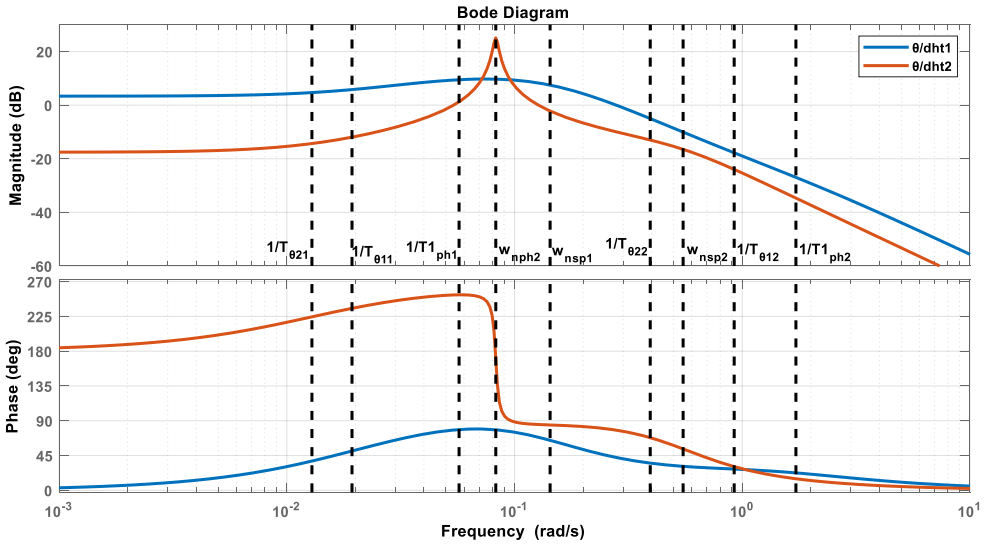

Fig. 5. $\frac{\theta(s)}{\delta_{ht}(s)}$ Bode diagrams for Case-1 and Case-2.

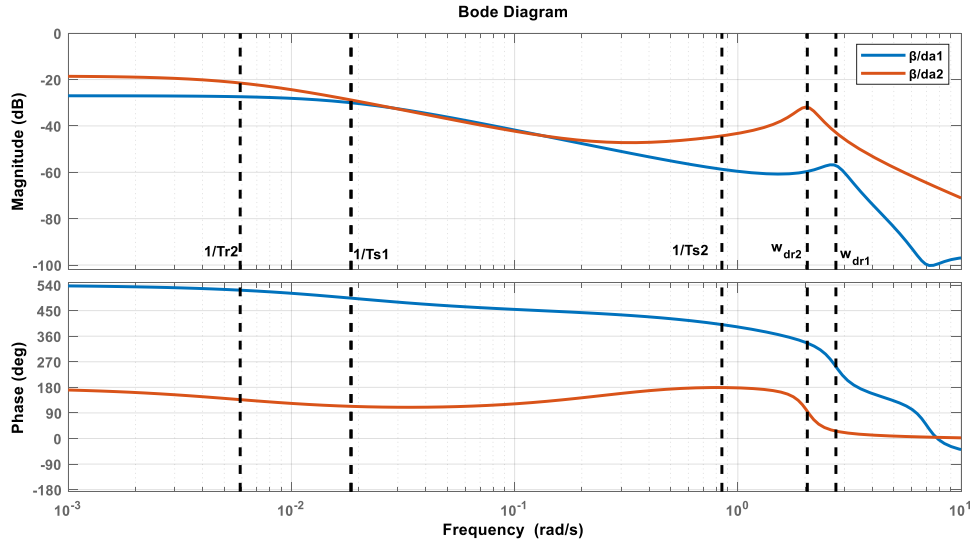

Fig. 6. $\frac{\beta(s)}{\delta_a(s)}$ Bode diagrams for Case-1 and Case-2.

The frequency response of side pitch angle θ, to horizontal tail input δ_{ht} for case-1 and case-2 are shown. For case-1, one pole is placed on the right side of the imaginary axis. Thus, this system is an unstable and nonminimum phase system. For case-2, there is not any zero or pole on the right side of the imaginary axis. Thus, this system is a stable and minimum phase system. The gain margin value remains constant at very low frequencies. As the control input frequency is increased, the attitude response decreases continuously with increasing phase lag after break frequency $\frac{1}{T_{\theta_1}}$ which caused a small peak on the gain margin. The case-1 results of these 3 transfer functions show that the longitudinal motion of the F 16 aircraft is unstable. But the longitudinal motion of the F 16 aircraft is stable for case-2.

The frequency response of sideslip angle β, to aileron input δ_a for case-1 and case-2 are shown. There is no pole on the right half side of the root locus diagram. But it has three positive zeros. Thus, this system is a nonminimum phase system. The right half plane zero has gained similar to that of the left half plane zero, but its phase nature is like a pole i.e., it adds adds negative phase to the system. Instead, the phase increases from 0 to 90 degrees, its phase increases from 0 to -90 degrees. This causes a delay in a system response which can lead to instability if not addressed. There is a peak at the dutch-roll frequency. But the gain is reduced by around −5 dB, which means that the pilot would see no significant oscillatory sideslip behavior. For case 2, there is no pole on the right half side of the root locus diagram. But it has three positive zeros. Thus, this system is a nonminimum phase system. Complex zeros at 0.30 rad/s frequency contribute approximately 15 dB into gain margin.

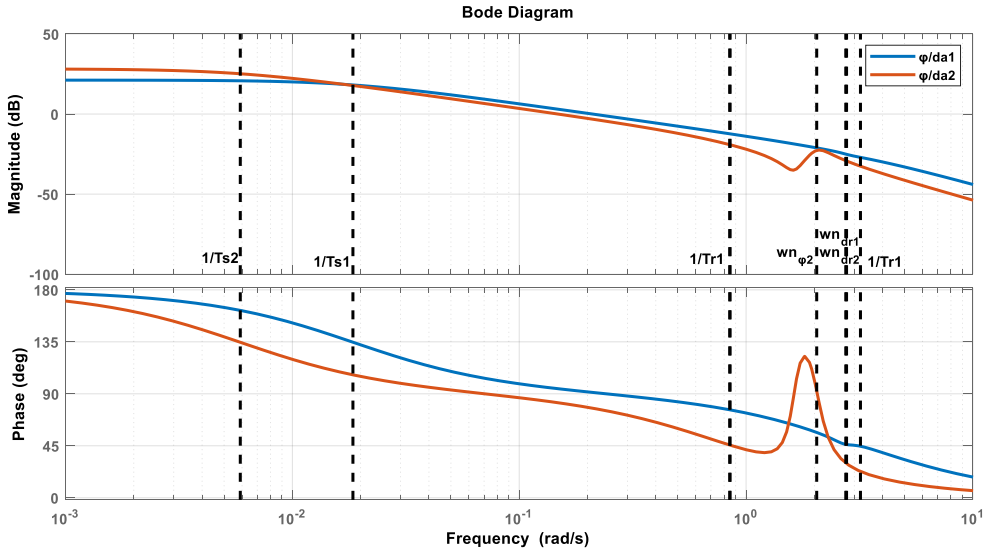

Fig. 7. $\frac{\varphi(s)}{\delta_a(s)}$ Bode diagrams for case-1 and case-2.

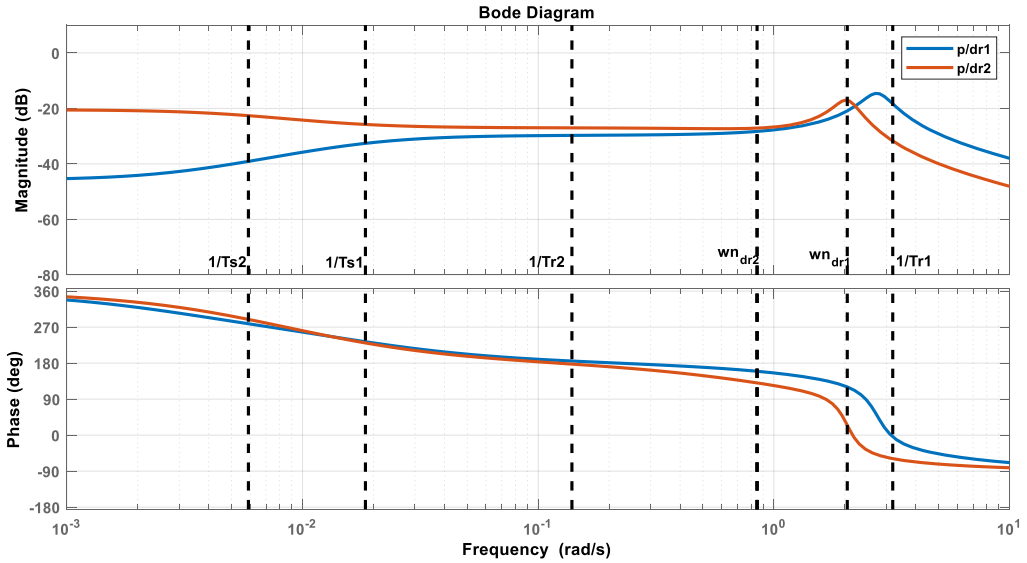

Fig. 8. $\frac{p(s)}{\delta_a(s)}$ Bode Diagrams for Case-1 and Case-2.

The frequency response of roll rate p, to rudder input δ_r for case-1 and case-2, are shown. Two systems are nonminimum phase systems because of positive zero values. Despite these zero values, systems are stable. The dutch-roll resonant peak in gain and subsequent roll-off in both gain and phase in case-1 are both standard and readily explained. If the effects at extremely low frequencies are neglected, it is not unrealistic to suggest that the usable bandwidth is a bit greater than the dutch-roll mode frequency. For case-2, increasing input frequency is affected obviously at dutch-roll break frequency. Dutch-roll frequency also adds around 10 dB to the system. In comparison between case-1 and case-2, case-1 has a less dominant spiral mode pole than case-2. As a result, the gain of case-1 ramps up till the spiral mode frequency, while the other's gain ramps down.

The frequency response of yaw rate r, to rudder input δ_r for case-1 and case-2 are shown. These 2 systems are minimum phase systems because there is not any positive value on the right side of the imaginary axis. In case 1, the phase lag increases in spiral mode dynamics at extremely low input frequencies until the effect of the second order numerator becomes apparent. The gain plot shows a steady but significant decrease with increasing frequency to reach a minimum of −50 dB at $\omega_{n\psi}$, the resonant frequency of the second order numerator factor. The gain rises rapidly with a further increase in frequency to reach a maximum of -25 dB at the dutch-roll frequency. For case-2, the gain plot shows a steady but significant decrease with increasing frequency to reach a minimum of −50 dB at $1/T_r$ roll mode break frequency. The gain rises rapidly with a further increase in frequency to reach a maximum of -31.2 dB at the dutch-roll frequency. C-1 and C-2 refer to Case-1 and Case-2 in Table 10.

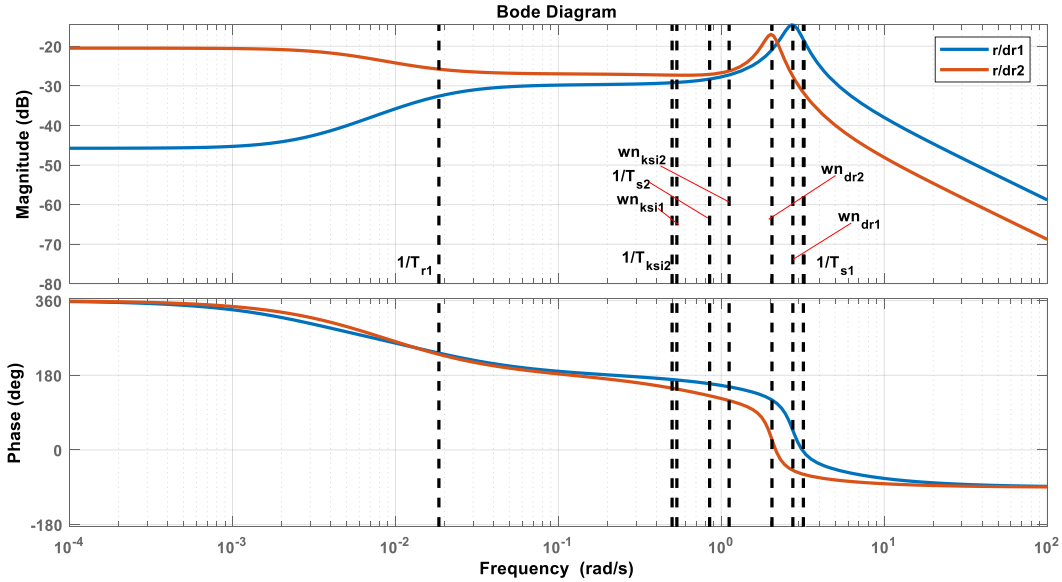

Fig. 9. $\frac{r(s)}{\delta_a(s)}$ Bode Diagrams for Case-1 and Case-2.

Table 10. All frequency domain values of longitudinal and lateral dynamics of F16 aircraft

	Longitudional Dynamics						**Lateral Dynamics**							
	$\frac{V_T(s)}{\delta_e(s)}$		$\frac{a(s)}{\delta_e(s)}$		$\frac{\theta(s)}{\delta_e(s)}$		$\frac{\beta(s)}{\delta_a(s)}$		$\frac{\phi(s)}{\delta_a(s)}$		$\frac{p(s)}{\delta_r(s)}$		$\frac{r(s)}{\delta_r(s)}$	
	Case-1	Case-2	Case-1	Case-2	Case-1	Case-2	Case-1	Case-2	Case-1	Case-2	Case-1	Case-2	Case-1	Case -2
Bandwidth (dB)	0.048	0.131	0.036	0.094	0.2729	0.7426	0.0184	0.0059	0.0184	0.0059	31.772	0.008	0.0184	0.006
Resonant Peak (dB)	57.44	66.41	-3.12	6.088	9.744	25.091	-26.99	-18.48	21.161	28.157	-14.58	-16.9	-18.77	-5.31
Resonant Freq. (rad/s)	0,001	0.083	1E-3	0.0827	0.0724	0.0827	1E-3	1E-4	1E-3	1E-4	2.6971	2.0195	1E-3	1E-4
Resonant Freq. (rad/s)	-50.5	-24.4	inf	11.6	inf	17.6	27	18.5	-21.2	-28.5	29.6	27	18.8	5.31
Phase Margin (deg)	-63	-49.3	inf	-16.6	-137	72.8	inf	inf	-88.8	-97.7	inf	inf	inf	inf

Mode analysis can be used to examine the aircraft's longitudinal and lateral transfer functions in addition to the frequency response of the systems. The derived transfer functions explain how the system responds to control input or disturbances, and the characteristic equation of transfer functions defines the characteristics of the system. These characteristic equations are fourth-order polynomial equations that each root corresponds to a different mode in aircraft analysis.

The transfer function poles correspond to phugoid or short period dynamic stability modes in longitudinal dynamics. The short term dynamic mode is a damped oscillation about y-axis on the body-fixed reference frame. The modes have a relatively high damping ratio and damped frequency compared to phugoid mode. Changes in velocity in the x-direction on a Body-fixed reference frame are not greatly affected since it is described as an oscillation in the y-axis. However, primary characteristics that are affected dominantly by the short-period mode are body angular rate in x direction, pitch angle and the velocity in the z-axis on body-fixed reference frame. The phugoid mode, on the other hand, may be represented as an oscillation in velocity u. The mode has a low damping ratio as well as a low damped frequency. So that, compared to the short-period mode, its poles are closer to the imaginary axis, and it has a slower response. Additionally, in this mode, velocity changes are coupled with pitch angle and altitude changes. Furthermore, with small fluctuations, the angle of attack tends to remain consistent. On the x-axis, the phugoid mode dominates the states, pitch angle, and velocity.

Roll mode, spiral mode, and dutch-roll mode are the three dynamic stability modes in lateral dynamics. Roll mode or subsidence roll can be defined as rolling dynamics around the x- axis in the body reference frame. The roll mode is a non-oscillatory mode that has a single pole in the real axis on a complex plane. It also affects the roll angle and roll rate. Another dynamic mode is spiral mode, also defined as non-oscillatory dynamics in lateral direction. When the sideslip angle disturbance excites the aircraft, the aircraft fin affects the roll angle, and dihedral effect influences the roll angle. It can be affected by disturbances on the sideslip angle. Therefore, regarding this, it can be stated that is a coupled motion (Bajodah at al., 2018) in yaw, sideslip, and roll. On longitudinal dynamics, the dutch-roll mode is identical to the short-period mode, but it occurs in the z-axis on the body-fixed reference frame. It usually has complex conjugate poles on the complex plane. This dynamics couples with the roll angle and the sideslip angle.

The poles in the longitudinal study are -0.124±0.0715j, -1.72, and 0.0571. Real poles belong to the phugoid mode. One of the poles is positive, which means it is unstable. Because there is instability, in this case, the case does not meet any criteria. For the second case, the poles of phugoid mode are at -0.00201±0.0827j with 0.0243 damping ratio and 0.0827 rad/s natural frequency. The damping ratio is less than 0.04; therefore, Level 1 criteria are not met. However, the criteria for Level 2 is a damping ratio greater than 0; therefore, it is satisfied. This means although the response is relatively slow, the oscillatory response in phugoid mode eventually stabilizes.

The poles for the short period mode in the first flight condition are -0.124±0.0715j for short period frequency and dampening. The short period mode has a damping ratio of 0.867 and a natural frequency of 0.143 rad/s. The natural frequency of 0.143 does not meet any Level 1, 2, or 3 criteria for category A flights. However, it satisfies the requirements for some factor sensitivity parameters in category B. The damping ratio satisfies the criteria of being at least 0.05 for flight phase category B. The short-period modes for the second flight condition are in the -0.413±0.364j, with a damping ratio of 0.75 and a natural frequency of 0.551 rad/s. The damping ratio is sufficient once more, and the natural frequency is greater than in the previous case. The behavior satisfies the requirements of flight phase category B for all aircraft classes and C for aircraft class II-L and III for level 2 regarding standard MIL-STD-1797A. However, it does not fit categorie A and C for aircraft I, II-C, and IV for level 2.

For spiral mode, minimum time to double amplitude condition of lateral mode, the pole for the spiral mode is located in -0.0185, which is very close to the imaginary axis that makes this mode very slow to develop in the real case. Any real value that is smaller than 0.693 / T_{2min} is in compliance with spiral mode requirements. Where T_{2min} is the minimum time to double amplitude. Since the pole here is negative, it is guaranteed to be smaller than the required value. For the second flight condition, the scenario is similar. Although the pole magnitude is smaller, -0.006, it still lies on the left-hand side of the required value. This means that all the levels of spiral mode handling are achieved.

For maximum roll mode time constant, the pole of the roll mode is -3.19 for the first flight condition. The compliance region for roll mode root is $-1/T_{rmax}$. The T_{rmax} takes the values of 1.0, 1.4, 3.0, and 10 for different handling quality levels, yet -3.19 remains on the compliance region for any of them, so the behavior meets all the level's criteria. However, the second flight condition's roll mode pole is -0.848, which means while still meeting most of the requirement T_{rmax} values, it does not satisfy the requirements when the T_{rmax} is 1.0. Since the root would lie in the right-hand side of this value, outside of the compliance region. Therefore, in this

condition, the handling qualities meet the criteria for Level 2 and Level 3. However, there are some shortfalls for Level 1.

For the minimum dutch-roll frequency and damping, the complex conjugate poles of dutch-roll modes are located in $-0.384 \pm 2.72j$ with 0.139 damping ratio and 2.75 rad/s natural frequency. The damping ratio falls within satisfactory region for the Level 3 and Level 2 qualities; however, it only meets the requirement for B and C flight categories for Level 1. The minimum natural frequency is quite enough for each level, but the damping ratio is the limiting factor here. For the second condition, the complex conjugate poles of the dutch-roll mode are $-0.244 \pm 2.03j$. The damping ratio of the dutch-roll mode is 0.119, and the natural frequency is 2.05 rad/s. Again, the natural frequency is quite enough, while the damping ratio still falls short of meeting the Level 1 category A criteria. Handling qualities are classified as the same for both conditions.

6. Conclusions

A Simulink model is developed in this paper to simulate F-16 dynamics. The aircraft's equation of motion is also simulated. Some properties like Mach number, altitude change with aircraft dynamics, and aircraft's actuator dynamics are also included in the system designed to make it more realistic. Then, the nonlinear aircraft dynamics are linearized around the trim conditions. The trim conditions of the aircraft are tried to be found as much as accurately using global search algorithms. Because it is also important for the accuracy of the linearized model. After finding the linearized model, the transfer functions are analyzed for frequency response and flying quality criteria. Along with the analysis in the frequency domain, mode analysis has a vital role, especially for flight performance. The phugoid, short period, roll mode, spiral mode, and dutch-roll modes were investigated longitudinally and latitudinally, respectively. It has been seen that the stability augmentation system and control augmentation system design has a critical importance for the modes with unstable or long steady-state duration. In order to make these designs, classification, level, and category of the aircraft must be determined in accordance with MIL-STD-1797A standards. For case 1, it is found that the longitudinal transfer function is unstable, which is caused by aircraft parameters coupling with different atmospheric conditions. On the other hand, for the second case, both lateral and longitudinal linearized dynamics are found as stable condition.

The results obtained for the flight at these two different altitudes reveal the effect of altitude on flight performance. It is also used as performance evaluation criteria in analyzes such as fuel consumption, controller performance, and actuator saturation of the change in flight performance. The stability augmentation system and autopilot design for F-16 aircraft will be the topic of further research after this study.

CRediT Author Statement

Abdurrahim Bilal Özcan: Conceptualization, Methodology, Software, Data curation, Writing- Original draft preparation. **Elbrus Caferov**: Supervision, Validation, Writing- Reviewing and Editing.

Nomenclature

MIMO	: multi-input multi-output
MIL	: military
dB	: decibel
$\dot{V}_T$	: wind velocity rate (m/s^2)
$\dot{\beta}$	: sideslip velocity rate (m/s^2)
$\dot{a}$	: angle of attack velocity rate (m/s^2)
$\dot{p}$	: roll velocity rate (rad/s^2)
$\dot{q}$	: pitch velocity rate (rad/s^2)
$\dot{r}$	: yaw velocity rate (rad/s^2)
$\dot{x}$	: forward velocity (m/s)
$\dot{y}$	: horizontal velocity (m/s)
$\dot{z}$	: vertical velocity (m/s)
Φ	: roll angle (rad)
Θ	: pitch angle (rad)
Ψ	: yaw angle (rad)
$\dot{u}$	: forward velocity rate (rad/s^2)
$\dot{v}$	: horizontal velocity rate (rad/s^2)
$\dot{w}$	: vertical velocity rate (rad/s^2)
H	: angular momentum (Nm/s^2)
M_{ext}	: external momentum (Nm/s)
T_{idle}	: thrust of idle condition
T_{mil}	: thrust of military condition
f_{TD}	: function of translational dynamics
f_{RD}	: function of rotational dynamics
f_{TK}	: function of translational kinematics
f_{RK}	: function of rotational kinematics

References

Atangana, A., Akgül A., 2020. Can Transfer Function and Bode Diagram Be Obtained from Sumudu Transform. Alexandria Engineering Journal, 59(4), pp.1971-1984 https://doi.org/10.1016/j.aej.2019.12.028.

Atak, K.U. 2020, Aircraft Model and Flight Control System Design, Master Thesis, Department of Control and Automation Engineering, Istanbul Technical University, İstanbul, June.

Bajodah, A. H., Mibar, H., Ansari, U. 2018, Aircraft Motion

Decoupling of Roll and Yaw Dynamics Using Generalized Dynamic Inversion Control. 26th Mediterranean Conference on Control and Automation (MED), Zadar, Croatia, pp.1–9. doi: https://10.1109/MED.2018.8442505.

Dündar, Ö., Bilici M., Ünler T., 2020. Design and performance analyses of a fixed wing battery VTOL UAV,

Engineering Science and Technology, an International Journal, Volume 23, Issue 5, pp. 1182-1193, DOI: https://doi.org/10.1016/j.jestch.2020.02.002.

Fu M. 1990. Computing the frequency response of linear systems with parametric perturbation. Systems & Control Letters, 15(1), pp.45-52, https://doi.org/10.1016/0167-6911(90)90043-T.

Garza, F. R., Morelli E. A., 2003, A Collection of Nonlinear Aircraft Simulations in MATLAB. NASA Langley Research Center, Hampton, Virginia, available at: https://www.cs.odu.edu/~mln/ltrs-pdfs/NASA-2003-tm212145.pdf (accessed 22 March 2022).

Greenberg, H., 1951, A Survey of Methods for Determining Stability Parameters of an Airplane from Dynamic Flight Measurement. Ames Aeronautical Laboratory Moffett Field, Calif, Washington, available at: https://ntrs.nasa.gov/api/citations/19930082979/downloads/19930082979.pdf (accessed 22 March 2022).

Hess, R.A. 2007, Frequency-Domain Design/Analysis of Robust Flight Control Systems. In System Control Technologies, Design Considerations & Integrated Optimization Factors for Distributed Nano UAV Applications, Available at: https://www.sto.nato.int/publications/STO%20Educational%20Notes/RTO-EN-SCI-175/EN-SCI-175-03.pdf (accessed 22 March 2022).

Jafarov, E.M., Tasaltm, R., 1999. Design of Longitudinal Variable Structure Flight Control System for the F-18 Aircraft Model with Parameter Perturbations, Kohala Coast, USA , (), pp.607–612. https://doi:10.1109/cacsd.1999.808716

Klein V., 1978, Aircraft Parameter Estimation in Frequency Domain. American Institute of Aeronautics and Astronautics 4th Atmospheric Flight Mechanics Conference, https://10.2514/6.1978-1344.

Klein V., 1980, Maximum Likelihood Method for Estimating Airplane Stability and Control Parameters from Flight Data in Frequency Domain. NASA Technical Paper 1637. The George Washington University, Langley Research Center, available at: https://ntrs.nasa.gov/api/citations/19800015831/downloads/19800015831.pdf (accessed 22 March 2022).

MIL-F-8785C, 1980, Military Specification-Flying Qualities of Piloted Airplanes.

Millidere M., 2021, Optimal Input Design and System Identification for an Agile Aircraft. A Thesis Submitted to The Graduate School of Natural and Applied Sciences, Middle East Technical University.

Milliken, W. F., 1947. Progress in Dynamic Stability and Control Research, Journal of the Aero. Sci., Vol. 14, pp.494 519.

Morelli, E. A., 2000. Real-Time Parameter Estimation in the Frequency Domain. Journal of Guidance, Control, and Dynamics, 23(5), pp.812–818. https://doi:10.2514/2.4642.

Morelli E. A., Grauer J. A., 2020. Practical Aspects of Frequency-Domain Approaches for Aircraft System Identification, Journal of Aircraft 21(3), pp.268–291.

Morelli E. A., Jared C., 2015. Frequency-Domain Method for Automated Simulation Updates Based on Flight Data. Journal of Aircraft, 1(14). https://10.2514/1.C033121.

Nguyen, L. T., Marilyn E., Ogburn M.E., Gilbert W.P., Kibler K.S., Brown P.W., Deal P.L., 1979, Simulator study of stall/post-stall characteristics of a fighter airplane with relaxed longitudinal static stability (Vol. 12854). National Aeronautics and Space Administration, available at: https://ntrs.nasa.gov/api/citations/19800005879/downloads/19800005879.pdf, (accessed 22 March 2022).

Shukla, V. V., Nusrath K., 2017. Modeling & Identification of High Performance Aircraft in Frequency Domain. Journal of Mechanical and Aeronautical Engineering Research, 1(1), pp 38 – 45.

Sonneveldt L., 2006, Nonlinear F-16 model description, Control &Simulation Division, Faculty of Aerospace Engineering, Delft University of Technology.

Stevens, B.L. and Lewis, F.L., 1992. Aircraft Control and Simulation. John Wiley and Sons Ltd. ISBN 0471613975.

Stevens, B. L., Lewis, F. L., Johnson, E. N., 2015. Aircraft Control and Simulation: Dynamics, Controls Design, and Autonomous Systems, 3rd Edition. John Wiley and Sons. Hoboken, New Jersey.

Wescott T., 2006. Applied Control Theory for Embedded Systems, A volume in Embedded Technology, DOI: https://doi.org/10.1016/B978-0-7506-7839-1.X5000-4.

International Journal of Aviation Science and Technology

Research Article

Modeling and Control of a Fixed-Wing High-Speed Mini-UAV

Mesut Bilici[1]*, Mehmet Karalı[2]

[1] Necmettin Erbakan University, Faculty of Aviation and Space Sciences, İstanbul, Turkiye
mbilici@erbakan.edu.tr - 0000-0002-0016-1600

[1] Necmettin Erbakan University, Faculty of Engineering, İstanbul, Turkiye
mkarali@erbakan.edu.tr - 0000-0002-2380-0575

Abstract

High-speed Unmanned Aerial Vehicles (UAVs) will be an interesting subject of study in today's aviation technology because of their ingenuity in obtaining high speeds while maintaining good maneuverability. In this study, modeling and control of a fixed-wing high-speed mini-UAV are performed. Aerodynamic analyses of the vehicle with a wingspan of 1.2 meters and a total take-off weight of 1.1 kg are done with the help of some computational fluid dynamics software. A developed MATLAB/Simulink code evaluates flight performance after a doublet control surface disturbance with six-degrees-of-freedom flight simulations in both longitudinal and lateral directions by a developed MATLAB/Simulink code. The transfer functions are obtained by trimming the aircraft at wing-level for a speed of 155 km/h, and the maximum speed that the mini-UAV could reach is calculated as 400 km/h. Two kinds of different linear controllers are designed to hold the pitch angle of the vehicle to the desired value. The time responses of the controllers are represented, and the elevator deflection effort is evaluated. Finally, a compulsive pitch angle is wanted to be tracked by the two controllers, and their responses are compared in terms of performance and stability.

Keywords

Mini-UAV
High-speed
6DOF simulation
PID controller
LQR controller

Time Scale of Article

Received 20 January 2022
Revised to 9 May 2022
Accepted 15 May 2022
Online date 28 June 2022

1. Introduction

Unmanned aerial vehicles (UAVs) have made significant development in both study and application over the last few decades because they replaced manned aircraft in a variety of crucial and precarious operations. For the time being, the two most common types of mini-UAV platforms are fixed-wing conventional aircraft and Vertical Take-Off and Landing (VTOL) aircraft, each with its own set of connatural constraints in terms of flight performance, payload, endurance, maximum high speed, and so on (Saeed et al., 2015). Although VTOLs have their worthy features, performance losses and high consumption values, especially in cruise flights, limit them for fast-speed missions (Dündar et al., 2020). Small fixed-wing conventional UAVs usually cause mission limitations with low cruise speeds and low altitude operations (Çoban, 2019). On the other hand, while the fixed-wing conventional UAVs are more suited to applications requiring long-distance cruise duties, they are generally slow in terms of cruise speed (Khan et al., 2012). These disadvantages of popular small UAVs highlight high-speed UAVs for operations that are necessary to be fast.

Many studies have been carried out on the modeling and control of fixed-wing UAVs. Modeling, simulation, and control design for the longitudinal dynamics of a UAV with a highly stable fixed-wing and dual H-type tail assembly were carried out with USAF DATCOM and X-Plane (Mobarez et al., 2017). In this study, it is determined

*: Corresponding Author Mesut Bilici mbilici@erbakan.edu.tr
DOI: 10.23890/IJAST.vm03is01.0104

that the system responses given by both methods are similar. Aerodynamic analysis, simulation, and flight controller design of a small flying wing UAV were performed for a steady level trim speed of 15 m/s (Wang et al., 2021, Bautista-Medina et al., 2021). To overcome the mortal problem of the linearized model's narrow implementation range, a comprehensive non-linear model of a small battery-powered flying wing UAV was well constituted. In another study (Mekuria et al., 2021), mathematical modeling and designing some controllers of a fixed-wing UAV are evaluated. To avoid singularity in this system, a six-degrees-of-freedom (6DOF) equation of motion was created, and the three rotational angles were constrained. Finally, a non-linear PID control technique is devised for tracking difficulties, airspeed, and attitude control of the vehicle. On the other hand, tilt-wing UAV studies on modeling and control have also been carried out. The mode transition of a new-style dispended propulsion tilt-wing UAV is studied using a multibody attitude dynamics model (Wang et al., 2019). A new finite-time robust controller for altitude dynamics is proposed that can guarantee zero errors in terms of external disturbances while also displaying robustness to force inputs. Furthermore, for the attitude dynamic, a new-based tracking controller is proposed. In a similar study, a dual tilt-wing UAV in vertical flight was developed, modeled, and controlled with a PD-type controller (Sanchez-Rivera et al., 2020). In addition, aerodynamic distortions and vortexes that occur in VTOL aircraft, especially in transitions, have also been studied in detail (Kaya et al., 2021).

Another frequently used technique for controlling mini-UAVs is the Linear Quadratic regulator (LQR) method. In a study, LQR is developed for a fixed-wing UAV during the waypoint search mission, and it is capable of maintaining its trajectory on its own (Ashari et al., 2019, Philips et al., 2002). This LQR controller is accompanied by a proportional gain, increasing the stability of the system. Dharmawan et al. have developed an LQR-based control algorithm for a fixed-wing UAV that can overcome obstacles. Both Proportional Integral Derivative (PID) and LQR control methodologies with a method of integrated action controls were employed to create the lateral and longitudinal control for fixed-wing Micro Aerial Vehicles (MAVs) (Anjali et al., 2016). Results for this study are represented by MATLAB and Simulink, and it is stated that the LQR controller has a higher level of disturbance rejection and overall performance. The optimal control approach is used to create an altitude control system for a mini-UAV with the Kalman filter approach to make the controller more effective (Hajiyev et al., 2013). The simulations show that employing a Kalman filter to predict states' values when there are disturbances improves the LQR controller's performance significantly.

The concept of high-speed UAV is virtually a new term in the aviation literature (Yin et al., 2021). Definition of high-speed UAV is generally used for jet-powered aircraft intended to be used as target UAV (LJ-1, 2019) or supersonic jets (Bougas et al., 2013). Target UAVs are often vehicles with enough space for gasoline and jet engines, as well as a delta wing design that addresses structural difficulties. On the other hand, most fixed-wing electric-powered mini aircraft, which can reach high speeds of about 500 km/h with their small dimensions, are model aircraft used in pylon races (Pylon Racer, 2013).

In this study, the mini-UAV design named Kuzgun is inspired by the fixed-wing electric-powered racing aircraft. Although racing aircraft are not evaluated in the UAV class under normal conditions, in this work, a hybrid design is determined as a research subject that has a general aerodynamic design characteristic of fixed-wing electric-powered racing aircraft with the flight controllers achieving autonomous flight. First, the geometric parameters design of the vehicle is carried out to provide high-speed and low drag. The aerodynamic coefficients and derivations are obtained using Xflr5 and USAF DATCOM with a wide range of flight conditions. Flight simulation studies are implemented with the linearized 6DOF equations of motion by performing thrust, servomotor, atmospheric, gyroscopic, and gravitational modeling. The open-loop system response of the mini-UAV against doublet elevator and rudder inputs with a 5-degree deflection angle is investigated in both longitudinal and lateral directions with the help of a code developed in MATLAB/Simulink. Finally, two different linear controllers, which are PID (Kaba, 2020) and LQR, are designed for mini-UAV, and time-dependent results are compared with elevator effort.

2. Modeling the Mini-UAV

2.1. High-speed Mini-UAV

The aircraft considered in this study is a high-speed fixed-wing electric-powered mini-UAV that is designed to reach high speeds, especially in pull-down maneuvers. The mini-UAV has a 1.2 m long wingspan with a relatively large wing area and high aspect ratio to provide both high-speed and stable flying characteristics with sufficient lift. The MH-30 airfoil, with a thickness of 7.74% and a low drag and moment coefficient, is selected owing to less drag and better performance in terms of maximum speed compared to the similar profiles. It is modified by slightly flattening the base towards the rear so that the total drag and moment coefficient value of the profile is reduced, and it has been made more producible. Modified wing airfoil provides a wide speed range so that the mini-UAV will have a great climb and wind penetration capability affording low drag at high

speeds while maintaining good lift and docile handling at lower speeds.

The increased dihedral angle at the tip of the wing reduces the wing-tip vortices. The wing and the stabilizers are located inline so that the total drag is minimized. The fuselage has a small frontal area and square-like sections to be manufactured easily and to accommodate the large battery and the payload while decreasing total drag. The maximum take-off weight of the mini-UAV is 1.1 kg with a maximum 200-gram payload. The vertical stabilizer has almost zero taper ratio with enough rudder efficiency to decrease the total drag of the vehicle. High-speed mini-UAVs are comparably listed with some physical and flight characteristics in Table 1. In addition, some geometric specifications with aerodynamic characteristics and a perspective view of high-speed mini-UAV designed are given in Table 2 and Figure 1, respectively.

Table 1. High-speed mini-UAVs

Mini-UAV	Wingspan [mm]	Wing area [m²]	Aspect ratio	Maximum total weight [g]	Length [mm]	Maximum speed [km/h]
Stinger ARF	950	0.135	6.68	550	760	330
Snipp FG	1300	0.185	9.1	870	725	375
Acro-Prism	1600	0.308	8.3	1250	1100	340
Monster 1.1 SpreadTowsa	1450	0.225	9.34	790	1150	440
Sabre F5B	1710	0.22	13.2	890	1000	390
Kuzgun	1200	0.144	9.98	1100	810	400

The total take-off weight of the mini-UAV, which is designed to have a larger payload volume, is slightly higher than that of other aircraft. The maximum speeds of the investigated vehicles are almost the same with electric power. Apart from this, it is seen that there is a certain ratio between the wingspans and weights of the vehicles.

2.2. 6DOF Equations of Motion

According to (Nicolosi et al., 2013, Padfield, 1996), the twelve equations that make up the non-linear model for fixed-wing aircraft dynamics are based on a body-fixed reference frame. A high-speed fixed-wing mini-UAV can be thought of as a rigid body that moves in three dimensions while being influenced by gravity, aerodynamic, and propulsive forces. As a result, it's a six-degrees-of-freedom (6DOF) system with three translational and three rotational DOF. For such a system, non-linear equations of motion are given in Equation (1).

$$X = m(\dot{u} + qw - rv) \quad (1.1)$$

$$Y = m(\dot{v} + ur - pw) \quad (1.2)$$

$$Z = m(\dot{w} + pv - qu) \quad (1.3)$$

$$L = \dot{p}I_{xx} - I_{xy}(\dot{q} - pr) - I_{xz}(\dot{r} + pq) + (I_{zz} - I_{yy})qr + I_{yz}(r^2 - q^2) \quad (1.4)$$

$$M = \dot{q}I_{yy} - I_{yz}(\dot{r} - pq) - I_{xy}(\dot{p} + qr) + (I_{xx} - I_{zz})pr + I_{xz}(p^2 - r^2) \quad (1.5)$$

$$N = \dot{r}I_{zz} - I_{xz}(\dot{p} - qr) - I_{yz}(\dot{q} + pr) + (I_{yy} - I_{xx})pq + I_{xy}(q^2 - p^2) \quad (1.6)$$

In Equation (1), X, Y, and Z represent total weight, aerodynamic and propulsion forces, L, M and N are the total moments acting on the vehicle, including reaction torque and gyroscopic moments exerted by the thruster on the mini-UAV. Aircraft motion is symbolized by three translational velocity components, u, v, and w, and three rotational velocity components, p, q, and r, which are called body rates. m represents the mini-UAV's total weight, I_xx, I_yy, and I_zz are moments of inertia, while I_xy, I_yz, and I_xz express the product of inertias. To simplify the non-linear equations of motion, numerous assumptions are applied. The mini-UAV's center of gravity will not have a relative velocity for the body-fixed reference frame because the airframe is presumed to be a rigid body. Second, the mini-UAV mass is assumed to be constant since it is powered with electricity, and finally, mass distribution is assumed to be constant during the flight, resulting in a constant inertia tensor. In addition, equations of motion are typically used in body-fixed axes, earth-fixed frames, and wind axes.

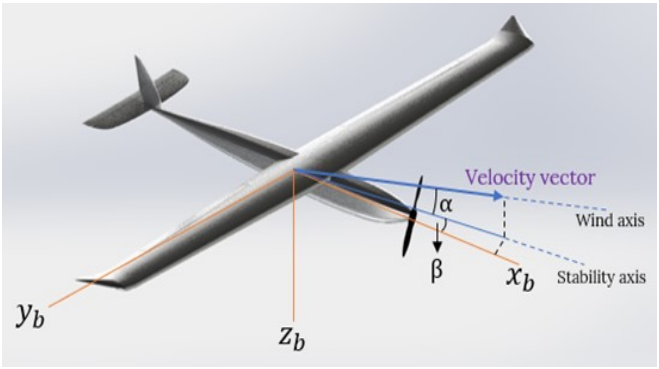

Fig. 1. Fixed-wing high-speed mini-UAV with frames

Obtaining the aerodynamic coefficients is carried out in the wind-axis body frame (Panagiotou et al., 2014). However, all measurement devices are placed on the body-fixed frame to be able to measure the flight characteristics such as velocity and altitude. Therefore,

a relationship and transformation between the different axes on the mini-UAV are inevitable. In other words, transformation matrices are required to transform

Table 2. Fixed-wing high-speed mini-UAV properties

Wingspan [mm]	Wing area [m²]	Mean aerodynamic chord [mm]	Aspect ratio	Taper ratio	Root-tip sweep angle [°]	Tip twist angle [°]	Dihedral Angle [°]
1200	0.144	124	9.98	0.067	8.34	-1.5	1 at root 10 at tip
Maximum take-off weight [N]	I_{xx} [kg.m²]	I_{yy} [kg.m²]	I_{zz} [kg.m²]	Center of gravity from nose [m]	Cruise speed [m/s]	Maximum speed [m/s]	Maximum g-load
10.79	0.036	0.0326	0.0686	0.251	43	111	2.3
Wing airfoil	Mh-30 modified	Horizontal tail airfoil	NACA 0009	Vertical tail airfoil	NACA 0009	Maximum payload	200 g

between variables stated in the inertial and body frames. The most used kinematic transformation is between body rates and time rates of change of the Euler angles (ϕ ˙, θ ˙, and ψ ˙) as given in Equation (2).

$$\begin{pmatrix}\dot{\phi}\\ \dot{\theta}\\ \dot{\psi}\end{pmatrix}=\begin{pmatrix}1 & tan\theta sin\phi & cos\phi tan\theta\\ 0 & cos\phi & -sin\phi\\ 0 & sec\theta sin\phi & sec\theta cos\phi\end{pmatrix}\begin{pmatrix}p\\ q\\ r\end{pmatrix} \quad (2)$$

Another widely used conversion is from earth-fixed frame to wind-axis frame as given in Equation (3). x ˙, y ˙, and z ˙represent the trajectory directions.

2.3. Aerodynamic Modeling

Estimating the aerodynamic coefficients and derivatives is the most severe and, at the same time, the most crucial part. Aerodynamic coefficients and derivatives are assigned as inputs to 6DOF simulations as well as for the designed controllers. In addition, different flow conditions can cause significant changes in the coefficient and its derivatives. The aerodynamic coefficients can be explained in different methods. However, in this study, a basic but logical formula (Gryte et al., 2018) is performed, as shown in Equation (4) and Equation (5).

Where α and β show the angle of attack, the sideslip angle, δ_e, δ_a, and δ_r represent the elevator, aileron, and rudder deflection angles, respectively. In addition, C_L, C_D, and C_Y are the lift, drag, and side force coefficients, respectively. C_l, C_m, and C_n refer to the aerodynamic moments along the x, y, and z-axis of the body-fixed-frame, respectively. All the aerodynamic coefficients are calculated in compliance with the given equations through Xflr5 and USAF DATCOM and are represented in Table 3. The ungiven coefficients are neglected.

$$\begin{pmatrix}\dot{x}\\ \dot{y}\\ \dot{z}\end{pmatrix}=\begin{pmatrix}\cos\psi cos\theta & \cos\psi sin\theta sin\phi-sin\psi cos\phi & \cos\psi sin\theta cos\phi+sin\psi sin\phi\\ sin\psi cos\theta & \sin\psi sin\theta sin\phi+cos\psi cos\phi & \sin\psi sin\theta cos\phi-sin\psi sin\phi\\ -sin\theta & cos\theta sin\phi & cos\theta cos\phi\end{pmatrix}\begin{pmatrix}u\\ v\\ w\end{pmatrix} \quad (3)$$

$$\begin{bmatrix}C_L\\ C_D\\ C_Y\end{bmatrix}=\begin{bmatrix}C_{L_0}+C_{L_\alpha}\alpha+C_{L_q}(c/2V)\,q+C_{L_{\delta_e}}\delta_e\\ C_{D_0}+C_{D_\alpha}\alpha+C_{D_{\delta_e}}\delta_e+C_{D_\beta}\beta+C_{D_q}(c/2V)\,q\\ C_{Y_0}+C_{Y_\beta}\beta+C_{Y_p}(b/2V)\,p+C_{Y_r}(b/2V)\,r+C_{Y_{\delta_a}}\delta_a+C_{Y_{\delta_r}}\delta_r\end{bmatrix} \quad (4)$$

$$\begin{bmatrix}C_l\\ C_m\\ C_n\end{bmatrix}=\begin{bmatrix}C_{l_0}+C_{l_\beta}\beta+C_{l_p}(b/2V)\,p+C_{l_r}(b/2V)\,r+C_{l_{\delta_a}}\delta_a+C_{l_{\delta_r}}\delta_r\\ C_{m_0}+C_{m_\alpha}\alpha+C_{m_{\delta_e}}\delta_e+C_{m_q}(c/2V)\,q\\ C_{n_0}+C_{n_\beta}\beta+C_{n_p}(b/2V)\,p+C_{n_r}(b/2V)\,r+C_{n_{\delta_a}}\delta_a+C_{n_{\delta_r}}\delta_r\end{bmatrix} \quad (5)$$

Table 3. Aerodynamic coefficients and derivatives

Coefficient	Value	Coefficient	Value	Coefficient	Value	Coefficient	Value
C_{L_0}	0.177	C_{D_q}	0	C_{l_β}	-0.13	$C_{m_{\delta_e}}$	-0.99
C_{L_α}	5.61	C_{Y_0}	0	C_{l_p}	-0.51	C_{m_q}	-38.21
$C_{L_{\delta_e}}$	0.13	C_{Y_β}	-0.83	C_{l_r}	0.25	C_{n_β}	0.073
C_{D_0}	0.023	C_{Y_p}	0	$C_{l_{\delta_a}}$	0.17	C_{n_p}	-0.069
C_{D_α}	0.027	C_{Y_r}	-0.013	$C_{l_{\delta_r}}$	0.0024	C_{n_r}	-0.095
$C_{D_{\delta_e}}$	0.0135	$C_{Y_{\delta_a}}$	0.075	C_{m_0}	0.0135	$C_{n_{\delta_a}}$	-0.011
C_{D_β}	0.037	$C_{Y_{\delta_r}}$	0.19	C_{m_α}	-2.74	$C_{n_{\delta_r}}$	-0.068

2.4. Propulsion Modeling

The propulsion system of a fixed-wing UAV is composed of a propeller, brushless DC (Direct Current) motor, battery (Lithium Polymer or Lithium-Ion), and ESC (Electronic Speed Control). Since the mini-UAV has high speeds TP3640 7D-KV2080-4 brushless motor is selected with 3000 mAh 6S1P 22.2V Li-Po, 150A ESC, and 12x8 propeller.

The thrust of the high-speed mini-UAV is accepted to be composed of motor/propeller pair. The inputs to the thrust model will be the airspeed of the aircraft V and the throttle setting. It is accepted that the thrust and moment vectors produced by the propeller/motor pair are aligned with the rotation axes of the motor and are denoted by the magnitude of the thrust is T. The standard model for the thrust produced by a propeller is given by propeller theory (Mahmuddina, 2017) as Equation (6).

$$T = (\rho D^4/4\pi^2)\Omega C_T \tag{6}$$

where D is the diameter of the propeller, Ω is the propeller speed in radians per second, and C_T represents the thrust coefficient which is found from literature data. It is also assumed that the input voltage (V_in) of the battery is a linear function of the throttle level. Therefore, Equation (7) can be derived.

$$V_{in} = V_{max}\delta_t \tag{7}$$

When a DC motor drives the propeller, torques around the propeller and motor can be assumed as equal (Emhemed et al., 2012).

$$(\rho D^5/4\pi^2)C_{Q_0}\Omega^2 + (\rho D^4/2\pi C_{Q_1}V + ({K_Q}^2/R))\Omega + \rho D^3 C_{Q_2}V^2 - (K_Q/R)V_{in} + K_Q i_0 = 0 \tag{8}$$

where C_Q is a non-dimensional aerodynamic coefficient, K_Q is the motor torque constant, R is the resistance of the motor windings, i_0 is the no-load current. From Equation (8) operating speed of the propeller Ω can be calculated numerically.

2.5. Servomotor Modeling

The mini-UAV is fitted with two DC servo motors that control the aileron and elevator deflection. The servo motors' reaction characteristics will have a direct impact on the UAV's attitude control, so servo motor modeling is crucial. A second-order system technique (Sufendi et al., 2013) is utilized to model the servo motor. Equation (9) depicts the servo motor's transfer function with the classical notation method.

$$\frac{Y(s)}{X(s)} = \frac{95.53}{s^2+15.65s+95.53} \tag{9}$$

2.6. Atmospheric Modeling

The atmospheric sub-system returns density, temperature, pressure, dynamic and kinematic viscosity, speed of sound, and gravitation acceleration whereas the input is just altitude. In atmospheric modeling, the atmosphere is assumed to be steady and does not change with time (Daidzic, 2015).

2.7. Gyroscopic Modeling

Rotating rigid bodies have angular momentum and if an external moment acts on the rigid body that generates angular velocity, gyroscopic moments are generated to conserve previous angular momentum by producing a counter moment which is called the gyroscopic precession effect. The gyroscopic moment of the center of gravity can be calculated as given in Equation (10) where ω is the angular rate of the aircraft and H_P represents the transformation matrix from the propulsion reference frame to the body-fixed frame. x, y, and z subscripts denote the directions where the moments act on. Besides, i_B, j_B, and k_B represent unit vectors in the body frame.

$$\sum M_{Gy} = -dH_P/dt - \omega \times H_P = -\begin{pmatrix} (qH_{P,z} - rH_{P,y})i_B \\ (rH_{P,x} - pH_{P,z})j_B \\ (pH_{P,y} - qH_{P,x})k_B \end{pmatrix} \tag{10}$$

2.8. Gravitational Modeling

Gravitational force is calculated as given in Equation (11) due to the gravitation. F_G represents the gravitational force θ, and ϕ shows the orientation of the aircraft with respect to the reference frame, which is the earth's fixed-frame

$$F_G = \begin{pmatrix} -mg\ sin\theta \\ mg\ cos\theta\ sin\phi \\ mg\ cos\theta\ cos\phi \end{pmatrix} \tag{11}$$

2.9. Linearization of Non-linear Equations of Motion

Due to the need for accurate representations of the intricate vehicle dynamics, analyzing the stability of a non-linear system is challenging and time-consuming. In addition, since fixed-wing aircraft are linear in most of their flight by nature, it is quite reasonable to linearize the non-linear equations according to the Small Disturbance Theory (Philips et al., 2002) for the steady level flight trim condition. Besides, linear systems enable the use of linear controllers, which are a more straightforward and cost-effective method of developing controllers for fixed-wing UAVs. Linearized equations of motion around the steady, wings-level, trimmed flight of fixed-wing mini-UAV are given in Equation (12).

$$\Delta X = m(\dot{u} - Wq + (g\cos\theta_0)\theta) \tag{12.1}$$

$$\Delta Y = m(\dot{v} + Vr - Wp - (g\cos\theta_0)\phi) \tag{12.2}$$

$$\Delta Z = m(\dot{w} - Vq + (g\cos\theta_0)\theta) \tag{12.3}$$

$$\Delta L = I_{xx}\dot{p} - I_{xz}\dot{r} \tag{12.4}$$

$$\Delta M = I_{yy}\dot{q} \tag{12.5}$$

$$\Delta N = I_{zz}\dot{r} - I_{xz}\dot{p} \quad (12.6)$$

where V is forward speed, W is the total weight, θ_0 is the unperturbed flight path angle. While deriving these equations, it is assumed that angular velocities are zero, and some stability derivatives don't affect the steady level flight.

Modeling the high-speed fixed-wing mini-UAV with all circumstances, Figure 2 and Figure 3 represents the open-loop 6DOF simulation results for 155 km/h steady level trimmed flight which is developed by MATLAB/Simulink environment for longitudinal and lateral planes, respectively.

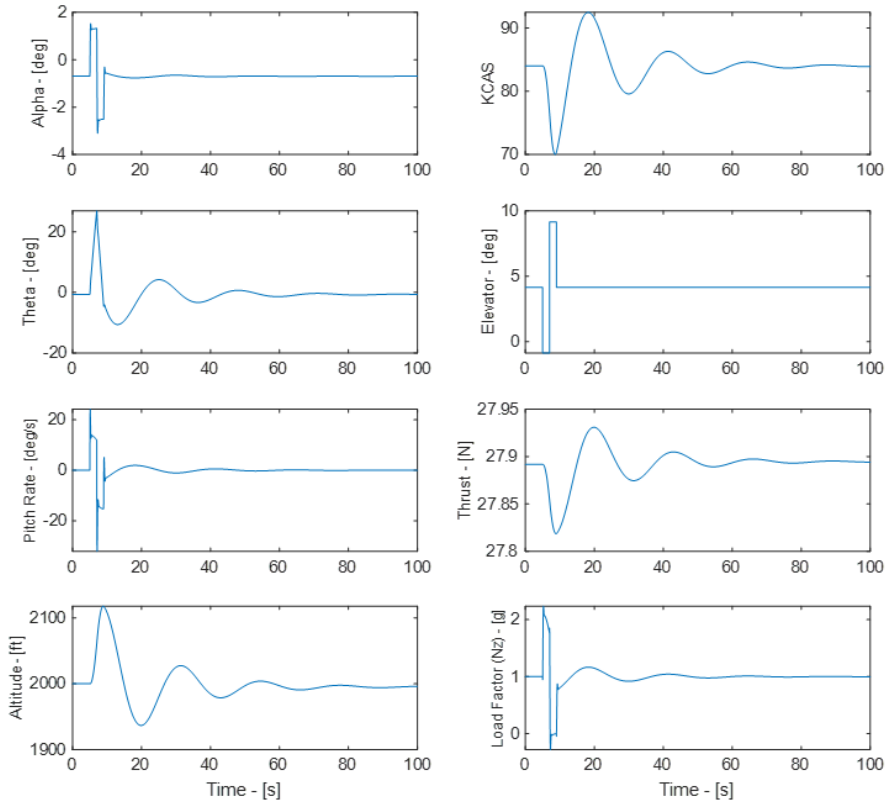

Fig. 2. Longitudinal open-loop 6DOF simulation results in Simulink

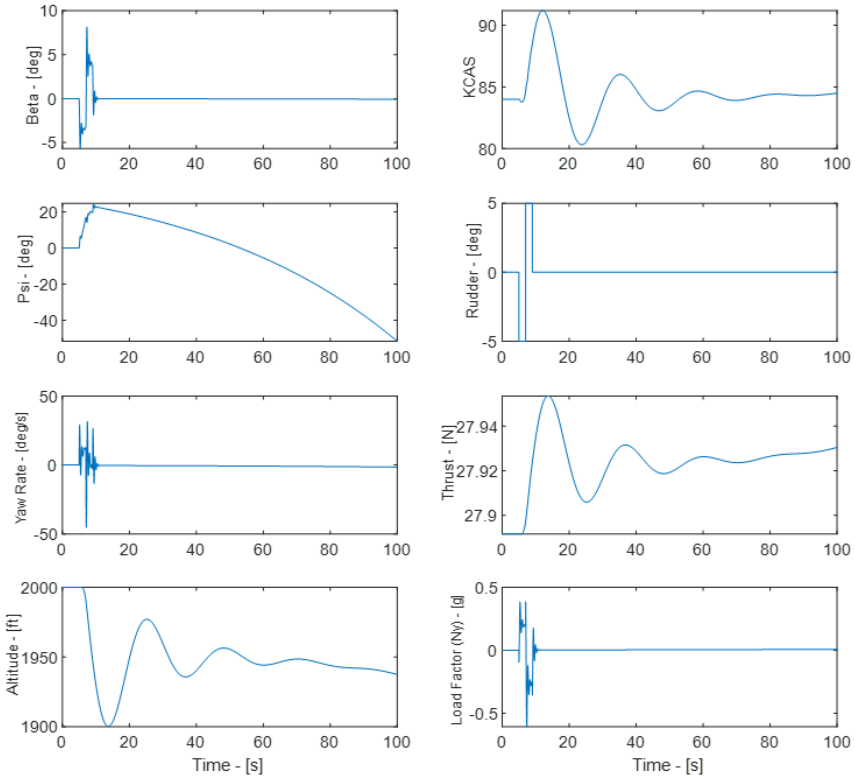

Fig. 3. Lateral open-loop 6DOF simulation results in Simulink

In the 100-second flight simulation, -5 and +5 degrees of doublet input are entered into the elevator and rudder at the 5th second of the flight, and the response of the mini-UAV is examined. The mini-UAV is inherently stable in all flight modes in the longitudinal direction, and its response to elevator disturbance causes a 10% fluctuation in altitude and speed. In the lateral direction, the vehicle is unstable only for spiral mode; this is due to the positive pole in the right half of the s-plane, which is +0.0164. For a highly maneuverable and high-speed mini-UAV, this instability in spiral mode can be easily tolerated (Yanık et al., 2014). The details of the longitudinal and lateral flight modes of the high-speed mini-UAV are presented in Table 4.

Table 4. Longitudinal and lateral flight modes properties

Short-period frequency [rad/s]	Short-period damping	Phugoid frequency [rad/s]	Phugoid damping	Dutch roll frequency [rad/s]	Dutch Roll Damping	Spiral Stability time to double [s]	Roll Mode time to half [s]
15.98	0.487	0.277	0.204	9.68	0.223	42.45	0.019

$$\begin{bmatrix} \Delta\dot{V}_T \\ \Delta\dot{\alpha} \\ \Delta\dot{q} \\ \Delta\dot{\theta} \end{bmatrix} = \begin{bmatrix} -5.7462 & 0.0725 & -3.0927 & 0 \\ -0.6821 & -0.0724 & 0.4032 & -9.8104 \\ 30.052 & -0.5229 & -5.0221 & -0.2225 \\ 1 & 0 & 0 & 0 \end{bmatrix} \begin{bmatrix} \Delta V_T \\ \Delta\alpha \\ \Delta q \\ \Delta\theta \end{bmatrix} + \begin{bmatrix} -0.8504 \\ -0.0050 \\ -0.0620 \\ 0 \end{bmatrix} \Delta\delta_e \quad (13)$$

3. Controller Design for Pitch Angle

The equations of motion are split into longitudinal motion, which includes variables V, α, q, θ, and lateral motion, which includes states β, ϕ, ψ, p, r, after linearization. The Linear state-space model of longitudinal and lateral dynamics is given in Equation (13). On the other hand, the effect of the throttle has been removed since linearization is done in an equilibrium flight condition where the thrust force is constant.

3.1. PID Controller

To keep the altitude constant, the PID controller design of the high-speed mini-UAV is carried out first. The elevator deflection angle versus the pitch angle transfer function is obtained as given in Equation (14). This transfer function has been tuned in the Simulink environment with the servo model transfer function given in section 3.3, and the controller design has been realized. The response of the PID controller for the reference angle of 30 degrees pitch angle and the effort of the elevator for this response are presented in Figure 4.

$$\frac{\theta(s)}{\delta_e(s)} = \frac{-48.73s^3 - 237.3s^2 - 27.86s}{s^4 + 10.84s^3 + 122.8s^2 + 10.52s + 19.38} \quad (14)$$

3.2. LQR-I Controller

LQR is a well-known approach for creating closed-loop stable and high-performance systems by providing appropriately managed feedback gains. The objective function J is minimized with the formation of the controller K. A feedback gain matrix is built in this technique to minimize the objective function J and establish a balance between the usage of the size, the speed of response, and the control exertion, resulting in a stable system.

$$J = \int_0^\infty (x^T Q x + u^T R u) dt \quad (15)$$

where Q and R are the weight matrices that must be a positive definite or positive semi-definite symmetry matrix. In order to minimize the cost function value, the controller K is calculated according to Equation (16)

$$K = R^{-1} B^T P \quad (16)$$

In Equation (15) P is calculated by solving the Algebraic Ricatti Equation (ARE) (Petersen et al., 1986). In addition, an integrator is added to the system to be able to procure zero steady-state error. The LQR-I controller design can be formulated as follows:

- Estimation of the matrices Q and R
- Calculation of P from ARE
- Finding the state feedback matrix K using $K = R^{-1}B^T P$

The response of the LQR-I controller for the reference angle of 30 degrees pitch angle and the effort of the elevator for this response are given in Figure 4. A challenging task for reference theta is given as input to the system, and the responses of the controllers are evaluated in Figure 5. The PID controller can successfully follow the desired reference value with a little overshoot. LQR-I controller, on the other hand, could not follow the reference value and left a steady-state error.

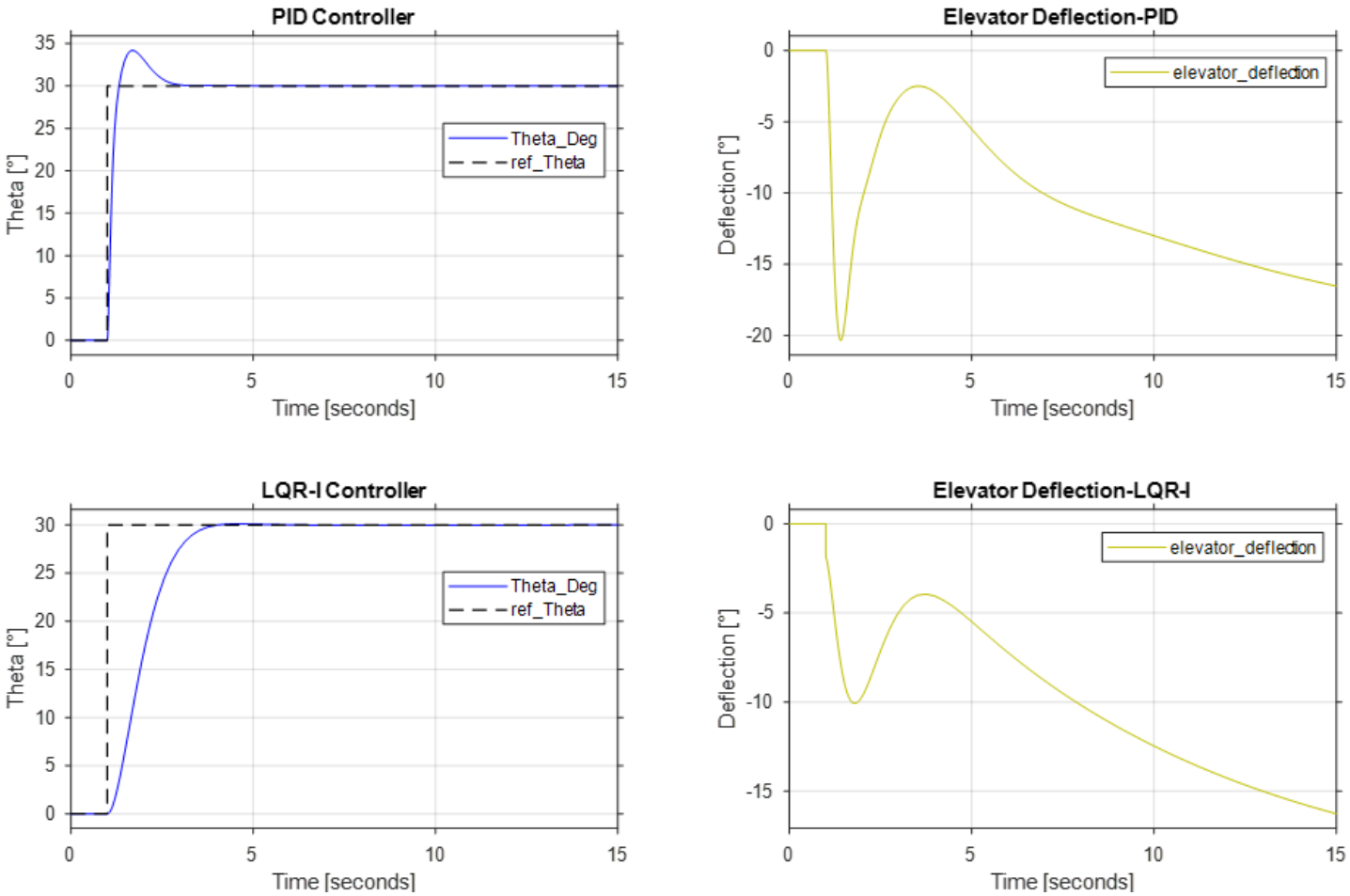

Fig. 4. Pitch angle control with PID and LQR-I controllers and corresponding elevator efforts

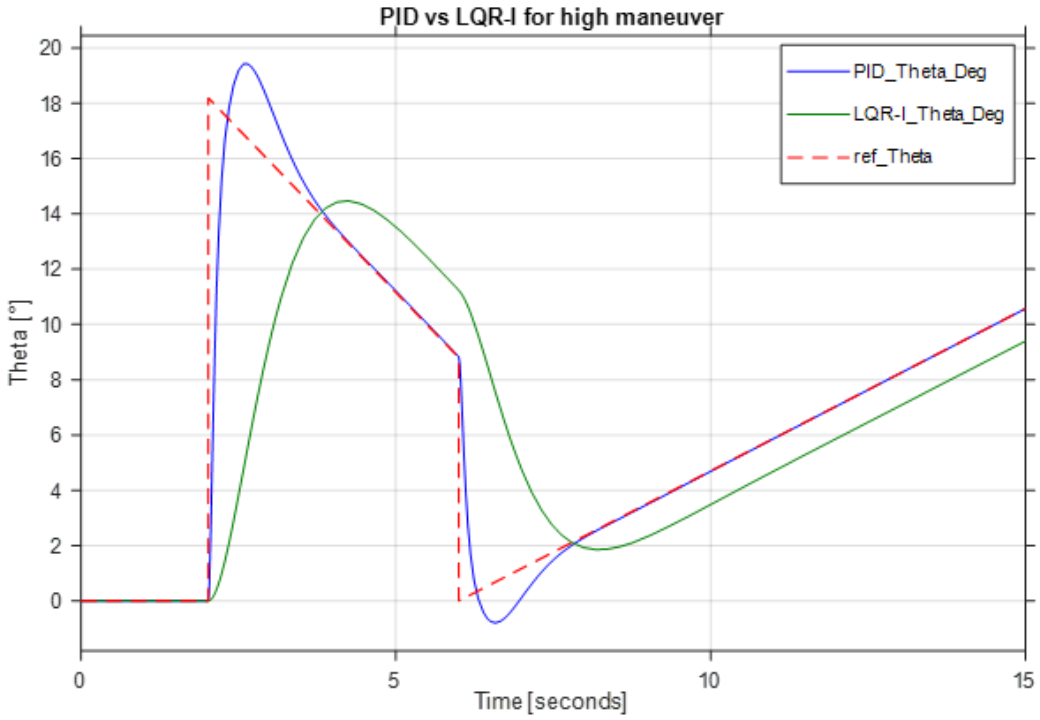

Fig. 5. PID vs LQR-I responses to a compulsive theta reference angle

4. Conclusion

In this study, 6DOF flight simulation studies and two different controller designs are carried out for a fixed-wing high-speed mini-UAV. Unlike standard fixed-wing UAVs, the high-speed mini-UAV can reach a speed of 400 km/h, especially in pull-down maneuvers, and has a

conventional design with a wingspan of 1.2 meters and a total take-off weight of 1.1 kg. The aerodynamic analysis of the mini-UAV and the derivation of its coefficients are obtained with Xflr5 and USAF DATCOM. Aerodynamic, propulsion, servomotor, gyroscopic, atmospheric, and gravitational modeling is performed under suitable conditions. 6DOF flight simulation studies are implemented with a code developed in MATLAB/Simulink environment. The simulation features and results suggest that:

- The mini-UAV is trimmed at 155 km/h wing-level, steady flight.
- The mini-UAV responses as statically and dynamically stable to the doublet elevator and rudder deflection angles.
- Load factor (n) exceeds the 2-g after the elevator disturbance
- Altitude and speed changes are observed slightly low after the control surface deflections.
- The mini-UAV is unstable for only the spiral flight mode in the lateral direction.
- Since the spiral mode requires long flight times, the pole placement method is not addressed to eliminate this instability

Both longitudinal and lateral transfer functions are obtained by considering the trim conditions in the 6DOF simulation studies. Two controllers are designed for high-speed mini-UAV using PID and LQR-I methods using these transfer functions. The main conclusions from the controller designs are:

- The PID controller responded to the reference theta angle of 30 degrees faster than the LQR-I controller.
- The PID controller has an overshoot and its settling time is shorter than the LQR-I controller. This situation caused the vehicle to respond faster to the reference value.
- LQR-I controller gives a smoother and late response without overshoot compared to PID.
- Elevator efficiency is good enough for both controllers to hold the theta angle in the desired value.
- For compulsory reference theta input, the PID controller can successfully follow the target reference value with a little overshoot.
- The LQR-I controller is unable to track the reference value and hence produces a steady-state error under the same compulsory reference theta input.

In conclusion, the PID controller results in a high-performance response with some overshoot, while the LQR-I controller imparts a low-performance response with high stability. In future work, a robust controller will be designed for the high-speed fixed-wing mini-UAV.

Abbreviations

UAV	:	Unmanned Aerial Vehicle
PID	:	Proportional Integral Derivative
LQR-I	:	Linear Quadratic Regulator with Integral
VTOL	:	Vertical Take-off Landing
6DOF	:	Six Degree of Freedom
DC	:	Direct Current
ESC	:	Electric Speed Control
CFD	:	Computational Fluid Dynamics

CRediT Author Statement

Mesut Bilici: Conceptualization, Methodology, Software, Investigation, Validation, Writing-Original Draft, Visualization. **Mehmet Karalı:** Resources, Data Curation, Supervision, Project administration.

References

Anjali, B. S., Vivek, A., & Nandagopal, J. L. (2016). Simulation and Analysis of Integral LQR Controller for Inner Control Loop Design of a Fixed Wing Micro Aerial Vehicle (MAV). Procedia Technology, (25), 76-83.

Ashari, A., Dharmawan, A., Fadhli, & H., Handayani, A. (2019). Flight Trajectory Control System on Fixed Wing UAV using Linear Quadratic Regulator. International Journal of Engineering Research & Technology (IJERT), 8(8), 2278-0181.

Bautista-Medina, J. A., Lozano, R., & Osorio-Cordero, A. (2021). Modeling and Control of a Single Rotor Composed of Two Fixed Wing Airplanes. Drones, 5(3), 92.

Bougas, L., & Hornung, M. (2013). Propulsion system integration and thrust vectoring aspects for scaled jet UAVs. CEAS Aeronautical Journal, 4(3), 327-343.

Çoban, S. (2019). Different Autopilot Systems Design for a Small Fixed Wing Unmanned Aerial Vehicle. Avrupa Bilim ve Teknoloji Dergisi, (17), 682-691.

Daidzic, N. E. (2015). Mathematical Model of Hot-Air Balloon Steady-State Vertical Flight Performance. Aviation, 25(3), 149-158.

Dharmawan, A., Putra, A. E., Tresnayana, M., & Wicaksono W. A. (2019, January). The Obstacle Avoidance System in A Fixed-Wing UAV When Flying Low Using LQR Method. In International Conference on Computer Engineering Network,

and Intelligent Multimedia (CENIM) (pp. 1-7

Dündar, Ö., Bilici, M., & Ünler, T. (2020). Design and performance analyses of a fixed wing battery VTOL UAV. Engineering Science and Technology, an International Journal, 23(5), 1182-1193.

Emhemed, A. A., & Mamat, R. B. (2012). Modelling and Simulation for Industrial DC Motor Using Intelligent Control. Procedia Engineering, 41, 420-425.

Gryte, K., Hann, R., Alam, M., Rohac, J., Johansen, T.A., & Fossen, T.I. (2018). Aerodynamic modeling of the Skywalker X8 Fixed-Wing Unmanned Aerial Vehicle. In Proceedings of the International Conference on Unmanned Aircraft Systems (ICUAS), (pp. 826–835).

Hajiyev, C., & Vural, S. Y. (2013). LQR Controller with Kalman Estimator Applied to UAV Longitudinal Dynamics. Positioning, 4(1), 36-41.

Kaba, A. (2020). A Comparative Study on the Tuning of the PID Flight Controllers Using Swarm Intelligence. International Journal of Aviation Science and Technology, 1(2), 80-91.

Kaya, M. N., Kok, A. R., & Kurt, H. (2021). Comparison of aerodynamic performances of various airfoils from different airfoil families using CFD. Wind and Structures, 32(3), 239-248.

Khan, W., & Nahon, M. (2015, June). Real-time modeling of agile fixed-wing UAV aerodynamics. In International Conference on Unmanned Aircraft Systems (ICUAS) (pp. 1188-1195).

LJ-1 (Target Drone), Available at: https://www.militarydrones.org.cn/lj-1-high-speed-target-drone-p00452p1.html, (accessed 1 March 2022)

Mahmuddina, F. (2017). Rotor Blade Performance Analysis with Blade Element Momentum Theory. Energy Procedia, 105(2017), 1123-1129.

Mekuria, S., Belete, M., & Niguse, B. (2021). Fixed Wing Unmanned Aerial Vehicle Control by Using a Non-linear PID Controller. Journal of Electrical Engineering, Electronics, Control and Computer Science, 7(24), 39-46.

Nicolosi, F., Vecchia, P. D., & Ciliberti, D. (2013). An investigation on vertical tailplane contribution to aircraft sideforce. Aerospace Science and Technology, 28(1), 401-416.

Yanık, N. S., Özyetiş, E., Güçlü, Ö., Kayran, A., Kıran, E., & Alemdaroğlu, N. (2014, May). Design and manufacturing of a high-speed jet powered UAV. In International Conference on Unmanned Aircraft Systems (ICUAS) (pp. 1073-1080).

Padfield, G., Helicopter Flight Dynamics (1996): The Theory and Application of Flying Qualities and Simulation Modeling. American Institute of Aeronautics and Astronautics.

Panagiotou, P., Kaparos, P., & Yakinthos, K. (2014). Winglet design and optimization for a MALE UAV using CFD. Aerospace Science and Technology, 39(2014), 190-205.

Petersen, I. R., & Hollot, C. V. (1986). A riccati equation approach to the stabilization of uncertain linear systems. Automatica, 22(4), 397-411.

Philips, W. F., & Santana, B. W. (2002). Aircraft Small-Disturbance Theory with Longitudinal&Lateral Coupling. Journal of Aircraft, 39(6), 973-980.

Pylon Racer (Racing aircrafts), Available at: https://icare-icarus.3dcartstores.com/Pylon-Racer-F5D_c_28.html, (accessed 1 March 2022)

Saeed, A., Younes, A. B., Islam, S., Dias, J., Seneviratne, L., & Cai, G. (2015, June). A review on the platform design, dynamic modeling, and control of hybrid UAVs. In International Conference on Unmanned Aircraft Systems (ICUAS) (pp. 806-815).

Sanchez-Rivera, L. M., Lozano, R., & Arias-Montano, A. (2020). Development, Modeling and Control of a Dual Tilt-Wing UAV in Vertical Flight. Drones, 4(4), 71.

Mobarez, E. N., Sarhan, A., & Ashry, M. M. (2019). Modeling of fixed wing UAV and design of multivariable flight controller using PID tuned by local optimal control. In IOP Conference Series: Materials Science and Engineering 610 (2019) 012016.

Sufendi, Trilaksono, B.R., Nasution, S.H., & Purwanto, E.B. (2013). Design and implementation of hardware-in-the-loop-simulation for UAV using PID control method. In Proceedings of the 3rd International Conference on Instrumentation, Communications, Information Technology, and Biomedical Engineering (pp. 124–130).

Wang, Y., Zhu, H., Zhao, Z., Zhang, C., & Lan, Y. (2021). Modeling, System Measurements and Controller Investigation of a Small Battery-Powered Fixed-Wing UAV. Machines, 9(12), 333.

Wang, Y., Zhou, Y., & Lin, C. (2019). Modeling and control for the mode transition of a novel tilt-wing UAV. Aerospace Science and Technology, 91(2019), 593-606.

Yin, Q., Wei, X., Nie, H., & Deng, J. (2021). Parameter effects on high-speed UAV ground directional stability using bifurcation analysis. Chinese Journal of Aeronautics, 34(11), 1-14.

International Journal of Aviation Science and Technology

Research Article

Design of a Wing Structure for a Single Turboprop Normal Category Aircraft

Phacharaporn Bunyawanichakul[1]*, Vis Sripawadkul[2]

[1] *Department of Aerospace Engineering, Faculty of Engineering, Kasetsart University, Bangkok, Thailand*
phacharaporn.b@ku.ac.th - 0000-0002-4904-3488

[2] *Department of Aerospace Engineering, Faculty of Engineering, Kasetsart University, Bangkok, Thailand*
fengvisp@ku.ac.th - 0000-0001-6238-6779

Abstract

This paper presents the wing design and structural analysis of a single turboprop aircraft with a maximum take-off weight of 2,200 lbs. The aircraft's wing structure is a conventional mid-wing configuration of a twisting trapezoidal planform with an aspect ratio of 0.6. The analysis involved determining the loads acting on the wing structure. That is, the aircraft's flight envelope and the wing's critical loading condition are according to Title 14 Code of Federal Regulations Part 23 (14 CFR Part 23). The wing CAD model, composed of the aircraft wing components of the spar, ribs, and skins, including its layout, was developed and analyzed based on available 7075T6 Aluminum sheets using the SolidWorks software. The results for the wing's critical loading condition showed that the wing tip displacement was less than 5% of the half-wingspan with a margin of safety of 0.5 and a mass of 117.97 lbs which was less than the expected mass of 132 lbs.

Keywords

Wing Structural Design
Finite Element Analysis
Normal Category Aircraft
14 CFR Part 23
Single Turboprop Aircraft

Time Scale of Article

Received 7 March 2022
Revised until 25 April 2022
Accepted 15 May 2022
Online date 28 June 2022

1. Introduction

Developing an aircraft involves a lot of effort regarding the market, technical data, commercial analysis, existing and competitive aircraft, payload, range, mission, organizing the design process, airworthiness and other standards, systems and equipment requirements, and innovation toward the world needs (Brandt et al., 2004; Jenkinson and Marchman III, 2003; Raymer, 1992). The aviation sector had been growing rapidly prior to the pandemic in 2019, that has had a major impact not only on aviation but also on the world economy. Now, after almost two years, the general aviation sector has started to make a good recovery. The General Aviation Market Association recently released its aircraft shipment report that indicated a 45.4% increase in turboprop aircraft in the first six months of 2021 compared to the same period in 2020, as the highest growth among all types (Table 1).

As mentioned earlier, the private aircraft industry is a market that is expected to grow significantly in the future. According to statistical data, leading companies in the United States could sell more aircraft each year if the recent COVID-19 pandemic did not exist. The largest market for the aircraft models that are used for general aviation (GA) operations in the United States, accounting for more than 60% of global private jet sales. The Asian market is less than 10%, and the future is certainly growing in Asia (Deane, 2022). This business opportunity caused a Thai entrepreneur who had experience in the business of assembling kit planes to see the direction and the gap and, therefore, come up with the idea of producing the first Thai brand of a fixed-wing aircraft. To achieve this, the company has a business model for developing a two-seater aircraft (Pengsiri, 2020) and other models in partnership with several institutions, state-owned and private sectors. The roadmap for the first fixed-wing aircraft model is to initially design an all-metal aircraft, for which the wing's structural layout is

*: Corresponding Author Phacharaporn Bunyawanichakul, phacharaporn.b@ku.ac.th
DOI: 10.23890/IJAST.vm03is01.0105

the purpose of this paper. Then, the structure will be replaced with composite material and be converted to electric aircraft for the air transportation needs of Thailand's sustainability and worldwide market.

Table 1.First Half Aircraft Shipments and Billings (Castro, 2020).

Aircraft Type	**2020**	**2021**	**%Change**
Piston Airplanes	503	565	+12.3%
Turboprops	152	221	+45.4%
Business Jets	244	264	+8.2%
Total Airplanes	899	1,050	+16.8%
Total Airplane Billing	**$7.9B**	**$8.6B**	**+9.4%**
Piston Helicopters	63	83	+31.7%
Turbine Helicopters	194	258	+33%
Total Helicopters	257	341	+32.7%
Total Helicopter Billing	**$1B**	**$1.4B**	**+37.7%**

This paper focuses on the conventional aircraft model powered by a single turboprop engine. The design and structural analysis of the wing's structure for a two-seater aircraft involves the input of the following specifications:

- Maximum Take-off Weight 2,200 lbs
- Basic Empty weight 990 lbs
- Maximum Usable Fuel 616 lbs
- Maximum Usable Load 264 lbs
- Engine power 240 hp
- Take-off 1,312 ft
- Take-off over 50 ft Obstacle 1,968 ft
- Climb Rate 3,000 ft/min
- Maximum Operate Altitude 28,000 ft
- Stall Speed with Flaps 61 KCAS
- Maximum Cruise Speed 320 KTAS
- Landing Ground roll 1,148 ft
- Wingspan 28.5 ft
- Length 21.0 ft
- Height 8.92 ft
- Cabin Width 4.13 ft
- Wing Area 95.1 ft^2
- Taper Ratio 0.6
- Airfoil NACA 65_2-415

The wing structural mass was defined as being 12% of the maximum take-off weight (MTOW), which is 264 lbs. The geometric wing twist is the wash-out type, distributed along the span by the wing incidence angle at the root of 3 degrees and the tip of -3 degrees.

This study presents the design of a simplified conventional aircraft wing made of aluminum. The simplified model of the wing structure consists of a single or box-shaped spar, ribs, and skin, excluding stringers. The combined flight envelope was calculated to present the most critical flight condition in the normal category aircraft according to Title 14 Code of Federal Regulations Part 23 (14 CFR Part 23) (FAA, 2018). The lift magnitude and distribution over the wingspan were determined for the simulation. The analysis was carried out to estimate the structural responses in terms of overall strength and tip deformation by the following objectives:

- Symmetrical positive and negative limit maneuvering load factor
- Mid wing stiffness: wing tip displacement < 5% of the wing's half span
- Wing mass estimation < 12% of maximum take-off weight
- Margin of Safety > 0.5

2. Theoretical Background

One of the most important factors to be considered in this section is the forces on the wing. All forces exerted on the wing by air loads from the speed of the aircraft and the strength of the wind in terms of gust wind speeds. The wing design of an aircraft requires a flight envelope, including gust speed, to ensure the operation of the aircraft and identify the maximum load factor that could be applied to the structure.

2.1. Aircraft flight envelope (gust included)

When the aircraft is flying, it is obviously required to be capable of operating in all weather conditions. The wing is the most important component of an aircraft for generating lift while moving forward in the air. Design wing loads consist of the loads exerted on the wing structure when maneuvering to the limits of the flight envelope, also known as the V-n diagram. The flight envelope is a plot of load factor versus airspeed

(Anderson, 1999; Bruhn, 1973; Curtis, 1997; Megson, 1999; Niu, 1988). It combines both aerodynamic and structural limitations of an aircraft. In the same meaning, it presents the maneuver boundaries for a given aircraft. A flight envelope is generally illustrated in Fig. 1 (top). Considering the positive load factor region, the maximum positive lift capability represents the aerodynamic limitation resulting from the maximum lift coefficient of the selected airfoil for the wing. The aircraft will stall over this curve, which is a parabolic trend from the well-known lift force equation as

$$Lift = nW = \frac{1}{2}\rho V^2 S C_{L,max} \quad (1)$$

where n is the load factor, W is the aircraft weight, ρ is the air density, V is the airspeed, S is the wing area, and $C_{L,max}$ is the maximum lift coefficient.

Similarly, the maximum negative lift capability is the aerodynamic boundary for the aircraft with a negative load factor controlled by the airfoil shape. There are four horizontal lines in Fig. 1 (top) that represent structural limitation by limit and ultimate load factor in both positive and negative regions.

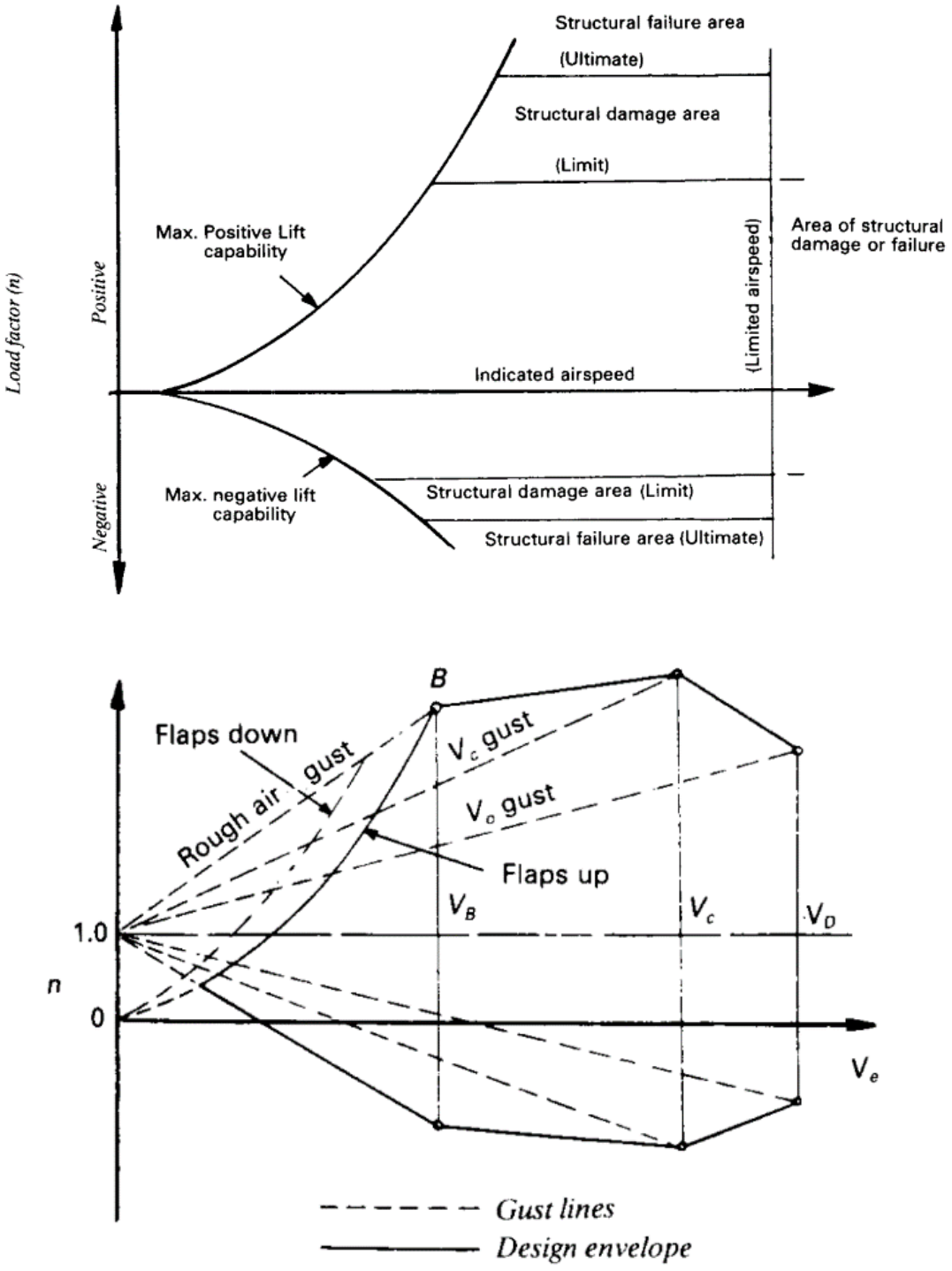

Fig. 1. (top) Typical and (bottom) combined flight envelope (Niu, 1988).

The values of limit and ultimate load factors depend on the mission, such as heavy bombers, cargo and passenger transports, light planes, advanced trainers, primary trainers, and military fighters. The single-vertical line also represents a structural limitation at a design dive speed (V_D). This is the maximum speed chosen for the aircraft's performance and operational requirements. To avoid penalizing the aircraft weight, care must be taken on the design dive speed. The aircraft structure must be designed to withstand the maximum load factor, including the nature of atmospheric turbulence in terms of gust effect. The additional loads imposed on the wing structure due to turbulent air may be greater than the maximum load factor in the typical flight envelope. As shown in Fig.1 (bottom), this combined flight envelope is the aircraft flight envelope with gust effect. The gust load factor is an additional load factor when the aircraft flies into the turbulence air gathered from statistical data. A simple equation represents the gust velocity in the vertical direction, resulting in an increased load factor from a level flight (n = 1) as follows:

$$n = 1 \pm \frac{K_g U_{de} V_e C_{L\alpha}}{498 * \frac{W}{S}} \quad (2)$$

where $K_g = \frac{0.88\mu}{5.3+\mu}$ which is the gust alleviation factor introduced in order to account for the behavior of the gust, which does not act instantaneously but rather in a sinusoidal manner, $\mu = \frac{2\frac{W}{S}}{g\bar{c}\rho C_{L\alpha}}$ which is the mass ratio in order to take into account the aircraft's dimension-the effect of the gust will be faster for the lighter aircraft, g is the gravitational acceleration of the Earth, $\bar{c}$ is the mean aerodynamic chord, $C_{L\alpha}$ is the lift-curve slope, U_{de} is the design gust velocity that is normally ±25, ±50, and ±60 ft/s depending on airworthiness authorities (FAA, 2018; EASA, 2017; CAAT, 2019), and V_e is the flight airspeed.

2.2. Spanwise lift distribution

The analysis of forces on the wing is essential to determine the lift required to be input into the simulation. Spanwise lift distribution was calculated using the lifting-line theory initially developed by Prandtl (Sadraey, 2013). First, the wing was divided into N segments along the span with each corresponding angle θ, as shown in Fig. 2.

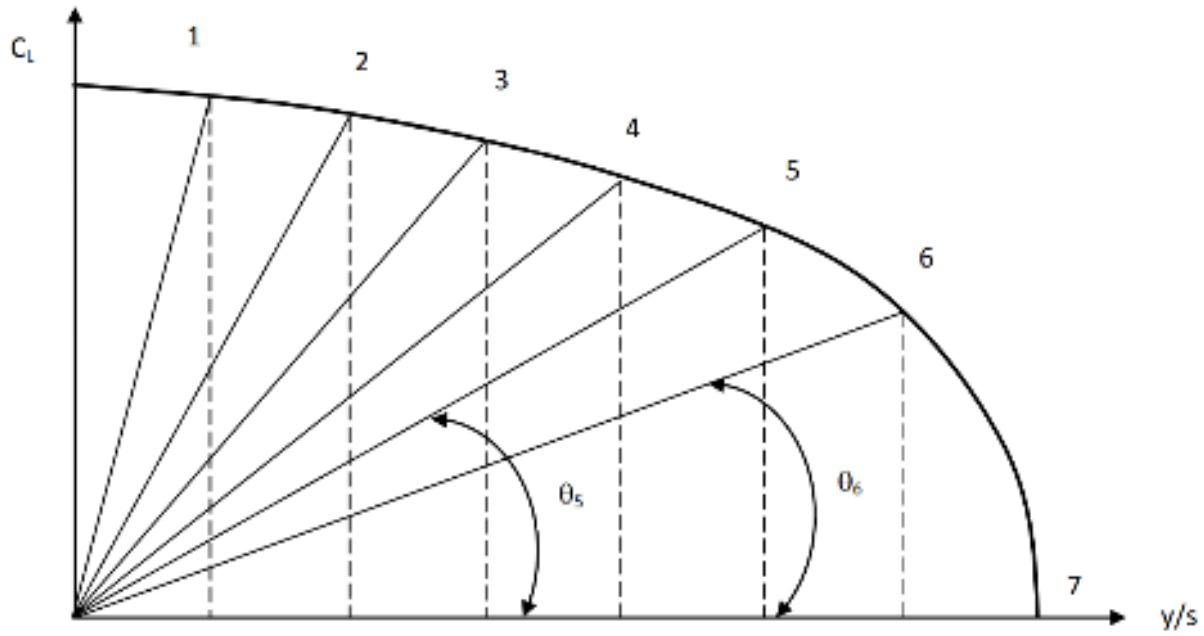

Fig. 2. Angles correspond to each segment in the lifting-line theory.

The aim was to solve for coefficients A_1 to A_n using the following equation:

$$\mu(\alpha - \alpha_0) = \sum_{n=1}^{N} A_n \sin(n\theta)\left(1 + \frac{\mu n}{\sin\theta}\right) \quad (3)$$

where α is the segment's angle of attack and α_0 is the segment's zero-lift angle of attack. The parameter μ is defined as:

$$\mu = \frac{\bar{C}_i C_{l,\alpha}}{4b} \quad (4)$$

Where $\bar{C}_i$ is the segment's mean geometric chord, $C_{l,\alpha}$ is the segment's lift curve slope, and b is the wingspan. Each segment's lift coefficient was finally determined using the equation:

$$C_{Li} = \frac{4b}{\bar{C}_i} \sum A_n \sin(n\theta) \quad (5)$$

The spanwise lift distribution is estimated using unit load analysis in accordance with the segment's lift coefficient (Bruhn, 1973). Because this load acts through

the 40 percent chord line at each station, it results in the distribution of shear force, bending moment, and torsion for a level flight (n = 1) under certain flight conditions. The maximum load factor will then be multiplied at the corresponding airspeed to determine the most critical flight condition.

2.3. Required strength of the wing's structure

The structural limitations in aircraft design are generally divided into two categories: limit and ultimate load factor (Pengsiri, 2020; Castro, 2020; FAA, 2018; Megson, 1999). The limit load factor is the boundary where permanent structural deformation of the aircraft occurs, while ultimate load factor is the boundary that the aircraft structure will break. The margin of safety (M.S.) in terms of the ultimate strength and allowable stress can be expressed as

$$Margin\ of\ Safety = \frac{Ultimate\ strength}{Allowable\ stress} - 1 \qquad (6)$$

2.4. Simplified modeling

Due to the symmetry related to the mid-fuselage, only the half wing was modeled. Two models were initially created by assembling the main components of the wing structure, including the rib, skin, and single or box spar. The rib spacing in the original wing model was set with even spacing at least one-fifth of the chord (Zahm, 1920). Fig. 3 (left) shows the main components of the wing structure with a single spar located at 40% of the chord length along the wingspan. Fig. 3 (right) is the half-wing model with the box spar replacing the single spar in the left picture. The wing loading obtained from the previous section was considered when designing the components based on simple beam theory (Curtis, 1997; Megson, 1999). The thickness of each component is assigned according to the available thickness of the sheet (Table 2). The wing model was developed with constant taper and twist and used 7075T6 aluminum sheets, with its material properties shown in Table 2. The model was prepared as a surface with no defined thickness, which was later identified in the pre-processing tool.

Table 2. Properties of 7075T6 aluminium sheet (Aircraft Spruce, 2020).

Property	Value
Density, lb/in^3	0.101518
Young's modulus, Msi	10
Poisson's ratio	0.33
Yield strength, ksi	64
Ultimate tensile strength, ksi	75
Available thicknesses, inch	0.04, 0.05, 0.063, 0.125

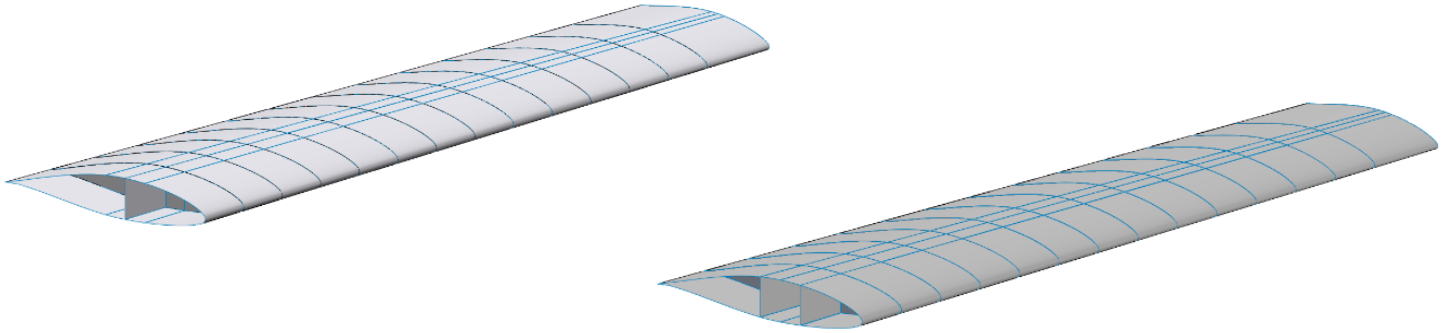

Fig. 3. Half-wing layout with (left) single and (right) box spar.

All wing components were created as 2D shells. The wing is fixed at the root. The loads are applied as obtained from the spanwise lift distribution. The structural response was simulated and analyzed to fulfill the objectives of this study, which are strength, deformation, and weight.

3. Results and Discussion

3.1. Extreme load factor identification

A combined flight envelope was written in the Mathcad program. Referring to Title 14 Code of Federal Regulations Part 23 (14 CFR Part 23), the maximum positive and negative load factors for the normal category are +3.8 and -1.5, respectively. The stall speed was determined at the corresponding maximum lift coefficient of the NACA 65_2-415 airfoil (Abbott and Von Doenhoff, 1958), while the dive speed was 1.4 times the cruise speed. Gust wind speeds of 25 and 50 ft/s were included in determining the load factors, both positive and negative, at the maximum operation speed (V_{Cmax}) and dive speed, respectively. The aircraft flight envelope is a diagram that maps the possible combination of minimum and maximum values of speed versus load factor that the aircraft can experience during flight. The aircraft can operate without suffering permanent deformation or structural damage. This envelope combines the maneuvering envelope and the gust envelope, as shown in Fig. 4 from the aircraft specifications given in Section 1.

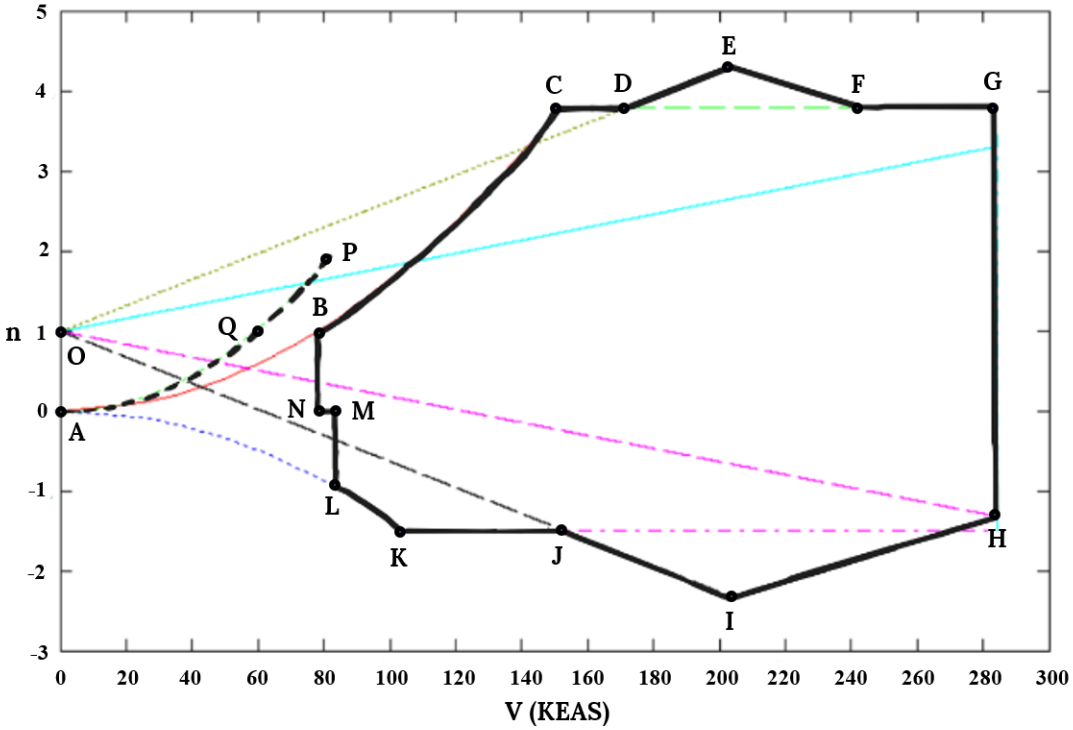

Fig. 4. Combined flight envelope.

There are 17 points that play an important role in the flight maneuver for this aircraft, as illustrated by the points A to Q in Fig.4. The combined flight envelope shows a plot of load factor versus equivalent airspeed in knots. Point A is the point of zero magnitudes for both load factor and airspeed. Point B represents an airplane flying at level flight with a speed of 77.84 knots, which is also the stall speed. Point C is the corner speed that presents the point of the highest load factor at the stall speed for the aircraft. The flying condition at this point is also well-known as the positive high angle of attack (PHAA) condition. The aircraft's wing structure will be subjected to the maximum compression in the upper flange of the forward stiffener, while the maximum tension will be generated in the lower flange of the rear stiffener for the conventional wing box structure. The aerodynamic limit, obtained from the maximum lift coefficient, is the curve between points B and C. The region above this line is the stall region. The horizontal line CG denotes the positive limit load factor at speed between 151.73 knots and 284.11 knots; the former is the corner speed, and the latter is the dive speed. Point G is also called a "positive low angle of attack" (PLAA) condition, where the highest compression will occur at the rear longeron in the upper flange while the highest tension will occur at the forward longeron in the lower flange.

Point O represents the level of flight for the aircraft at no speed, as shown by n = 1 intersecting the Y-axis. The line OE denotes the variation of the load factor at a gust speed of 25 ft/s, which means that the additional load factor is linearly proportional when increasing airspeed. The intersection of the gust speed at 25 ft/s and the maximum cruise or operating speed is at point E. The straight line between the points D and E shows the additional gust load factor that becomes n = 4.31 obtained by eq.2 with the gust wind speed of 25 ft/s, which is the maximum positive load factor at the maximum cruise speed of the aircraft. The load factor at point G at the dive speed is 3.8. The gust speed of 50 ft/s has no influence on the maximum load factor specified in the normal category, with the intersection of the gust line and dive speed being less than 3.8. The vertical line GH represents an airplane flying at a dive speed with a load factor of between 3.8 and -1.32.

The combined flight envelope in the negative load factor zone is plotted in the same manner as the positive one. The speed at point L is greater than that at point B, which is 88.39 knots, due to the unsymmetrical airfoil. The line NB and ML show the level flight condition of the aircraft in the positive and negative load factors, respectively. The curve between points L and K is the stall limit in the negative region. The aircraft velocity corresponding to point K is 104.59 knots, which is less than the corner speed. This point is also called "negative high angle of attack" (NHAA), where the highest compression will occur in the forward longeron in the lower flange while the highest tension will occur in the rear longeron in the upper flange. The limit load factor in the negative region is -1.5, which is the horizontal line passing through points K. The highest load factor, calculated from the gust airspeed of -25 ft/s, is -2.31 at the maximum operating speed as represented by the point I. The wing's structure requires to withstand the load factor of -2.31

at this point. It is noted that the load factor at the point I is lower than the minimum load factor where the flight envelope with combined gust calls the "negative low angle of attack at the maximum operation speed" (NLAA, V_{Cmax}) condition. It means that the aerodynamic force on the wing at the point I will cause maximum compression in the lower flange rear longeron and maximum tension in the upper flange forward longeron. Analogous stress acting on the wing from the flight behavior of point I can be stated at point H, the "negative low angle of attack" at the operating speed (NLAA, V_D) condition. Point H shows the intersection between the dive speed and the total load factor resulting from the gust airspeed of -50 ft/s where the wing's structure is required to withstand the load factor of -1.32. It is noted that the load factor at point H is greater than the minimum load factor where the flight envelope with combined gust calls the "negative low angle of attack at the design dive speed" (NLAA, V_D) condition.

The combined flight envelope with flap down, shown as the curve between points A and P, expands the stall region by reducing the stall speed for level flight to 58.75 knots at point Q compared to the flap up condition with the stall speed for the level flight of 77.84 knots at point B. However, the load factor is limited by 2 in the case of flap deployment due to the generation of too much lift. The wing structure layout and dimension will be designed, requiring a different load factor according to the aircraft type.

The design of the wing's structure must take the largest expected load into account. The maneuver boundaries, including gust effects, show the value of the maximum load factor corresponds to that at either point E or G in Fig. 4 in the positive region, while the minimum load factor is not the critical load due to the shape of the airfoil. It means that the maximum operating speed intersects with the gust load factor of 25 ft/s at n = 4.31, and the dive speed intersects with the gust load factor of 50 ft/s at n = 3.8 from the diagram. Both points were compared based on the spanwise lift distribution at n = 1 to identify the maximum values of the load factor expected to occur with the wing's structure.

From the calculation, the aerodynamic forces acting on the center of pressure, denoted by c.p., are approximately located at 0.40 of the airfoil's chord point, measured from the leading edge. A set of Microsoft Excel® workbooks created shows the spanwise distribution of lift, shear force (V), bending moment about 40% chord ($M_{x40\%c}$), and torsion about 40% of the chord (T) for a level flight (n = 1) at the critical flight condition as described in calculating wing shears and moments for one unit load condition on half-wing (Bruhn, 1973). Fig. 5 shows the lift distribution on the half-wing at n = 1 for the same speed of points E and G, corresponding to V_{Cmax} and V_D, respectively. The curve demonstrates an elliptical lift distribution applied to the half of the wing, where the maximum value occurs at the root of the wing and zero at the tip. The lift force distribution when the aircraft flies at maximum cruise and dive speeds is approximately 19.04 and 37.89 lb/in. It is noted that the pressure distribution generated by moving air results in the lift and drag force acting at the center of pressure. The resultant drag is neglected in this study. The lift resultant is considered to act at 40% of the chord point and results in torsion distribution by aerodynamic forces along the wingspan.

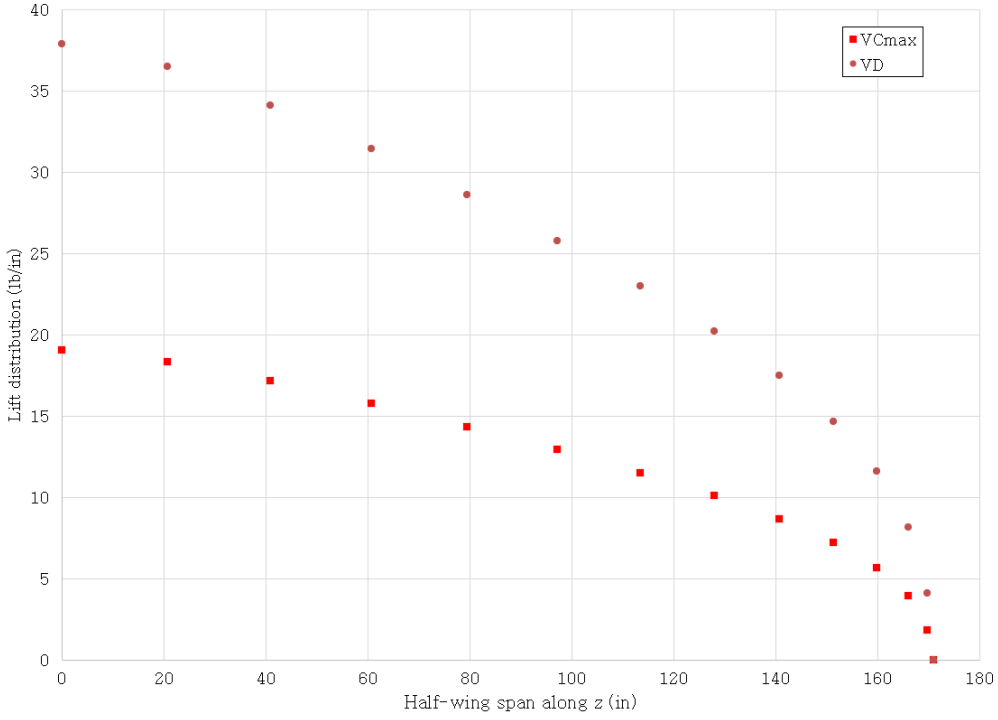

Fig. 5. Lift distribution on half-wing at n=1.

This study was carried out with the aircraft's fuselage oriented along the X-axis, the Y-axis oriented vertically, and the Z-axis perpendicular to the plane XY. The shear force distribution was obtained by the numerical integration of the spanwise lift distribution. The bending moments (M_x) could similarly be constructed with the numerical integral of the shear distribution. Fig. 6 shows results from the calculation of wing shear (V) and wing bending moments due to wing structure weight and lift acting upward in the Y direction and applied at 0.4 of the chord's length. They were calculated in a spanwise direction when the aircraft is flying in a level flight condition (n = 1). The results show the critical shear force and bending moment occur at a diving condition corresponding to 4,407 lbs and 312,555 in-lb compared to 2,207 lbs and 155,970 in-lb for the maximum operating speed. The load factor of 3.8 at the dive speed, therefore, is the most critical condition for the wing structure design concerning the combined flight envelope.

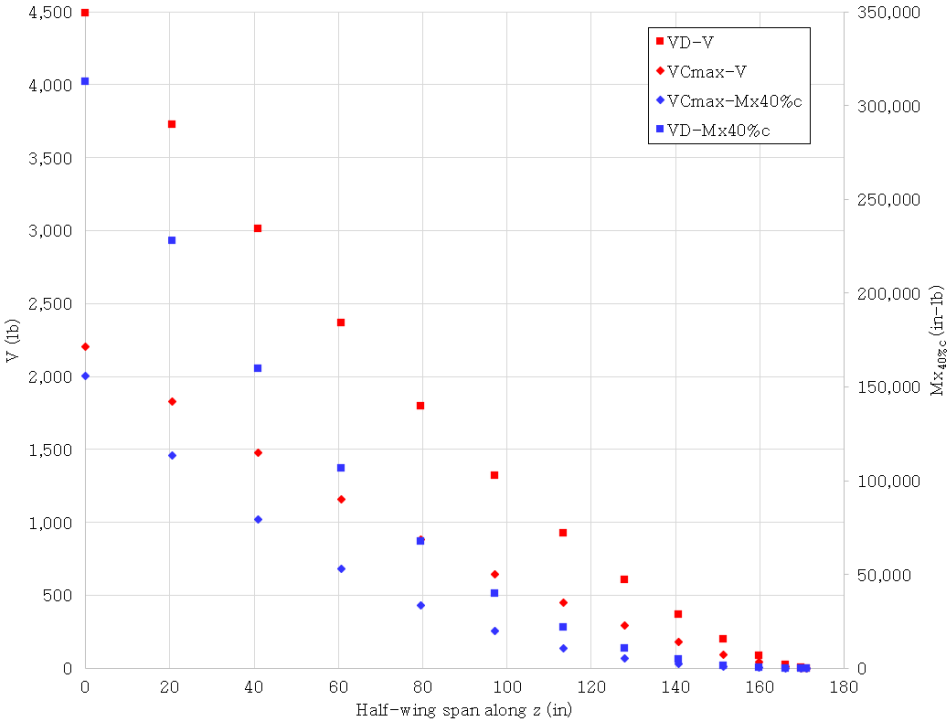

Fig. 6. Shear force (V) and bending moment about 40% chord ($M_{x40\%c}$) distribution on half-wing at n=1.

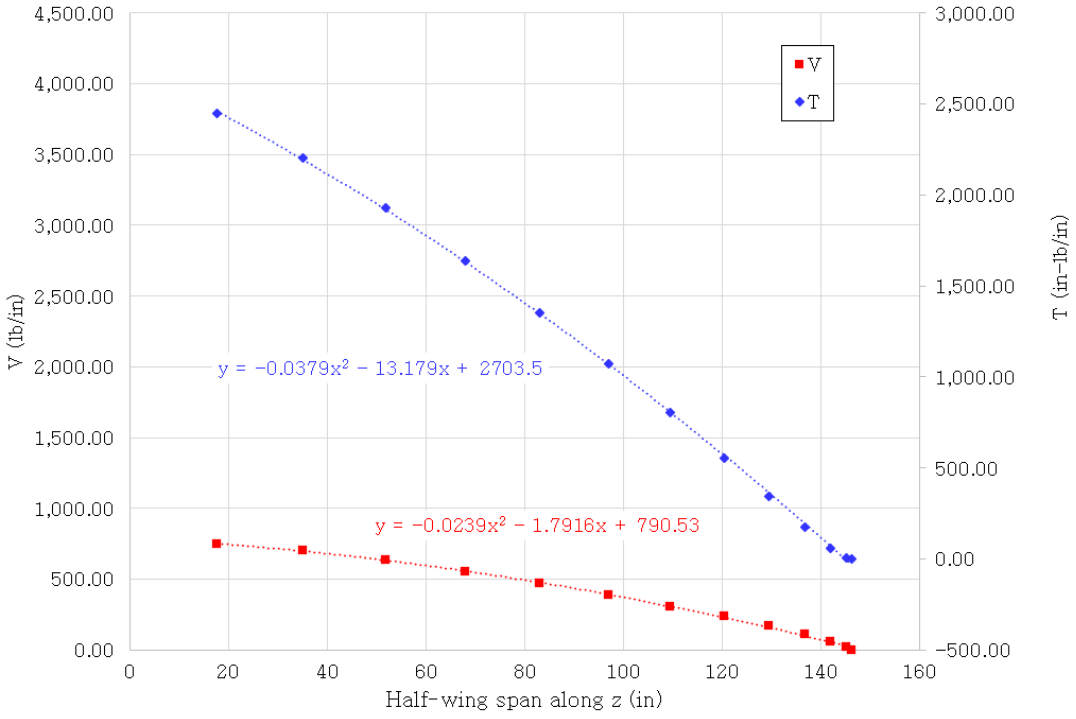

Fig. 7. Shear force (V) and Torsion about 40% of the chord (T) distribution on half-wing at the dive speed.

The distribution of shear force and torsion about 40% chord along the wingspan was generated when the aircraft flew at dive speed and n = 3.8, which is the maximum load factor (Fig.7). The fuselage size was taken into the calculation for the wing configuration of the mid-fuselage type. At the dive speed and the maximum load factor (n = 3.8), the total shear force applied to the wing's structure was 16,747 lbs. The shear force (V) was varied along the Z-axis using reference coordinates that were initially located at 40% of the chord length and was calculated using the equation:

$$V(z) = -2.39 \times 10^{-2} z^2 - 1.792z + 790.53 \quad (7)$$

Similarly, the variation of torsion was applied to the wing spar at approximately 40% of the chord length, with a total intensity of 57,762 in-lb using the equation:

$$T(z) = -3.79 \times 10^{-2} z^2 - 13.18z + 2704 \quad (8)$$

3.2. Wing structural analysis

Static studies were carried out to observe the structural behavior with the mesh preview as shown in Fig. 8. The thicknesses of each surface were visualized and checked to see if they were as expected. The analysis with a single spar layout is initially generated. The model shows each rib was placed every 10" from root to tip, except for the last bay, where the spacing is greater than the other bays to fit with the semi-span length. All surfaces were divided into several small elements using a curvature-based mesh. A convergence study was carried out to find the optimum element size and was adopted in all the models. The maximum and minimum element sizes were 3" and 1", respectively. The left picture in Fig. 3 represents six simplified models in Table 3. The models were created with 15 ribs, 14 bays, 56 flanges, and 28 skins. Table 3 describes six models with different thickness attributions. For the first model (Model 1), a constant thickness is specified for the same component. The ribs and the spar webs had a thickness of 0.063". The thickness of the spar flanges was made using three layers of 0.125" aluminum plate; therefore, it is 0.375". All skins had a thickness of 0.04". The total structural weight for the Model 1 was estimated to be 129.85 lbs. The simulation results show the maximum Von Mises stress is 46.5 ksi and the tip deformation is 7.31". This results in an unsatisfactory margin of safety as described in Table 3. It is expressed with an alphabet "U" in the evaluation row for Model 1.

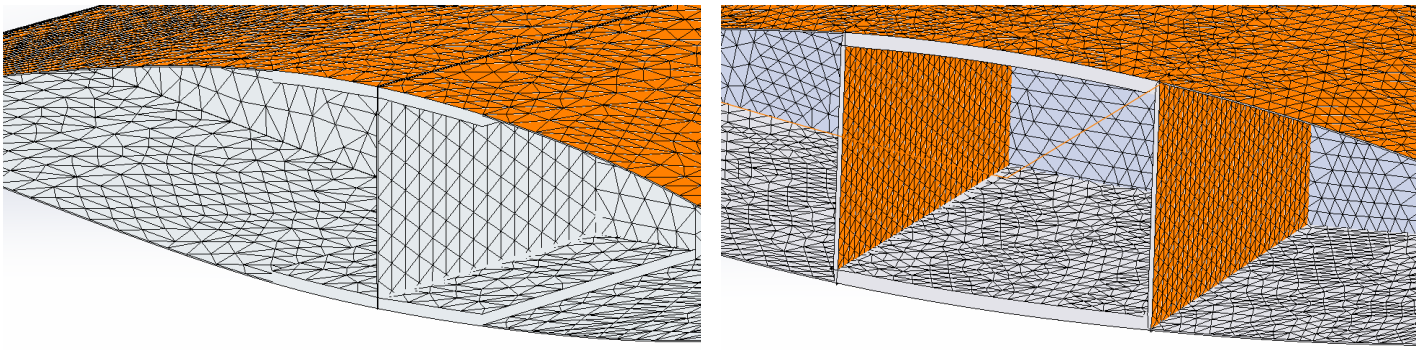

Fig. 8. Mesh preview for the different spar layouts: (left) single and (right) box spar.

The Model 2 was a modification of the Model 1 by increasing the spar web thickness to 0.125", but the result was still unsatisfactory for the reason of being overweight. The modification, Model 3, still focused on the spar web thickness by keeping the first three bays from the root at a thickness of 0.125" and using a thickness of 0.063" for the rest. All objectives were satisfied, or S, as shown in the table. The Model 4 was indeed satisfied by using the ribs' thickness of 0.04" to reduce weight. The last two models, Models 5 and 6, were studied by focusing on thinner sheets for some parts of the spar flanges and webs. However, unsatisfactory results were obtained from the simulation. All results show that the wing's structure with a layout of a single spar was not effective in terms of strength, deformation, weight, and margin of safety. This led to using the layout of a box beam spar, as shown in the right picture in Fig. 3.

A modified model was developed by replacing a single spar with a box spar, as described in Table 4. As it was a simplified model, the number of the spar web components was directly doubled to 28 pieces. The Model 7 is developed with a constant thickness for the same component. The ribs and the spar webs had a thickness of 0.05". The thickness of the spar flanges was made using two layers of 0.125" aluminum plate; therefore, 0.25". All skins had a thickness of 0.04". The total structural weight for the Model 7 was estimated to be 108.20 lbs. The simulation results show the maximum Von Mises stress is 58.63 ksi and the tip deformation is 10.13". This results in both an unsatisfactory margin of safety and displacement. This led to a modification by increasing the thickness of the flange to only three bays from the wing root, but the results were still unsatisfactory for the Model 8. The Model 9 was generated to reduce the maximum stress so that the spar webs were thicker at three bays from the wing root. The Model 10 was modified from the Model 9 with an increased thickness of 0.125-inch for the spar web and,

to keep the weight within the limitation, the ribs had a thinner plate for the one that does not belong to the three bays from the root. The results from the simulation greatly reduced the maximum stress, but the tip displacement was still unsatisfied with the design framework. Model 11 was the last one that corresponded to the right picture in Fig.3 and the first model in Table 4 that met the objectives of this study by using a 0.375-inch flange thickness. However, the total weight was quite heavy towards the limit, so the Model 12 was generated to mainly focus on the uneven spacing of the wing ribs, as illustrated in Fig. 9, since the stress concentration zone was located near the wing root.

Table 3. The model with a single spar.

Model descriptions and results	Single spar					
	Model 1	**Model 2**	**Model 3**	**Model 4**	**Model 5**	**Model 6**
Rib, pieces	15	15	15	15	15	15
Web, pieces	14	14	14	14	14	14
Flange, pieces	56	56	56	56	56	56
Skin, pieces	28	28	28	28	28	28
Rib thickness, inch	0.063	0.063	0.063	0.04	0.04	0.063
Web thickness, inch	0.063	0.125	0.125 (3 bays from root), 0.063	0.125 (3 bays from root), 0.063	0.125 (3 bays from root), 0.063	0.125
Flange thickness, inch	0.375	0.375	0.375	0.375	0.25	0.375 (3 bays from root), 0.25
Skin thickness, inch	0.04	0.04	0.04	0.04	0.04	0.04
Weight, lbs	129.85	134.99	131.09	126.15	104.23	119.36
Maximum Von Mises stress, ksi	46.5	36	36.85	36.95	49.28	42.50
Tip deformation, inch	7.31	6.99	7.17	7.18	9.88	8.71
% Wing tip displacement	<5	< 5	< 5	< 5	>5	>5
% Wing mass to MTOW	< 12%	> 12%	< 12%	< 12%	< 12%	< 12%
Margin of Safety	< 0.5	> 0.5	> 0.5	> 0.5	< 0.5	> 0.5
Evaluation*	U	U	S	S	U	U

*S = Satisfied, U = Unsatisfied

Table 4. The model with box spar.

Model descriptions and results	Box spar					
	Model 7	**Model 8**	**Model 9**	**Model 10**	**Model 11**	**Model 12**
Rib, pieces	15	15	15	15	15	9
Web, pieces	28	28	28	28	28	16
Flange, pieces	56	56	56	56	56	32
Skin, pieces	28	28	28	28	28	16
Rib thickness, inch	0.05	0.05	0.05	0.05 (3 bays from root), 0.04	0.05 (3 bays from root), 0.04	0.063 (3 bays from root), 0.04
Web thickness, inch	0.05	0.05	0.063 (3 bays from root), 0.05	0.125	0.125	0.125
Flange thickness, inch	0.25	0.375 (3 bays from root), 0.25	0.375 (3 bays from root), 0.25	0.375 (3 bays from root), 0.25	0.375	0.375 (3 bays from root), 0.25
Skin thickness, inch	0.04	0.04	0.04	0.04	0.04	0.04
Weight, lbs	108.20	114.49	115.02	125.54	130.89	117.97
Maximum Von Mises stress, ksi	58.63	54.31	50.47	35.52	34.21	43
Tip deformation, inch	10.13	8.24	8.80	8.12	6.61	6.48
% Wing tip displacement	>5	>5	>5	>5	< 5	< 5
% Wing mass to MTOW	< 12%	< 12%	< 12%	< 12%	< 12%	< 12%
Margin of Safety	< 0.5	< 0.5	< 0.5	> 0.5	> 0.5	> 0.5
Evaluation*	U	U	U	U	S	S

*S = Satisfied, U = Unsatisfied

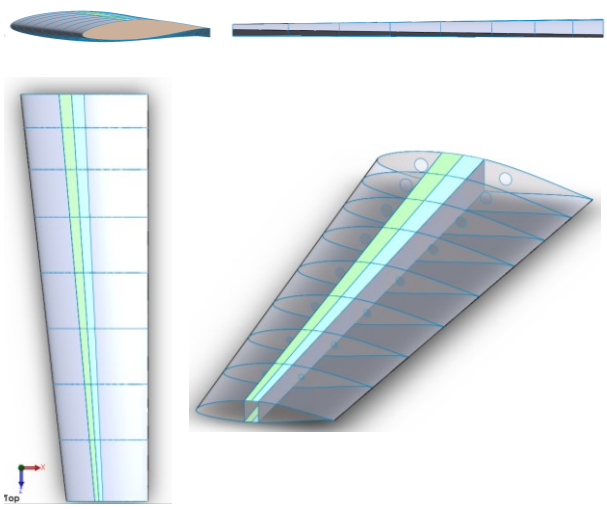

Fig. 9. Wing model from top, side, front, and 3D view.

The wing design was finally created with a box spar layout. For weight reduction purposes, the ribs had three circular cut-outs. The model consisted of nine ribs, eight bays, 32 flanges, and 16 skins, as described in Model 12 of Table 4. Fig. 9 shows multiple drawing views of the wing model: top, side, front, and 3D view. Different thicknesses were defined for the wing model, as illustrated in Fig. 10. All skins had a thickness of 0.04", and the spar webs had a thickness of 0.125". The thickness of the spar flanges corresponding to bays 1 to 3 from the wing root used three layers of 0.125" aluminum plate. In comparison, the rest of the flanges had only two layers. The four ribs on the root side had a thickness of 0.063". In contrast, the rest had a thickness of 0.04". The total structural weight was estimated to be 117.97 lbs, which was less than the wing mass estimation of 132 lbs.

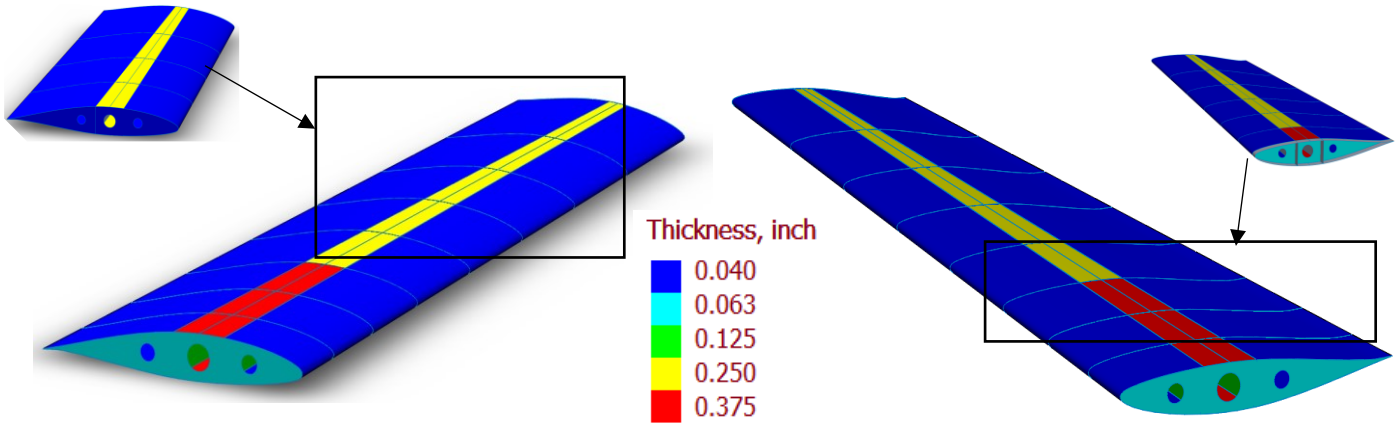

Fig. 10. The thickness of each surface: from a top (left) and bottom isometric view (right).

3.3. Discussion

The static structural analysis was performed to provide the wing layout for a single turboprop normal category aircraft. The most critical flight condition was identified at the dive speed with a load factor of 3.8. The wing's structure is subjected to estimated lift and torsion distribution. Fixed support is applied at one end of the wing as it is attached to the fuselage's structure. The models using shell elements present a wing structure, with the box spar layout being more effective than the one with the single spar layout at the preliminary aircraft design stage. The results could give more ideas about the loading combination of lift and torsion distribution that might be too complex to estimate from a simplified calculation for the same loading. The output in terms of Von Mises stress and displacement is shown in Fig. 11 (top) and Fig. 11 (bottom), respectively. It is obvious that the Von Mises stress is locally high at the wing root because this is the fixed end location of the defined boundary condition. Localized stresses exist at the skin, spar, and rib connections, but they are not severe enough to cause catastrophic failure of the wing's structure. The stress contour shows the region having a margin of safety of 0.5 at the wing-fuselage junction. This region could be reinforced during the manufacturing process. It was noted that the maximum displacement of 6.48" occurred at the wing tip, which satisfied the constraint of being less than 5% of the wing's half span. The wing gradually twisted and deformed in its spanwise direction. It is in accordance with the applied load and boundary condition.

The equal rib spacing was designed for the initial model. The structural analysis was carried out to adjust the layout of the main components under the extreme flight conditions obtained from the flight envelope. The maximum stress should be less than 43 ksi to keep the margin of safety within the framework. Increasing the thickness of each component could increase the margin of safety but put a penalty on the weight. The final wing structure layout was optimized in all conditions. This methodology could be implemented for the model made of composite material later.

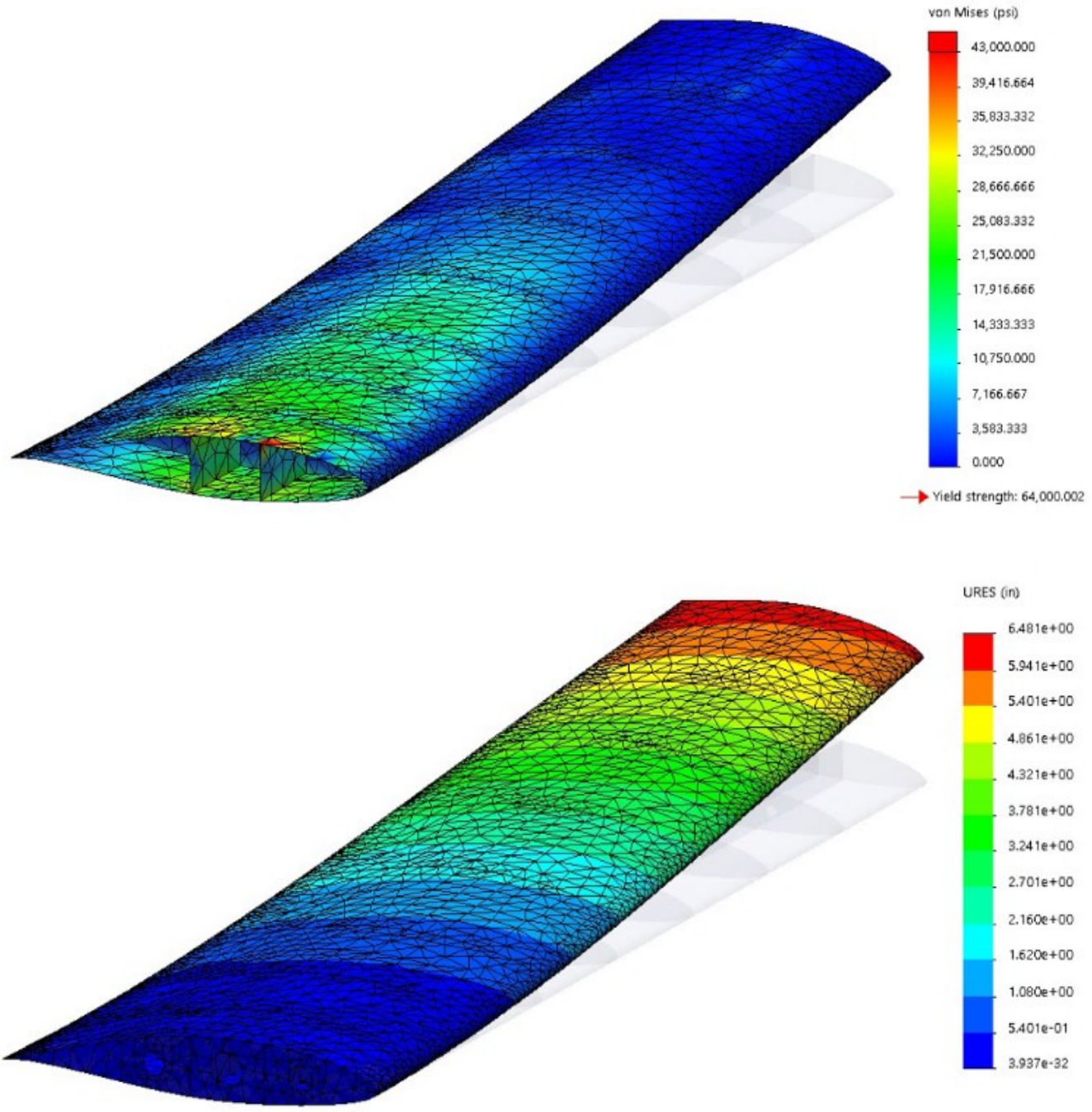

Fig. 11. Von Mises stress of the wing (top) and wing displacement (bottom).

4. Conclusions and Further Studies

Based on the information presented in the flight envelope and the critical wing loading, an initial wing structure was developed that met all aircraft structural and operational requirements according to Title 14 Code of Federal Regulations Part 23 (14 CFR Part 23). The structural behavior of a three-dimensional wing has been simulated using single and box spars based on the shell element type. The simplified model successfully achieved the objectives of this study in terms of strength, displacement, and weight. However, the model is made entirely of aluminum. The design of the wing structure could be lighter and optimized with composite materials. The analysis with composite wings and electric aircraft is on the way according to the roadmap of the company toward Thailand's sustainability. Further study could be done in many aspects, including analysis with stringers, cut-outs, and control surfaces, detailed design in the high-stress concentration region, wing design and optimization, buckling analysis, flutter analysis, composite material replacement, unsymmetrical flight condition, and construction and testing of individual components for structural integrity behavior.

CRediT Author Statement

Vis Sripawadkul: Conceptualization, Methodology, Software, Resources, Investigation, Writing-Review & Editing. **Phacharaporn Bunyawanichakul**: Conceptualization, Methodology, Software, Resources, Investigation, Validation, Writing-Original Draft.

References

Abbott, I.H. and Von Doenhoff, A.E., 1958. Theory of Wing Sections. Dover Publications Inc.

Aircraft Spruce, 2020, Aircraft Spruce & Speciality Co., General Aluminum Information, **Error! Hyperlink reference not valid.**

Anderson, J.D., 1999. Aircraft Performance and Design. McGraw-Hill, ISBN 0-07-001971-1.

Bruhn, E.F., 1973. Analysis and Design of Flight Vehicle Structures. Jacobs & Associates Inc.

Brandt, S.A., Stiles, R. J., Bertin, J. J. and Withford, R., 2004. Introduction to Aeronautics: A Design Perspective. Second Edition. American Institute of Aeronautics and Astronautics Educational Series.

Castro, A., 2020. GAMA Publishes Second Quarter 2021 Aircraft Shipments and Billings Report, General Aviation Manufacturers Association, **Error! Hyperlink reference not valid.**

Curtis, H.D., 1997. Fundamentals of Aircraft Structural Analysis. McGraw-Hill.

Deane, S., 2022. 2022 Key Private Jet Industry Statistics – By Region, By Country, By Type, Stratos Jet Charters, Inc., https://www.stratosjets.com/blog/private-jet-statistics/

European Aviation Safety Agency (EASA), 2017. Certification Specifications for Normal, Utility, Acrobatic, and Commuter Aeroplanes (EASA CS-23).

Federal Aviation Administration (FAA), 2018. United States Department of Transportation, Title 14 Code of Federal Regulations Part 23 - Airworthiness Standards: Normal, Utility, Aerobatic, and Commuter Category Aeroplanes (14 CFR Part 23).

Jenkinson, L.R. and Marchman III, J.F., 2003. Aircraft Design Projects for Engineering Students. First Edition. Butterworth-Heinemann.

Megson, T., 1999. Aircraft Structures for Engineering Students. Second Edition. Elsevier.

Niu, M.C.Y., 1988. Airframe Structural Design. Conmilit Press Ltd.

Pengsiri, J., 2020. JFOX Sport Thunder, JFOX Aircraft Co., Ltd., https://www.jfoxaircraft.com/aircraft/sport-thunder

Raymer, D.P., 1992. Aircraft Design: A conceptual Approach. American Institute of Aeronautics and Astronautics.

Sadraey, M.H., 2013. Aircraft Design: A Systems Engineering Approach. Wiley.

The Civil Aviation Authority of Thailand (CAAT), 2019. Air Navigation Act B.E.2497 Section 34 (1). Airworthiness Standards: Normal, Utility, Acrobatic, and Commuter Airplanes. www.caat.or.th/th/archives/42000 [in Thai].

Zahm, A.F., 1920. Relation of Rib Spacing to Stress in Wing Planes. National Advisory Committee for Aeronautics: Technical notes No.5.

Annex 1: High Resolution Image for Article 3 Fig. 2. General Simulink model of the F-16 aircraft before trimming phase